DISSERTATION

ELECTROMAGNETIC MODEL SUBDIVISION AND ITERATIVE SOLVERS FOR SURFACE AND VOLUME DOUBLE HIGHER ORDER NUMERICAL METHODS AND APPLICATIONS

Submitted by

Sanja B. Manić

Department of Electrical and Computer Engineering

In partial fulfillment of the requirements

For the Degree of Doctor of Philosophy

Colorado State University

Fort Collins, Colorado

Fall 2019

Doctoral Committee:

Advisor: Branislav Notaroš

Steven Reising
V. Chandrasekar
Iuliana Oprea
Milan Ilić

ABSTRACT

ELECTROMAGNETIC MODEL SUBDIVISION AND ITERATIVE SOLVERS FOR SURFACE AND VOLUME DOUBLE HIGHER ORDER NUMERICAL METHODS AND APPLICATIONS

Higher order methods have been established in the numerical analysis of electromagnetic structures decreasing the number of unknowns compared to the low order discretization. In order to decrease memory requirements even further, model subdivision in the computational analysis of electrically large structures has been used. The technique is based on clustering elements and solving/approximating subsystems separately, and it is often implemented in conjunction with iterative solvers. This thesis addresses unique theoretical and implementation details specific to model subdivision of the structures discretized by the Double Higher Order (DHO) elements analyzed by i) Finite Element Method - Mode Matching (FEM-MM) technique for closed-region (waveguide) structures and ii) Surface Integral Equation Method of Moments (SIE-MoM) in combination with (Multi-Level) Fast Multipole Method for open-region bodies. Besides standard application in decreasing the model size, DHO FEM-MM is applied to modeling communication system in tunnels by means of Standard Impedance Boundary Condition (SIBC), and excellent agreement is achieved with measurements performed in Massif Central tunnel. To increase accuracy of the SIE-MoM computation, novel method for numerical evaluation of the 2-D surface integrals in MoM matrix entries has been improved to achieve better accuracy than traditional method. To demonstrate its efficiency and practicality, SIE-MoM technique is applied to analysis of the rain event containing significant percentage of the oscillating drops recorded by 2-D video

disdrometer. An excellent agreement with previously-obtained radar measurements has been established providing the benefits of accurately modeling precipitation particles.

ACKNOWLEDGMENTS

I would like to express the gratitude to my advisor Dr. Branislav Notaroš for teaching me computational electromagnetics, encouraging and guiding throughout my research. I would also like to thank Dr. Milan Ilić, Dr. V. N. Bringi and Dr. Merhala Thurai for providing their expertise and guidance during my studies. Special gratitude goes to my colleagues Ana Manić, Elene Chobanyan, Nada Šekeljić and Pranav Athlaye for providing supportive, collaborative, intellectually inspiring and fun environment, making the time spent in the laboratory creative and enjoyable. I would like to thank Dr. Bill Eads and Olivera Notaroš for choosing me to be their teaching assistant and coaching me into acquiring skills needed to instruct. Last but not least, I would like to thank my family for their love and support and my husband Dr. Mikhail Strizhov for giving me confidence to present my work and for his endless encouragement.

DEDICATION

To my parents, Nataša and Branislav Manić,

for encouraging and creating the person I am today.

TABLE OF CONTENTS

INTRODUCTION

Higher order curvilinear elements conform to arbitrary shapes enabling accurate modeling of the geometry. Higher order basis functions model the unknown enabling the element size to be of the order of the wavelength, unlike the low order discretization which is limiting element size to a tenth of the wavelength. Both of these features decrease the number of unknowns (i.e. memory) needed for the computer simulation of the electromagnetic phenomena. With the current demand to analyze electrically large, finely structured and complex systems of electromagnetic bodies, domain decomposition and approximate methods, decreasing the computational complexity, have found the vast development and use in computational sciences. Model subdivision, i.e. element grouping of the model under analysis, plays the key role decreasing the memory load even further. This dissertation includes details specific to model subdivision of the double higher order discretization applied to Finite Element Method (FEM) for closed-region (waveguide) structures computing electric field vector as the unknown in the volume elements and Surface Integral Equation Method of Moments (SIE-MoM) for open-region bodies computing equivalent current vector on the surface elements. The closed (waveguide) structure is divided into subdomains that are analyzed separately and Generalized Scattering Matrix (GSM) for each subdomain is obtained. GSM is computed using Mode Matching (MM) technique in conjunction with 3-D FEM, with the modal forms at the subdomain ports being computed by double higher order 2-D FEM analysis solving the eigenvalue problem solved by Krylov subspace iterative process Lanczos method. The subdomains are then connected into the original structure via GSM concatenation. The open region structures are divided using Octree grid and analyzed using SIE-MoM in conjunction with Fast Multipole Method and its' Multi-Level version enabling fast matrix vector multiplication in the Krylov subspace iterative solver implementation (Generalized minimal

residual method). Both, volumetric and surface, methods decrease the memory needed for the computer simulation and enable large models to be analyzed on a personal computer. Extraction method for 2-D surface integration used in calculating entries in MoM matrix has been previously developed in order to precisely compute near-field 2-D integrals [42]. Unlike the traditional extraction techniques, novel method takes into account curvature of the basis element as well as higher order of the basis functions in the computation of the integrals evaluated over parallelogram. The extension of the work presented in [42] is presented. SIE - MoM technique was also applied to the 100 minute rain event recorded by 2-D video disdrometer. The recorded rain event contained significant percentage of the oscillating drops which surface models were obtained using the nodes output by the reconstruction process. Scattering calculations of radar variables were computed and compared to the values measured by radar, showing advantage of accurately modeling asymmetric water precipitation particles.

This dissertation is organized as follows. Double higher order two dimensional Finite Element Method is presented in the first chapter following the Generalized Scattering Matrix computation by double higher order three dimensional Finite Element Method and Mode Matching Technique. The novel extraction integration technique is presented in the third chapter followed by the Multi-Level Fast Multipole Method applied to double higher order Surface Integral Equation in the fourth chapter. The dissertation is concluded following the Integral Equation application to scattering calculations for asymmetric rain drops during a line convection event presented in the fifth chapter.

1 TWO DIMENSIONAL FINITE ELEMENT METHOD FOR EIGENVALUE SOLUTION OF THE WAVEGUIDE CROSS SECTION

1.1 Introduction

Two dimensional (2-D) solution of Wave equation computed by Finite Element Method (FEM) has been established as a general tool in applied electromagnetic area especially in analysis of waveguide cross-sections with arbitrary geometry to obtain propagation coefficients [53]-[62] and modal field distribution which notably impacts General Scattering Matrix (GSM) computation for passive waveguide structures, Chapter 2, [71],[74]-[80],[90]-[104]. 2-D FEM analysis of waveguide structures has been established with tangential vector finite elements [54]-[57], [63], covariant-projection elements [58], and higher order field approximations [58]-[62], all leading to accurate and efficient solutions. The higher order basis functions enable large domain modeling i.e. element size is of the order λ in each dimension (λ is wavelength in medium) [62], unlike low order modeling where element size is limited to $\lambda/10$. In [62], higher order Lagrange-type curvilinear quadrilateral elements with higher order hierarchical polynomial curl-conforming vector basis functions show *p*-refinement advantages over *h*-refinement.

The work in this chapter resumes the method established in [62] using the same higher order geometrical and electric field modeling. The transformation from [56] is used to obtain final system of equation enabling TE and TM mode computation of waveguide cross-sections enclosed by means of perfect electric conductor (PEC). The details of the method are described in Section 1.2 and 1.3. The variable transformation is utilized leading to purely real system of equations for non-lossy medium enclosed by perfect electric conductor (PEC), which is solved by Lancosz method, outlined in Section 1.4, leading to excellent isolation of the modes with the same eigenvalue as well as decreasing the solution time by computing only requested number of modal

results. Results for PEC enclosed waveguides are presented in Section 1.5 while Sections 1.6 and 1.7 illustrate the solution for the waveguides enclosed by walls with finite conductivity, enabled by Standard Impedance Boundary Condition (SIBC) [148],[153]. The system of equation is changed to include SIBC enabling tunnel modeling by means of 3-D FEM in Chapter 2.

1.2 Two dimensional Wave equation Finite Element Method

In order to compute electric field distribution in waveguide cross section, vector wave equation is solved:

$$\nabla \times (\mu_r^{-1} \nabla \times \mathbf{E}) - k_0^2 \varepsilon_r \mathbf{E} = 0 , \tag{1.1}$$

where $\mathbf{E}$ is electric field modal solution, k_0^2 is eigenvalue solution for air-filled waveguide containing information of modal cut-off wave number, and μ_r and ε_r are permeability and permittivity of the material respectively. It is assumed that the waveguide structure is infinitely long and geometry variation depends just on two transversal dimensions (*x* and *y*) i.e. no variation is assumed along dimension normal to the geometry of the waveguide cross-section (*z*-axis), yielding following notation for electric field vector and dell operator[56],[62]:

$$\mathbf{E} = \mathbf{E}(x, y)e^{-\gamma z} = \mathbf{E}_t + E_z \mathbf{i}_z , \tag{1.2}$$

$$\nabla = \nabla_t - \gamma \mathbf{i}_z \tag{1.3}$$

where $\mathbf{E}_t$ represents components tangential to geometry and E_z is the component perpendicular to the geometry (i.e. in the direction of mode propagation), $\mathbf{i}_z$ is unit vector along *z*-axis and γ is the wave propagation constant.

Substituting equation (1.2) into (1.1), and using identity in (1.3), followed by moving k_0^2 dependencies to the right hand side and dividing equation components into parallel and transversal to the geometry, equations below are obtained:

$$\nabla_t \times (\mu_r^{-1} \nabla_t \times \mathbf{E}_t) - \gamma \mu_r^{-1} (\nabla_t E_z + \gamma \mathbf{E}_t) = k_0^2 \varepsilon_r \mathbf{E}_t , \tag{1.4}$$

$$\nabla_t \times (\mu_r^{-1} (\nabla_t E_z + \gamma \mathbf{E}_t) \times \mathbf{i}_z) = k_0^2 \varepsilon_r E_z \mathbf{i}_z . \tag{1.5}$$

Applying transformation from [56]: $\mathbf{e}_t = \gamma \mathbf{E}_t$ and $e_z = E_z$ ($\mathbf{e} = \mathbf{e}_t + e_z \mathbf{i}_z$) to (1.4)-(1.5) and multiplying them by γ and γ^2 respectively, equations to be solved yield:

$$\nabla_t \times (\mu_r^{-1} \nabla_t \times \mathbf{e}_t) - \gamma^2 \frac{1}{\mu_r} (\nabla_t e_z + \mathbf{e}_t) = k_0^2 \varepsilon_r \mathbf{e}_t , \tag{1.6}$$

$$\gamma^2 \nabla_t \times (\mu_r^{-1} (\nabla_t e_z + \mathbf{e}_t) \times \mathbf{i}_z) = \gamma^2 k_0^2 \varepsilon_r e_z \mathbf{i}_z , \tag{1.7}$$

where $k_0^2 = k_c^2 - \gamma^2$ is eigenvalue solution and $\mathbf{e}$ is corresponding eigenvector, k_c is cut off wave number and γ is propagation coefficient given as an input parameter.

Unknown vector is represented through the expansion of higher order hierarchical polynomial curl-conforming vector basis functions ($\mathbf{f}$) with *u* and *v* being local transversal components that are mapped to *x* and *y* coordinates, while *z* is component perpendicular to the geometrical cross-section of the waveguide. Applying Galerkin testing procedure (i.e. testing functions are the same as basis functions), assuming that medium is non-magnetic and the waveguide walls are represented by means of perfect electric conductor (PEC) final system of equations becomes:

$$\int_S \mu_r^{-1} (\nabla_t \times \hat{\mathbf{f}}_t) \cdot (\nabla_t \times \mathbf{e}_t) dS - \gamma^2 \int_S \mu_r^{-1} \hat{\mathbf{f}}_t \cdot \nabla_t e_z dS - \gamma^2 \int_S \mu_r^{-1} \hat{\mathbf{f}}_t \cdot \mathbf{e}_t dS = k_0^2 \int_S \varepsilon_r \hat{\mathbf{f}}_t \cdot \mathbf{e}_t dS , \tag{1.8}$$

$$\gamma^2 \int_S (\nabla_t \times \hat{\mathbf{f}}_z) \cdot \mu_r^{-1} (\nabla_t e_z \times \mathbf{i}_z) dS + \gamma^2 \int_S (\nabla_t \times \hat{\mathbf{f}}_z) \cdot \mu_r^{-1} (\mathbf{e}_t \times \mathbf{i}_z) dS = \gamma^2 k_0^2 \int_S \varepsilon_r \hat{\mathbf{f}}_z \cdot e_z \mathbf{i}_z dS , \tag{1.9}$$

where *S* is area of the waveguide cross-section, $\hat{\mathbf{f}}_{t/z}$ represents testing functions transversal / normal to the waveguide geometry. The integrals in (1.8) and (1.9) are mapped to the local *u*-*v* domain

and evaluated numerically using Gauss-Legendre quadrature with NGL_u and NGL_v being the input parameters representing number of integration points along u and v local coordinates respectively.

1.3 Higher-Order Geometrical Elements and Basis Functions

A generalized hexahedron and quadrilateral in Fig. 1.1 are used as the tessellation unit for geometry approximation of the 3-D and 2-D structures respectively. The curvilinear hexahedron or quadrilateral is determined by $M = (K_u+1)(K_v+1)(K_w+1)$ arbitrarily positioned points, with K_u, K_v and K_w (K_u, K_v, $K_w \geq 1$) being geometrical orders of the element along u-, v- and w- parametric coordinates, mapping the element into parametric cube or square [70],[62], respectively. Therefore, position vector of the points in the element can be defined as follows:

$$\mathbf{r}(u,v,w) = \sum_{i=1}^{M} \mathbf{r}_i p_i(u,v,w) = \sum_{k=0}^{K_u} \sum_{l=0}^{K_v} \sum_{m=0}^{K_w} \mathbf{r}_{klm} u^k v^l w^m \ , \ -1 \leq u,v,w \leq 1 \, , \tag{1.10}$$

where $\mathbf{r}_1$, $\mathbf{r}_2$, …, $\mathbf{r}_M$ are the position vectors of the interpolation points and $p_i(u,v,w)$ are Lagrange-type interpolation polynomials. The parametric coordinates u_j, v_j and w_j represent the local locations of the j-th node, and $\mathbf{r}_{klm}$ are constant vector coefficients derived from $\mathbf{r}_1$, $\mathbf{r}_2$ … $\mathbf{r}_M$.

Curl-conforming hierarchical polynomial vector basis functions ($\mathbf{f}$) are defined as

$$\begin{aligned}
\mathbf{f}_{uijk}(u,v,w) &= \frac{u^i P_j(v) P_k(w)}{J(u,v,w)} \mathbf{a}_u^{\cdot}(u,v,w) \\
\mathbf{f}_{vijk}(u,v,w) &= \frac{P_i(u) v^j P_k(w)}{J(u,v,w)} \mathbf{a}_v^{\cdot}(u,v,w) \\
\mathbf{f}_{wijk}(u,v,w) &= \frac{P_i(u) P_j(v) w^j}{J(u,v,w)} \mathbf{a}_w^{\cdot}(u,v,w)
\end{aligned} \quad , \quad P_i(u) = \begin{cases} 1-u, & i=0 \\ u+1, & i=1 \\ u^i - 1, & i \geq 2, \text{even} \\ u^i - u, & i \geq 3, \text{odd} \end{cases} , \quad -1 \leq u,v,w \leq 1 , \tag{1.11}$$

where N_u, N_v and N_w are the degrees of the polynomial electric field approximation [70]. The reciprocal unitary vector $\mathbf{a}_u^{\cdot}$ in (1.11) is calculated as

$$\mathbf{a}_u^{\cdot}(u,v,w) = \frac{\mathbf{a}_v(u,v,w) \times \mathbf{a}_w(u,v,w)}{J(u,v,w)} \text{, where } \mathbf{a}_u(u,v,w) = \frac{\partial \mathbf{r}(u,v,w)}{\partial u} , \tag{1.12}$$

$\mathbf{a}_u$ being unitary vector, with $\mathbf{r}$ given by equation (1.10), and $J(u,v,w)$ is the Jacobian of the covariant transformation:

$$J(u,v,w) = \left(\mathbf{a}_u(u,v,w) \times \mathbf{a}_v(u,v,w)\right) \cdot \mathbf{a}_u(u,v,w) \,. \tag{1.13}$$

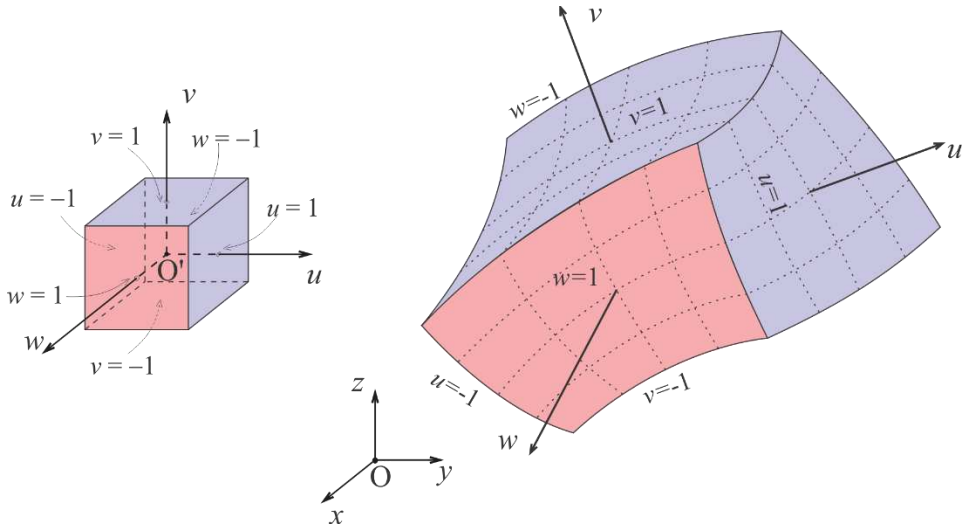

Fig. 1.1. A generalized parametric hexahedron and quadrilateral conforming to one of its sides.

Unknown electric field vector in the 3-D structure is represented through following expansion [70]:

$$\mathbf{E} = \sum_{i=0}^{N_u-1}\sum_{j=0}^{N_v}\sum_{k=0}^{N_w} \alpha_{uijk}\,\mathbf{f}_{uijk}(u,v,w) + \sum_{i=0}^{N_u}\sum_{j=0}^{N_v-1}\sum_{k=0}^{N_w} \alpha_{vijk}\,\mathbf{f}_{vijk}(u,v,w) + \sum_{i=0}^{N_u}\sum_{j=0}^{N_v}\sum_{k=0}^{N_w-1} \alpha_{wijk}\,\mathbf{f}_{wijk}(u,v,w) \,. \tag{1.14}$$

The 2-D unknown is represented as [62]:

$$\mathbf{e} = \sum_{i=0}^{N_u-1}\sum_{j=0}^{N_v} \alpha_{uij}\,\mathbf{f}_{uij}(u,v) + \sum_{i=0}^{N_u}\sum_{j=0}^{N_v-1} \alpha_{vij}\,\mathbf{f}_{vij}(u,v) + \sum_{i=0}^{N_u}\sum_{j=0}^{N_v} \alpha_{zij}\,\mathbf{f}_{zij}(u,v) \,, \tag{1.15}$$

where α represents eigenvectors from the eigenvalue problem solution and $\mathbf{f}_{zij}(u,v) = \mathbf{f}_{wijk}(u,v,w)$ for $K_w = 0$, $w = 0$ and $\mathbf{a}_u = \mathbf{i}_z$. The mixed-order arrangement in (1.14) and (1.15), where the expansion orders in different directions are intentionally left uneven, is in agreement with the reduced-gradient criterion.

1.4 Lanczos method – eigenvalue problem solution

The system of equations in (1.8) - (1.9) has a form of generalized eigenvalue problem:

$$[A]x = \lambda[B]x, \tag{1.16}$$

where [*B*] matrix is positive definite and both [*A*] and [*B*] matrices are real and symmetric, λ and *x* represent eigenvalue and corresponding eigenvector [64]. Eigenvalues and eigenvectors solution to (1.16) are computed iteratively using Lanzcos method, an orthogonal projection method onto Krylov subspace [65] that reduces dense matrix into Hessenberg form. In the case of real symmetric matrices, Hessenberg matrix is symmetric, real and tridiagonal with ζ_j and ξ_j being diagonal and sub diagonal elements. The eigenvalue problem in (1.16) is a good candidate to obtain the solution by shift and invert Lanczos algorithm [66] that solves a standard eigenvalue problem formulation described as:

$$[B][A - \sigma B]^{-1} s = \theta s, \tag{1.17}$$

where σ is a shift, θ and *s* represent eigenvalue and corresponding eigenvector relating to the original eigenvalue problem in (1.16) as $\lambda = \sigma + \theta^{-1}$ and $x = [W]\boldsymbol{s}$, where [*W*] is [*B*] orthogonal Krylov subspace basis functions. The shift updating is implemented to decrease the execution time having in mind known feature of the algorithm that the smallest eigenvalues converge first (i.e. eigenvalues of the original problem that are closest to the shift will be computed).

The Algorithm 1.1 [64] shows the steps in the algorithm for generalized eigenvalue problem for real and symmetric matreces. w_j and v_j represent j-th columns of [*W*] and [*V*] matrices that represent [*B*] and $[B]^{-1}$ orthogonal Krylov subspace basis functions respectively. Starting vector *r* is chosen such that elements corresponding to the transversal components have value one and elements correlating to the component normal to the geometry are zero valued [60] which enables TE/TM mode isolation for the same eigenvalue solution.

Algorithm 1.1 Shift and invert Lanczos algorithm for generalized real symmetric eigenvalue problem.

1. Choose starting vector r. Compute $q = [B]r$ and $\xi_0 = |q^T r|^{1/2}$
2. For j = 1,2,…, until convergence,
3. $w_j = r/\xi_{j-1}$, $v_j = q/\xi_{j-1}$
4. $r = [A - \sigma B]^{-1} v_j$
5. $r = r - w_{j-1}\xi_{j-1}$
6. $\zeta_j = v_j^T r$
7. $r = r - w_j \zeta_j$
8. Apply Gram-Schmidt orthogonalization process until vector r is $[B]$ orthogonal to $[V]$ matrix and to all converged eigenvectors.
9. multiply $q = [B]r$
10. $\xi_j = |q^T r|^{1/2}$
11. compute approximate eigenvalues
12. test for convergence
13. end for
14. compute approximate eigenvectors

1.5 Numerical Results and Discussion for 2-D PEC waveguides

1.5.1 Cross-section of the circular waveguide filled with air

The cylindrical waveguide cross-section with 1 mm radius is modeled by one and five second order elements. For the one element model, the basis orders are set to $N_u = N_v = 8$ (1.15) and Gauss Legendre integration points in each dimension are $NGL_u = NGL_v = 20$, while $N_u = N_v = 4$ and $NGL_u = NGL_v = 8$ for the five element model. In both cases inputs to Lancosz algorithm (Section 1.4) are $\gamma = j1000$ m^{-1} and $\sigma = 10^6$ m^{-1}. Dominant mode electric field vector pattern is given in Fig. 1.2.

1.5.2 Cross-section of the rectangular waveguide filled with air

The model of the air-filled waveguide cross-section with $a = 6$ m and $b = 4$ m is modeled by six square elements. Numerical parameters are set to $N_u = N_v = 6$ with 589 of unknowns. Inputs to Lancosz algorithm (Section 1.4) are $\gamma = j1$ m^{-1}, $\sigma = 1$ m^{-1} and error marking convergence in the Algorithm 1.1 is 10^{-14}. The relative error of the lowest fifteen eigenvalue solutions versus its values is represented in Fig. 1.3.

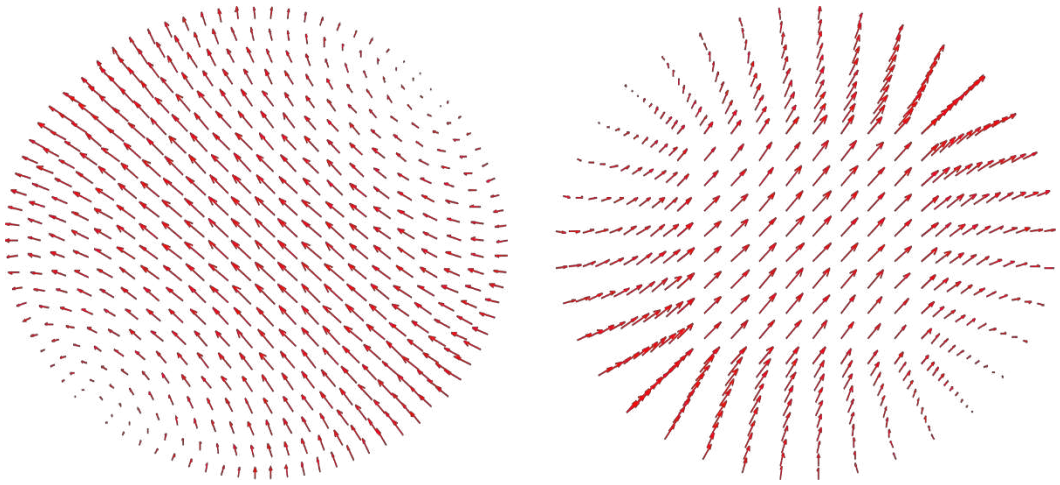

Fig. 1.2. Transversal electric field vector for TE_{11} (dominant) mode in the circular waveguide cross-section modeled with one (left) and five (right) second order geometrical elements.

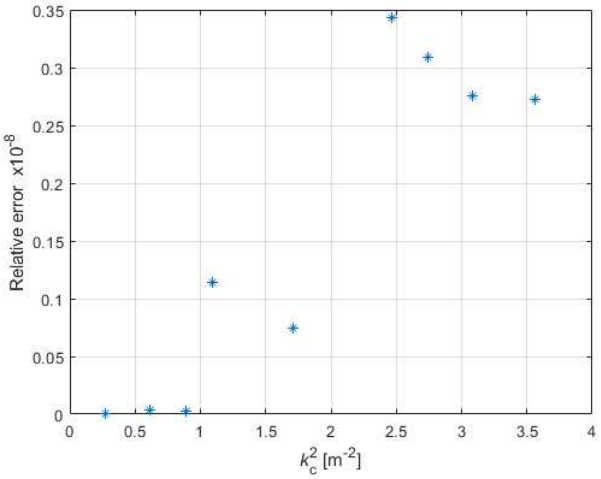

Fig. 1.3. Eigenvalue relative error.

The field pattern results, obtained from eigenvector solution and illustrated in Fig. 1.4 show TE modal solution perfectly isolated from the TM mode with the same eigenvalue. This is achieved by executing algorithm twice, obtaining only eigenvalue solutions in the first run. When the algorithm is executed for the second time, it is restarted often and the shift is updated with using the information about eigenvalues from the initial run. In the case when multiple TE modes have the same eigenvalue solution, example given in Fig. 1.5, the error of zero components is lower than 10^{-8}.

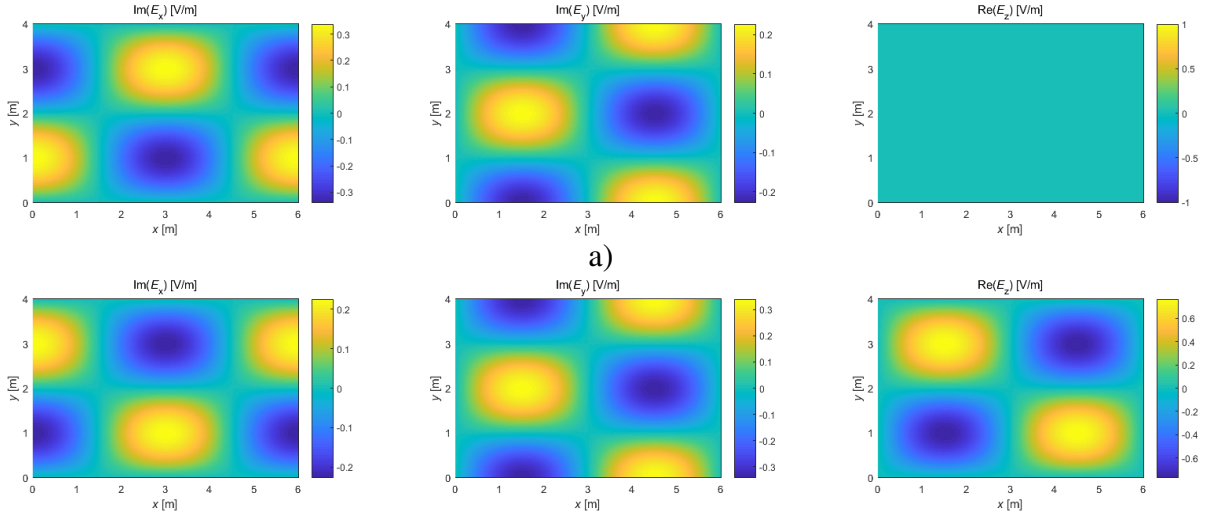

Fig. 1.4. Modal patterns for rectangular PEC waveguide for (a) TE_{22}, (b) TM_{22} modes.

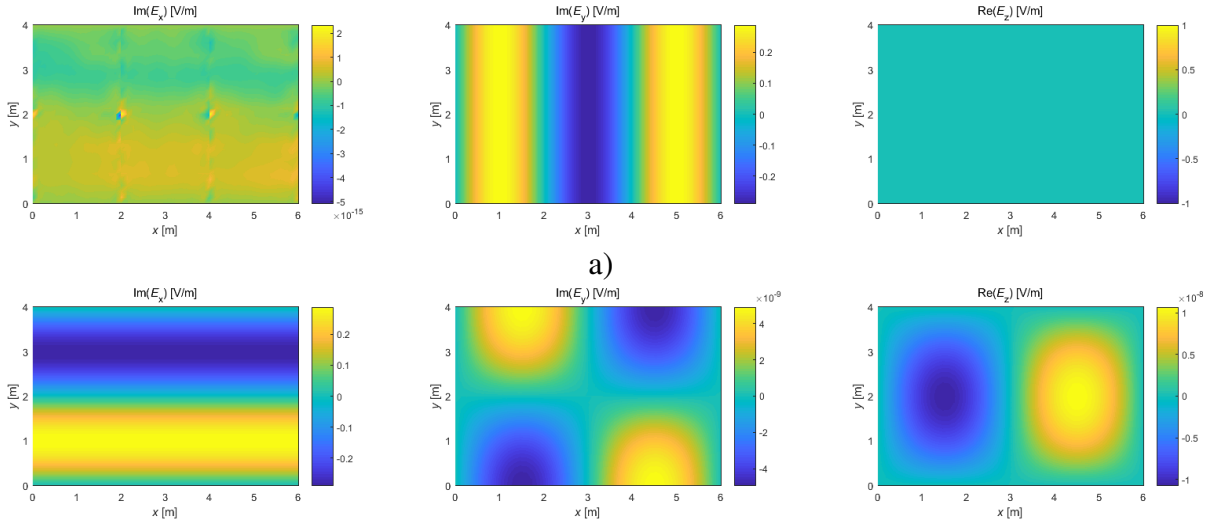

Fig. 1.5. Modal patterns for rectangular PEC waveguide for (a) TE_{30}, (b) TE_{02} modes.

1.6 Conductive waveguide walls and Standard Impedance Boundary condition

In the case where waveguide walls cannot be represented by perfect electric conductor (PEC), the computational domain is truncated by means of Standard Impedance Boundary Condition (SIBC). This is simple, i.e. first order, impedance boundary condition and it assumes that electromagnetic fields are confined to a layer with small thickness, much smaller than the

thickness of the conductive medium. SIBC connects tangential components of the magnetic and electric field inside and at the surface of the conductive material, so called Leontovich impedance boundary condition [148],[149],[153]:

$$\mathbf{n}\times\mathbf{n}\times\mathbf{E} = -Z(f)\mathbf{n}\times\mathbf{H}, \tag{1.18}$$

where **n** is outward normal at the conductive surface, i.e. the normal is directed from the discretized element into the conductive material. $Z(f)$ is impedance of the wall and it is defined as $Z(f) = C_{\mathrm{CW}}\sqrt{\mathrm{j}2\pi f\mu_0/(\sigma_{\mathrm{w}} + \mathrm{j}2\pi f\varepsilon_{\mathrm{w}})}$, where σ_{w} and ε_{w} are respectively conductivity and dielectric permittivity of the wall material and C_{CW} is coefficient describing the corrugation of the surface between wall and air [149].

The equations (1.8) and (1.9) are then expanded to include line (boundary) integral of the magnetic field which is introduced after Galerkin testing and transfer of the curl operator from basis to testing function. They are represented in the following form:

$$\gamma^2\int_S \mu_{\mathrm{r}}^{-1}\hat{\mathbf{f}}_{\mathrm{t}}\cdot\left(\nabla_{\mathrm{t}}e_{\mathrm{z}} + \mathbf{e}_{\mathrm{t}}\right)\mathrm{d}S = \int_S \mu_{\mathrm{r}}^{-1}(\nabla_{\mathrm{t}}\times\hat{\mathbf{f}}_{\mathrm{t}})\cdot(\nabla_{\mathrm{t}}\times\mathbf{e}_{\mathrm{t}})\mathrm{d}S - \mathrm{k}_0^2\int_S \varepsilon_{\mathrm{r}}\hat{\mathbf{f}}_{\mathrm{t}}\cdot\mathbf{e}_{\mathrm{t}}\mathrm{d}S + \mathrm{j}k_0R\int_{l_{\mathrm{I}}}(\mathbf{n}\times\hat{\mathbf{f}}_{\mathrm{t}})\cdot(\mathbf{n}\times\mathbf{e}_{\mathrm{t}})\mathrm{d}l\,, \tag{1.19}$$

$$\gamma^2\left(\int_S(\nabla_{\mathrm{t}}\times\hat{\mathbf{f}}_{\mathrm{z}})\cdot\mu_{\mathrm{r}}^{-1}(\nabla_{\mathrm{t}}e_{\mathrm{z}} + \mathbf{e}_{\mathrm{t}})\times\mathbf{i}_{\mathrm{z}}\mathrm{d}S - \mathrm{k}_0^2\int_S \varepsilon_{\mathrm{r}}\hat{\mathbf{f}}_{\mathrm{z}}\cdot e_{\mathrm{z}}\mathbf{i}_{\mathrm{z}}\mathrm{d}S + \mathrm{j}k_0R\int_{l_{\mathrm{I}}}(\mathbf{n}\times\hat{\mathbf{f}}_{\mathrm{z}})\cdot(\mathbf{n}\times\mathbf{e}_{\mathrm{z}})\mathrm{d}l\right) = 0\,, \tag{1.20}$$

where R is frequency dependent coefficient and represents the ratio between air impedance and the waveguide wall impedance. The new system of equations in (1.19)-(1.20) in the form of (1.16) gives propagation coefficient (γ) as unknown (eigenvalue) while [B] matrix is positive definite and both [A] and [B] matrices are complex and symmetric.

1.7 Numerical Results and Discussion for 2-D waveguides enclosed by SIBC

1.7.1 Cross-section of the rectangular waveguide filled with air

Rectangular waveguide cross-section with a = 4 m and b = 3 m dimensions is modeled by first order elements with 1 m^2 area. Operating frequency is 1 GHz and orders of the basis functions are $N_u = N_v = 8$ with number of Gauss-Legendre integration points $NGL_u = NGL_v = 12$. The waveguide wall material is represented via SIBC with conductivity σ_w = 0.01 S/m, relative dielectric constant $\varepsilon_{rw} = 0$, and corrugation coefficient $C_{CW} = 1$, i.e. walls are smooth. The twenty lowest eigenvalue solutions are compared with the results obtained by HFSS using SIBC in Fig. 1.6 and the absolute value of electric field modal solutions for first three dominant modes is displayed in Fig. 1.7.

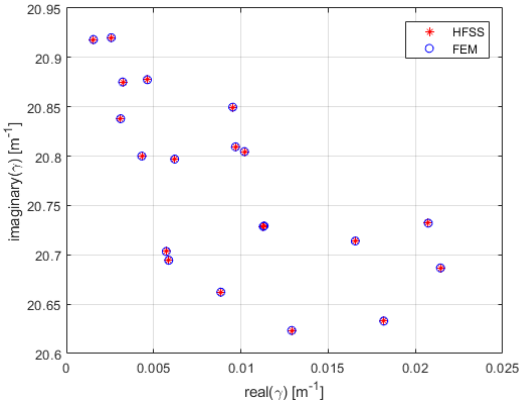

Fig. 1.6. Propagation constant comparison for the 20 most dominant modes.

1.7.2 Massif Central tunnel cross-section

In order to verify the method by comparing results with HFSS ANSYS [106], the tunnel walls are represented by SIBC with σ_w = 0.01 S/m, ε_{rw} = 0 and smooth walls at 900 MHz. The FEM model for the curved geometry of the arched tunnel in Fig. 1.8(a) is tasseled with 40 air filled 2nd order geometrical elements. Basis functions orders per element are $N_u = N_v = 4$, with integration parameters $NGL_u = NGL_v = 8$, giving overall number of 2-D unknowns to be 2001. Twenty lowest propagation coefficients, derived from eigenvalue solutions, are compared to results obtained by

HFSS in Fig. 1.9. Arched line of model 1 in HFSS is modeled as part of the circle approximated by as 50 straight sections, while the approximation of arch in model 2 is twice refined. It can be noted that FEM results compare better to the model 2 than model 1 results, as expected.

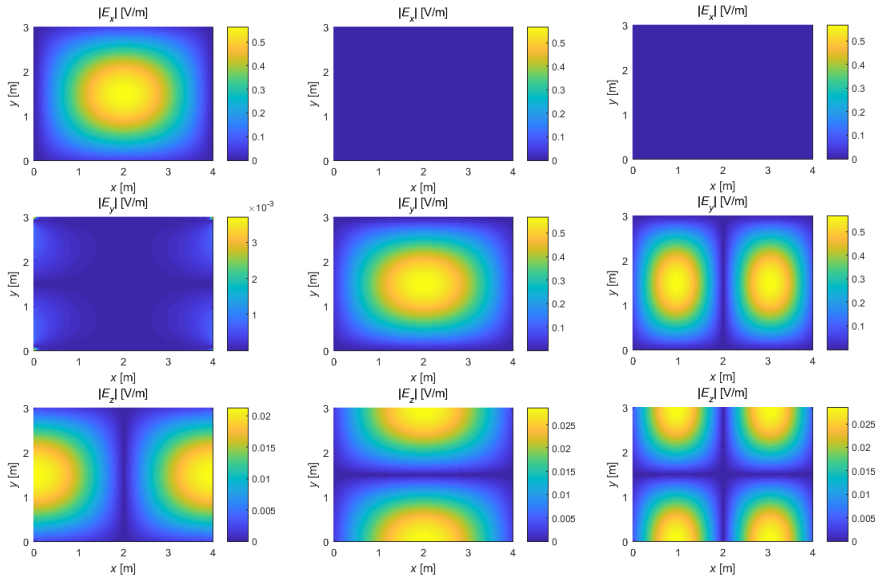

Fig. 1.7. Absolute value of electric field modal solutions at waveguide cross-section for the 3 most dominant modes, left to right.

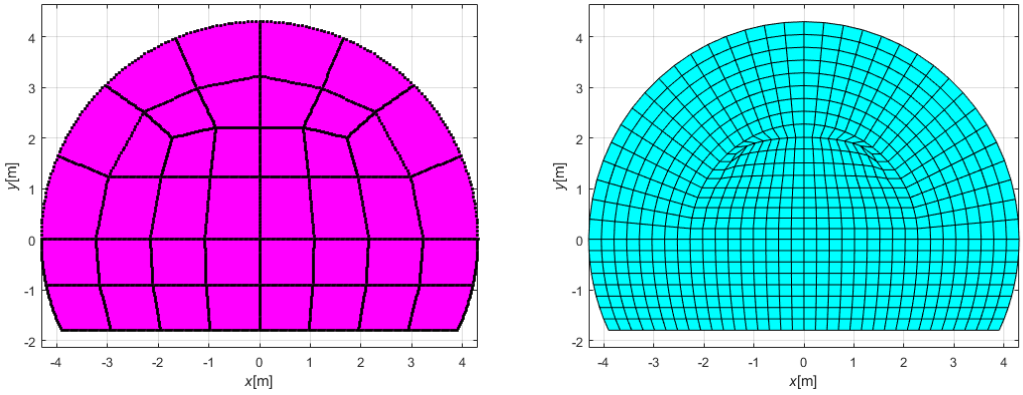

a) b)

Fig. 1.8. Geometry of the models representing cross-section of arched tunnel (a) 40 element model (b) 722 element model.

To accurately model Massif Central tunnel cross-section, the walls are represented via SIBC with $\sigma_w = 0.01$ S/m and $\varepsilon_{rw} = 5$ [151]. The curved geometry of the tunnel is modeled with 722 2nd order geometrical elements, shown in Fig. 1.8(b) with basis function orders per element being $N_u = N_v = 2$. Derived from eigenvalue solutions, the twenty lowest propagation coefficients

are graphed in Fig. 1.10 at operating frequencies 450 and 900 MHz, for two different values of corrugation factor which represents corrugation of the tunnel wall. Implicitly, it can represent the correction factor for the values of conductivity and dielectric permittivity of the wall material in the case of the smooth wall. Accuracy and appropriate computation of eigenvalue solutions in the tunnel model leads to correct estimation of the attenuation of the signal. At 450 MHz, absolute value of the electric field modal solutions obtained from eigenvectors of the three most dominant modes are plot in Fig. 1.11, showing similar pattern behavior to the solutions in rectangular cross section in Fig. 1.7, especially in the central area of the cross-section. This is the reason it is a common practice to model arched tunnels by means of rectangular cross-section, but it does not provide satisfactory accuracy when modeling electric field close to the edge of the tunnel.

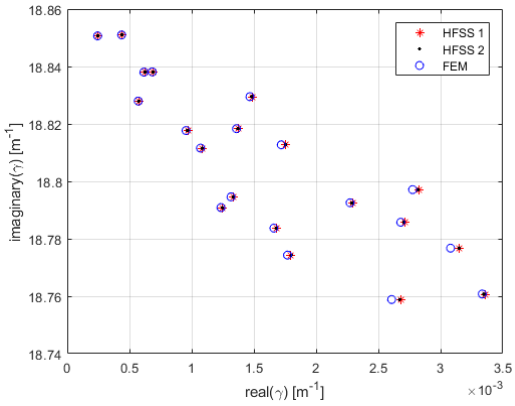

Fig. 1.9. Propagation coefficient comparison for arched tunnel.

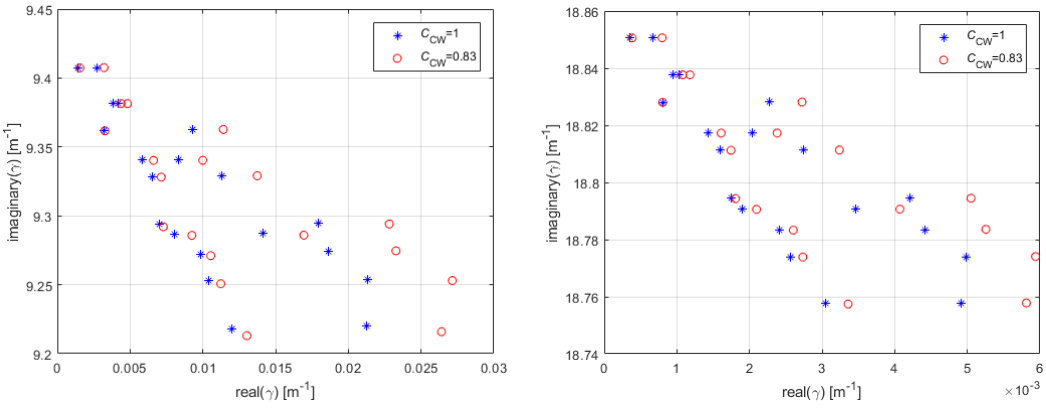

a) b)

Fig. 1.10. Eigenvalue solutions at (a) 450 MHz, (b) 900 MHz for two different corrugation factors.

1.8 Conclusion

Double Higher Order 2-D FEM eigenvalue solver has been developed for waveguides with both PEC and finite conductivity boundaries, with the purpose of utilizing it in GSM computation detailed in Chapter 2. The results have been verified with both analytic, Figs. 1.2-1.5, and industrial standard (ANSYS HFSS [106]) employing low order geometrical elements, Fig. 1.6 and Fig. 1.9. Lanczos method has been implemented for generalized real symmetric eigenvalue problems and its' benefits have been demonstrated in isolation of TE from TM modes in PEC waveguides.

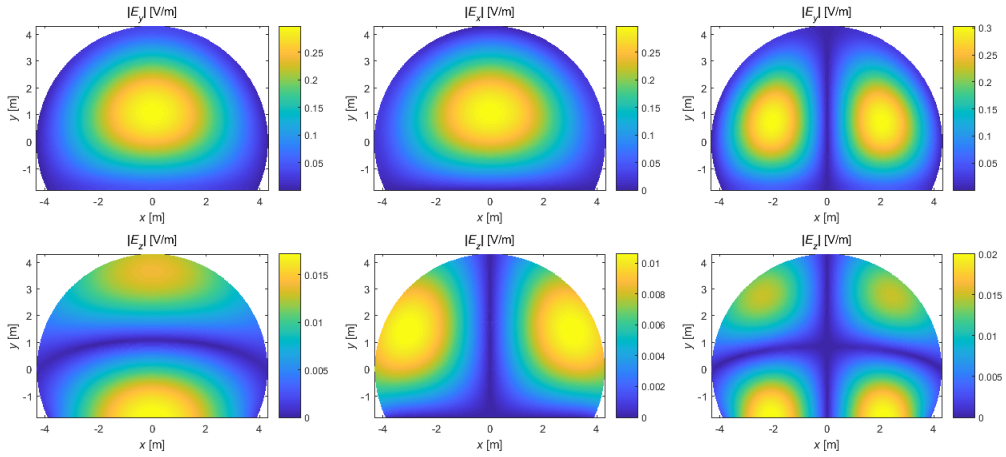

Fig. 1.11. Absolute value of electric field modal solutions for the three most dominant modes, left to right at 450 MHz and $C_{CW} = 0.83$.

2 GENERALIZED SCATTERING MATRIX COMPUTATION FOR WAVEGUIDE STRUCTURES USING FINITE ELEMENT MODELING AND MODE MATCHING TECHNIQUE

2.1 Introduction

Design, analysis and optimization of the three-dimensional waveguide-type microwave devices highly depends on accurate full wave numerical simulations of the electric/magnetic field distribution inside the structure. Method of moments (MoM), finite difference time domain (FDTD) and mode matching (MM) are widely used in the area. Finite element method (FEM) has shown powerful capabilities in analyzing waveguide structures with inhomogeneous, dielectric and metallic arbitrarily shaped discontinuities [69]. In order to decrease the memory needed for the analysis of large waveguides, segmentation of the structure's domain was proposed [74]. Many research groups base their waveguide segmentation method on multimode multiport matrix that describes each subdomain and connects them into the original structure. Each subdomain is analyzed by FEM and the Generalized Scattering Matrix (GSM) is computed via mode matching (MM).

Low order elements, e.g. tetrahedral/triangular elements, are widely present in waveguide modeling discretizing FEM domain [96]-[98], which is then applied in FEM/MM method to waveguide discontinuities and filters. During previous decade [99],[100], 2-D solution for modal expansion (Lanczos solution) and arbitrarily shaped waveguides giving theoretical background for analysis of inhomogeneous cross-sections were developed leading to employing hybrid MM methods in conjunction with FEM / MoM / Finite Difference(FD). In [104], edge-based Whitney's vector functions are employed. Scattering from 3-D cavities in [92],[93] uses FEM or MoM to compute GSM in different subdomains using integral equation method with Rao–Wilton–Glisson

(RWG) basis functions for the exterior unbounded domain while interior bounded part is solved with FEM that is modeled by means of tetrahedral curl conforming edge-element functions (Nedelec). In tetrahedral elements tree-cotree splitting obtained improvement in the efficiency and the stability of the adaptive mesh refinement process [55],[57],[101], later work using hierarchical higher order basis functions. Additionally to Mode Matching method combined with FEM and MoM obtaining GSM/GAM, there are advances in FDTD/MM area [102]-[103].

Curvilinear elements are used in [71], i.e. covariant projection elements discretize FEM domain to compute Generalized Admittance Matrix (GAM) using FEM-MM. They applied the symmetric Padé via Lanczos process [75],[76],[79] to obtain reduced-order model of the transfer function, the GAM can be evaluated at any frequency, reducing the computational time. Selleri analyzes horn antenna using FEM-MM and planar wave expansion to compute GSM [87] using curved triangular and tetrahedral elements that are defined by rational Bézier mapping and higher order interpolatory vector basis functions [88],[89]. In [103], hierarchical higher order basis functions are used with the inexact Helmholtz decomposition and tree-cotree splitting to improve the efficiency and the stability of the adaptive mesh refinement process.

Antenna design with spherical mode expansion on the absorbing boundaries has been popularly utilized [76]-[78],[80],[82]-[85],[94],[95]. By introducing Floquet mode expansion to the method [94],[95] analyzing antenna arrays or periodic structures becomes less expensive. Floquet-Bloch decomposition enabled infinite periodic structures analysis [81]. Domain decomposition coupled with GSM computation enables faster technique for the analysis of microwave devices [90],[91],[94].

Additionally to waveguide segmentation, FEM/MM enables accurate and efficient solution to short waveguide structures with discontinuities. In order to obtain dominant or multi-mode

solution for short structures, where the discontinuities are close to the ports, higher modes need to be included in the computation for appropriate boundary condition.

In this chapter hierarchical polynomial vector basis functions of arbitrarily high orders have been used to model the electric field in the domain of interest, as well as Lagrange-type curved hexahedral finite elements of higher geometrical orders for modeling the arbitrarily shaped structures [67],[68]. The technique shows to be highly efficient and accurate for a small number of curved hexahedral elements leading to the reduced number of unknowns compared to low-order discretization.

The idea behind presented technique, based on already developed higher order finite element method [68], is to decrease the memory usage needed for solving FEM matrix system that describes large waveguide structures by decomposing the structure into smaller waveguide forms. The original waveguide system is divided into a number of arbitrarily shaped subsystems analyzed completely independently reducing the memory required for the computation. The result of analysis is Generalized Scattering Matrix (GSM) computation and storage for each subdomain separately. The GSM relations of all subsystems are combined into a system of linear equations that gives solution to the original waveguide and electromagnetic field inside the structure can be computed if needed.

This chapter is organized as follows. The details of the methodology are given in Section 2.2 and 2.3. Method verification and the benefits of Double Higher Order (DHO) modeling are outlined in Section 2.4, presenting the results for PEC enclosed waveguides. Sections 2.5 illustrates the results for the waveguides enclosed by boundary with finite conductivity, enabled by Standard Impedance Boundary Condition (SIBC) in order to model mines and underground tunnels. Long rectangular tunnel (waveguide) is modeled and results are compared to commonly used Vector

Parabolic Equation in order to verify the implementation. Benefits of DHO FEM-MM-GSM over other commonly used methods in tunnel modeling are used in simulating electromagnetic field, mainly the fact that model can be subdivided and sections separately simulated. The other benefit is higher order modeling, elements approximating curved and arched geometries fairly accurately while broadly used methods usually use rectangular approximations. These advantages are presented in modeling communication system in Massif Central tunnel.

2.2 Segmentation of the waveguide structure

Consider a 3-D *N*-port waveguide structure with arbitrarily shaped metallic and/or dielectric discontinuities in Fig. 2.1. Dividing the structure into waveguide subdomains (subsystems) by introducing fictitious planar surfaces, S_i, between two subsystems, enables analysis of each subdomain separately. Same kinds of surfaces are introduced at the actual ports of the waveguide system which truncates the domain of computation obtaining the closed structure [69]. In the same manner, the planar surfaces (which can be viewed as subsystem ports) are part of the bound of one subsystem making it a closed structure that can be analyzed using previously developed technique for waveguide structures [68],[69],[70]. In Fig. 2.1 first *N* fictitious planar surfaces are modeling subsystem ports that are also ports related to original waveguide structure, while the other fictitious surfaces are used to connect subsystems into the structure.

The closed structure of one subsystem (e.g. *n*-th subsystem shown in Fig. 2.2) is tessellated using generalized Lagrange-type curved parametric hexahedra of higher geometrical orders [68] shown in Fig. 1.1 and defined in (1.10). The electric field inside each of the hexahedra is expanded (1.14) using curl conforming higher order basis functions described in Section 1.3.

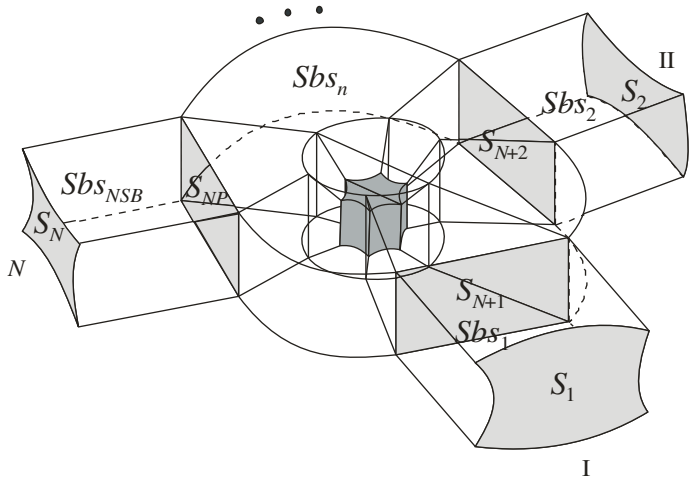

Fig. 2.1 Generic 3-D *N*-port waveguide structure divided into *NSB* number of subsystems (*Sbs*).

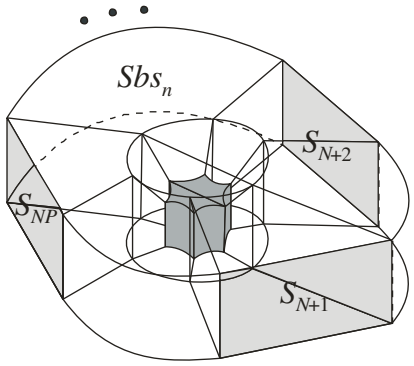

Fig. 2.2 Structure of *n*-th subsystem of the waveguide structure in the Fig. 2.1.

For the general subsystem in Fig. 2.2 that has the same properties as general waveguide structure [69], we invoke the curl-curl electric-field vector wave equation given in (1.1). A standard weak form of discretization yields [69]:

$$\int_V \mu_r^{-1}(\nabla\times\mathbf{f}_{\hat{i}\hat{j}\hat{k}})\cdot(\nabla\times\mathbf{E})\,\mathrm{d}V - k_0^2\int_V \varepsilon_r\mathbf{f}_{\hat{i}\hat{j}\hat{k}}\cdot\mathbf{E}\,\mathrm{d}V = \mathrm{j}k_0Z_0\oint_S \mathbf{f}_{\hat{i}\hat{j}\hat{k}}\cdot\mathbf{n}\times\mathbf{H}\,\mathrm{d}S\,, \tag{2.1}$$

where V is the volume of a generalized hexahedron, $\mathbf{f}_{\hat{i}\hat{j}\hat{k}}$ stands for testing functions $\mathbf{f}_{u\hat{i}\hat{j}\hat{k}}$, $\mathbf{f}_{v\hat{i}\hat{j}\hat{k}}$ or $\mathbf{f}_{w\hat{i}\hat{j}\hat{k}}$ which are $\mathbf{a}_u$, $\mathbf{a}_v$ or $\mathbf{a}_w$ directed respectively. Note that testing functions are the same as basis functions i.e. Galerkin testing procedure is used [70]. Surface S in (2.1) is the boundary surface of the hexahedron, and $\mathbf{n}$ is the outward unit normal ($\mathrm{d}\mathbf{S} = \mathbf{n}\mathrm{d}S$). Due to the continuity of the tangential component of the magnetic field intensity vector, $\mathbf{n}\times\mathbf{H}$ across the interface between

any two finite elements in the FEM model, the right-hand side term in (2.1) contains the surface integral over the overall boundary surface of the subsystem, and not over the internal boundary surfaces between the individual hexahedra in the model, which for the subsystem of waveguide problem in Fig. 2.2 reduces to the surface integral across the artificially introduced planar surfaces (subsystem ports) and metallic/conductive walls of the waveguide. Right hand side in (2.1) is represented as

$$\mathrm{j}k_0 Z_0 \oint_S \mathbf{f}_{\tilde{i}\tilde{j}\hat{k}} \cdot \mathbf{n} \times \mathbf{H} \, \mathrm{d}S = -\mathrm{j}k_0 R \int_{S_I} (\mathbf{n} \times \mathbf{f}_{\tilde{i}\tilde{j}\hat{k}}) \cdot (\mathbf{n} \times \mathbf{E}) \mathrm{d}S + \mathrm{j}k_0 Z_0 \int_{S_\mathrm{P}} \mathbf{f}_{\tilde{i}\tilde{j}\hat{k}} \cdot \mathbf{n} \times \mathbf{H} \mathrm{d}S \,, \tag{2.2}$$

where S_I represent surfaces of the hexahedron where Standard Impedance Boundary Condition (SIBC) is applied to the conductive walls in order to truncate the computational domain, details given in Section 1.6, and S_P represents surfaces of the ports. R is frequency dependent coefficient and represents the ratio between air impedance and the waveguide wall impedance (Section 1.6). In the case waveguide walls are modeled by PEC, first integral in the right hand side of (2.2) becomes zero.

In order to correctly introduce boundary condition at the ports of n-th subsystem, modal expansion method [69],[73] is applied. The tangential electric and magnetic fields at each of the subsystem ports are represented through linear combination of the incident and reflected modes existing at each of the cross-section. The expansion of the fields at one of the subsystem ports yields:

$$\mathbf{E}_\mathrm{t} = \sum_{m=1}^{N_\mathrm{m}} (a_m + b_m) \mathbf{e}_m(u,v) \,, \quad \mathbf{H}_\mathrm{t} = \sum_{m=1}^{N_\mathrm{m}} (b_m - a_m) \mathbf{h}_m(u,v) \,, \tag{2.3}$$

where $\mathbf{e}_m$ and $\mathbf{h}_m$ represent the transversal (tangential to the fictitious surface) electric and magnetic field components of the m-th mode on the given subsystem port, while a_m and b_m stand for the amplitudes ingoing and outgoing waves, respectively.

The electric filed vector modal forms at the subsystem ports are computed by 2-D higher-order eigenvalue FEM for waveguide cross-sections of arbitrary shapes (Chapter 1),[62], while magnetic field vector modal forms are computed from the electric filed modal pattern. The modal forms are obtained for all *NP* planar surfaces and then matched accordingly to the outward normal of each subsystem containing considered port surface, saving computational time.

Correlation between sets of *a* and *b* coefficients of the *n*-th subsystem is to be derived. Two following matrix equations are obtained by means of (2.1)-(2.3):

$$\left([A]-k_0^2[B]+\mathrm{j}k_0R[S]\right)\{\alpha\}=[P]\{a\}-[P]\{b\}\ ,\qquad [C]\{\alpha\}=[D]\{a\}+[D]\{b\}\ , \tag{2.4}$$

where the first matrix equation is based on substituting the 3-D electric-field expansion from (1.14) and 2-D magnetic-field modal expansion from (2.3) into (2.1) having in mind (2.2). The second equation in (2.4) is composed by imposing the continuity of the tangential electric field component expressed through 3-D FEM discretization (1.14) and modal expansion in (2.3) over the ports enclosing *n*-th subsystem and testing the electric field with modal forms. The elements of matrices [*A*] , [*B*] and [*S*] are computed as [70]:

$$a_{\tilde{i}\tilde{j}\hat{k}ijk}=\int_V \mu_{\mathrm{r}}^{-1}(\nabla\times\mathbf{f}_{\tilde{i}\tilde{j}\hat{k}})\cdot(\nabla\times\mathbf{f}_{ijk})\,\mathrm{d}V\ ,\ b_{\tilde{i}\tilde{j}\hat{k}ijk}=\int_V \varepsilon_{\mathrm{r}}\mathbf{f}_{\tilde{i}\tilde{j}\hat{k}}\cdot\mathbf{f}_{ijk}\,\mathrm{d}V\ ,\ s_{\tilde{i}\tilde{j}\hat{k}ijk}=\int_{S_{IBC}}(\mathbf{n}\times\mathbf{f}_{\tilde{i}\tilde{j}\hat{k}})\cdot(\mathbf{n}\times\mathbf{f}_{ijk})\,\mathrm{d}S \tag{2.5}$$

where *V* is the volume of a generalized hexahedron and $\mathbf{f}_{ijk}$ stands for the basis functions of any direction ($\mathbf{f}_{uijk}$, $\mathbf{f}_{vijk}$ or $\mathbf{f}_{wijk}$). The elements of matrices [*P*], [*C*], and [*D*] are obtained as [69]:

$$p_{\tilde{i}\tilde{j}\hat{k}m}=-\mathrm{j}k_0Z_0\int_S \mathbf{f}_{\tilde{i}\tilde{j}\hat{k}}\cdot(\mathbf{n}\times\mathbf{h}_m)\,\mathrm{d}S\ ,c_{\hat{m}ijk}=\int_S \mathbf{e}_{\hat{m}}\cdot\mathbf{f}_{ijk}\,\mathrm{d}S\ \text{ and }\ d_{\hat{m}m}=\int_S \mathbf{e}_{\hat{m}}\cdot\mathbf{e}_m\,\mathrm{d}S\ , \tag{2.6}$$

where the domain of integration (*S*) either coincides with a side of the generalized hexahedron belonging to the subsystem's port surface (in the first two integrals) or corresponds to the entire subsystem port (in the third integral). Integrals *p* and *c* in (2.6) are nonzero for testing/basis

functions that are nonzero at the subsystem port of interest. The integrals in (2.5) and (2.6) are mapped to the local *u*-*v*-*w* domain and evaluated numerically using Gauss-Legendre quadrature with NGL_u, NGL_v and NGL_w being the number of integration points along *u*, *v* and *w* local coordinates respectively.

2.3 Generalized Scattering Matrix

From sets of equations in (2.4), it is possible to obtain relation between outgoing (*b*) and ingoing (*a*) coefficients corresponding to analyzed subsystem. By representing α coefficients in the first equation as: $\{\alpha\} = \left([A] - k_0^2[B] + \mathrm{j}k_0 R[S]\right)^{-1} \cdot \left([P]\{a\} - [P]\{b\}\right)$ and substituting it in the second equation in (2.4), we obtain:

$$[C] \cdot \left([A] - k_0^2[B] + \mathrm{j}k_0 R[S]\right)^{-1} \cdot \left([P]\{a\} - [P]\{b\}\right) = [D]\{a\} + [D]\{b\}. \tag{2.7}$$

Generalized scattering matrix ($\{b\}=[GSM]\{a\}$) correlating amplitudes of all incident and reflected waves associated with the *n*-th subsystem is computed as following:

$$[GSM^n]^{-1} = ([C][FEM]^{-1}[P] - [D])^{-1}([C][FEM]^{-1}[P] + [D]), \tag{2.8}$$

where $[FEM] = [A] - k_0^2[B] + \mathrm{j}k_0 R[S]$. Note that [*GSM*] in (2.5), (2.6) and (2.7) depends on the frequency. Matrices needed for evaluation of [*GSM*] are computed without frequency dependence and stored. They are recalled, for each frequency, to compute [*GSM*] for each subsystem. All subsystems being solved, response of the original waveguide structure can be analyzed.

Ingoing waves of a subsystem are correlated just to the outgoing waves of the same subsystem via [GSM_n], subscript referring to the *n*-th subsystem. In order to compute Generalized Scattering Matrix of the original *N*-port structure in Fig. 2.1, all subsystems' coefficients need to be set in the system of equations. In Fig. 2.1, fictitious surface *SN*+1 is the boundary between the first and the *n*-th subsystems, meaning that outgoing waves at *SN*+1 from the first subsystem will

be equal to the ingoing waves to the *n*-th subsystem at *SN*+1 and vice versa. By representing all ingoing wave coefficients at the fictitious surfaces, that are not original waveguide ports, as outgoing wave coefficients of another subsystem and moving them to the left hand side of the equation, we obtain the system similar to the one in (2.9). These mathematical manipulations lead to all the values of the right hand side of the equation in (2.9) being zero, except coefficient values that correspond to the original waveguide ports. Final matrix equation, in (2.9), is obtained for each frequency where $\{a_n\}$ and $\{b_n\}$ are vectors of modes coefficients of the *n*-th subsystem.

$$\begin{bmatrix} [GSM_1]^{-1} & \cdots & \begin{bmatrix} 0 & 0 \\ -I & 0 \end{bmatrix} & \cdots \\ \vdots & \ddots & & \\ \begin{bmatrix} 0 & -I \\ 0 & 0 \end{bmatrix} & \cdots & [GSM_n]^{-1} & \cdots \\ \vdots & & \vdots & \ddots \end{bmatrix} \begin{Bmatrix} \begin{Bmatrix} b_{1@S_1} \\ b_{1@S_{N+1}} \end{Bmatrix} \\ \vdots \\ \begin{Bmatrix} b_{n@S_{N+1}} \\ b_{n@elsewhere} \end{Bmatrix} \\ \vdots \end{Bmatrix} = \begin{Bmatrix} \begin{Bmatrix} a_{1@S_1} \\ 0 \end{Bmatrix} \\ \vdots \\ \begin{Bmatrix} 0 \\ 0 \end{Bmatrix} \\ \vdots \end{Bmatrix} \tag{2.9}$$

The system matrix in (2.9) is the size N_m x N_m, where N_m is the number representing the sum of modes at each subdomain, which is much smaller then number of α coefficients in the field expansion over all elements of the original *N*-port waveguide structure. After solving matrix equation in (2.9) for *b* (outgoing wave) coefficients, it is straightforward to find all unknown *a* (ingoing wave) coefficients. The electric field distribution inside the waveguide (inside any subdomain) can be computed, if needed, by solving the first equation in (2.4) for α coefficients of that subdomain.

2.4 Numerical Results for 3-D waveguides enclosed by perfect electric conductor

2.4.1 Air-filled rectangular waveguide

The models in Fig. 2.3 are representing geometry with parameter values $a = 0.2\,\mathrm{m}$, $b = 0.1\,\mathrm{m}$, $l = 0.1\,\mathrm{m}$. The results in tables are obtained at frequency *f* = 1600MHz having the largest element size slightly larger than wavelength in air. Each subsystem is modeled by one 3-D

element with numerical parameters N_u=8, N_v=N_w=4, NGL_u=NGL_v=NGL_w=20, with u, v and w having direction of x, y and z respectively. Each port contains one 2-D element with N_u=N_v=6 and NGL_u=NGL_v=20 numerical parameters. For all the structures in Fig. 2.3, the port one (P1) is excited with TE_{01} and TE_{11} modes with unit amplitude. The outgoing coefficients at ports 2 to 4 (P2 – P4) for the structures in Fig. 2.3 (a) to (c) are given in Tables 2.1-2.3, respectively. The reflection coefficients at port 1 for both modes and all three structures, which are analytically evaluated to be zero, are computed to be less than 1E-3. The results are obtained for refined model of the structure in Fig. 2.3(a) divided along x direction, containing two cubical elements. Each port is modeled by two elements as well, with 3-D numerical parameters: N_u=N_v=N_w=4, NGL_u=NGL_v=NGL_w=14, and 2-D parameters, N_u=N_v=6 and NGL_u=NGL_v=20 showing the same accuracy as the result for non-refined model excited by TE_{10}.

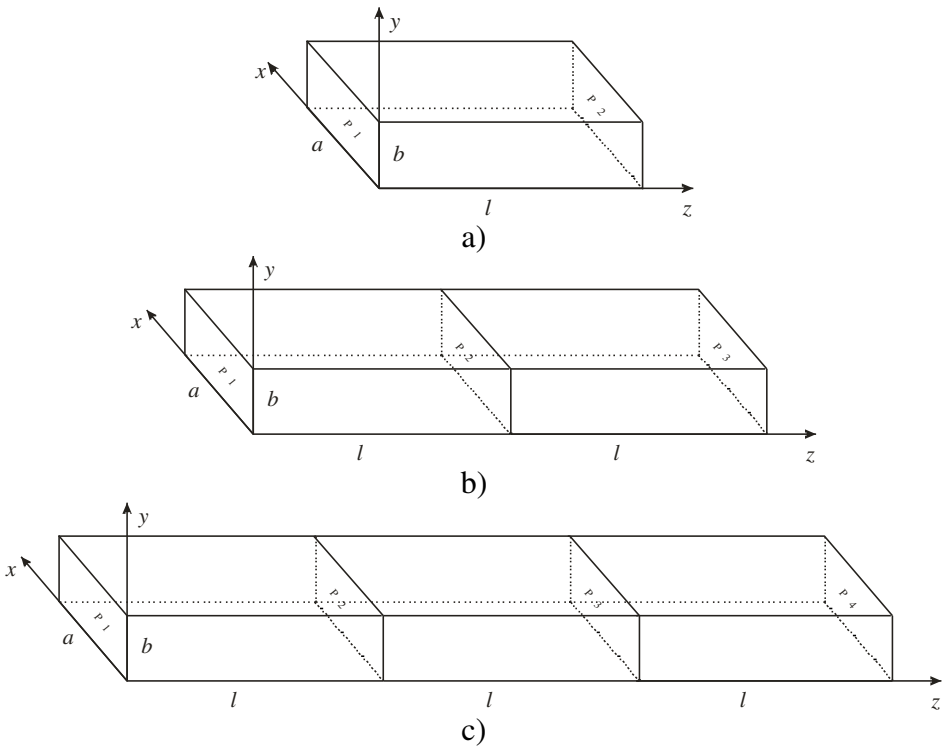

Fig. 2.3. Air filled rectangular waveguide models with (a) one, (b) two, and (c) three subsystems of length l.

TABLE 2.1. TE_{10} and TE_{11} mode outgoing coefficients at the port 2 with excitations at port 1 for the structure at Fig. 2.3(a).

mode	*b* coefficients	4 digit analytical values
TE_{10}	-0.983992215849992 - i0.178211255564046	-0.9840 - i0.1779
TE_{11}	0.387665181844883 - i0.921800251944533	0.3876 - i0.9218

TABLE 2.2. TE_{10} and TE_{11} mode outgoing coefficients at the port 3 with excitations at port 1 for the structure at Fig. 2.3(b).

mode	*b* coefficients	4 digit analytical values
TE_{10}	0.936481378306431 + i0.350716932186018	0.9367 + i0.3502
TE_{11}	-0.699431411222472 - i0.714699726888540	-0.6995 - i0.7146

TABLE 2.3. TE_{10} and TE_{11} mode outgoing coefficients at the port 4 with excitations at port 1 for the structure at Fig. 2.3(c).

mode	*b* coefficients	4 digit analytical values
TE_{10}	-0.858988618505138 - i0.511994136553759	-0.8594 - i0.5113
TE_{11}	-0.929955594830773 + i0.367671852713859	-0.9299 + i0.3678

2.4.2 Verification for model with dominant mode boundary condition

For the verification purposes, the results obtained by FEM method supporting only dominant mode rectangular waveguide analysis in [73],[62] were repeated by the FEM-MM method computing GSM for two structures given in Figs. 2.4 and 2.6. WR-62 waveguide structure in Fig. 2.4 is modeled by eight 2^{nd} order elements and two first order buffer elements at the ports. WR-90 waveguide structure in Fig. 2.6 is modeled by seven 1^{st} order elements. In both models, each port contains one first order 2-D element. Numerical parameters are: $N_u=N_v=6$ and $NGL_u=NGL_v=20$. The 3-D numerical parameters were kept equal to the FEM analysis in [62]. *S*-parameter results were compared in Figs. 2.5 and 2.7 and excellent agreement is achieved.

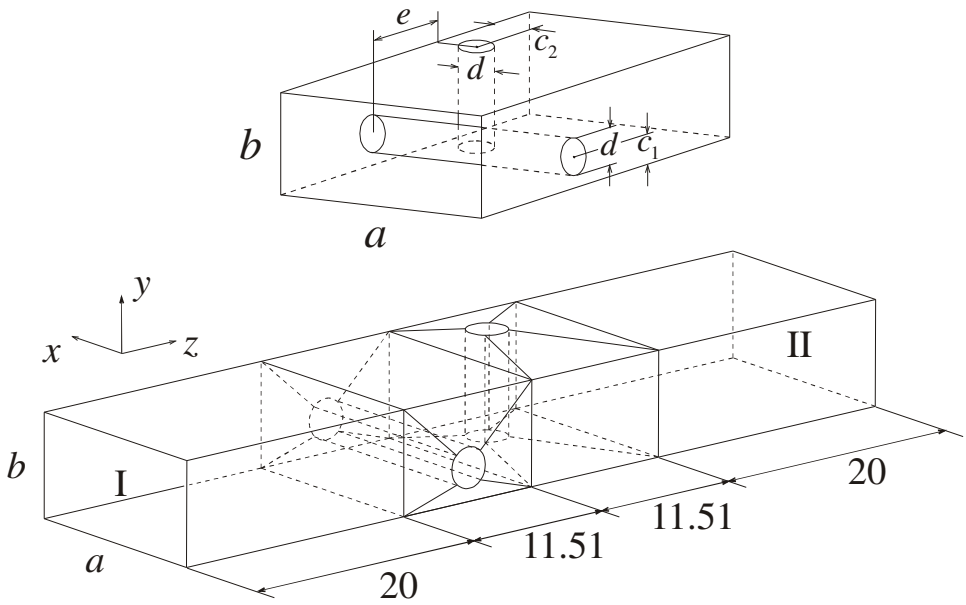

Fig. 2.4. Two crossed posts in a WR-62 waveguide (a = 15.7988 mm, b = 7.8994 mm, c_1 = 2.5 mm, c_2 = 4 mm, d = 3 mm, and e = 11.51 mm).

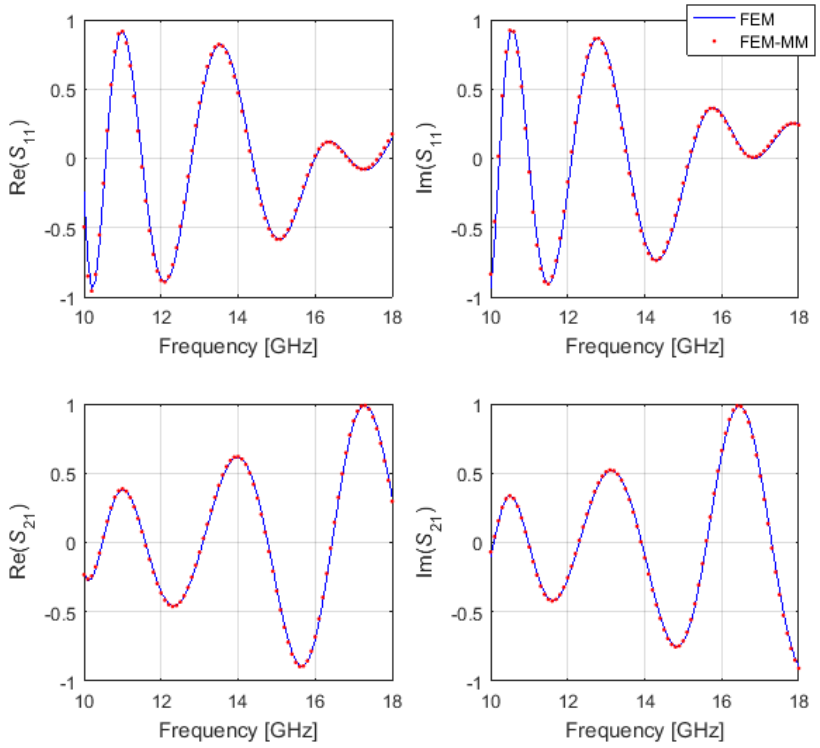

Fig. 2.5. Comparison of S-parameters for the dominant mode analysis of the model in Fig. 2.4 obtained by FEM and FEM-MM.

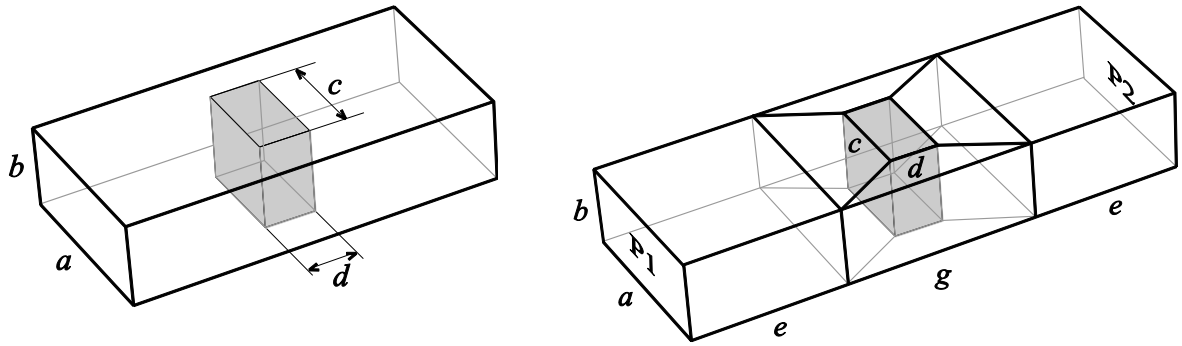

a) b)

Fig. 2.6. Dielectric ($\varepsilon_r = 8.2$) post discontinuity in a WR-90 waveguide: (a) definition of the structure geometry ($a = 22.86$ mm , $b = 10.16$ mm , $c = 12$ mm , and $d = 6$ mm) and (b) first order large-domain volumetric mesh of the structure using generalized hexahedra ($e = 45.72$ mm and $g = 24$ mm).

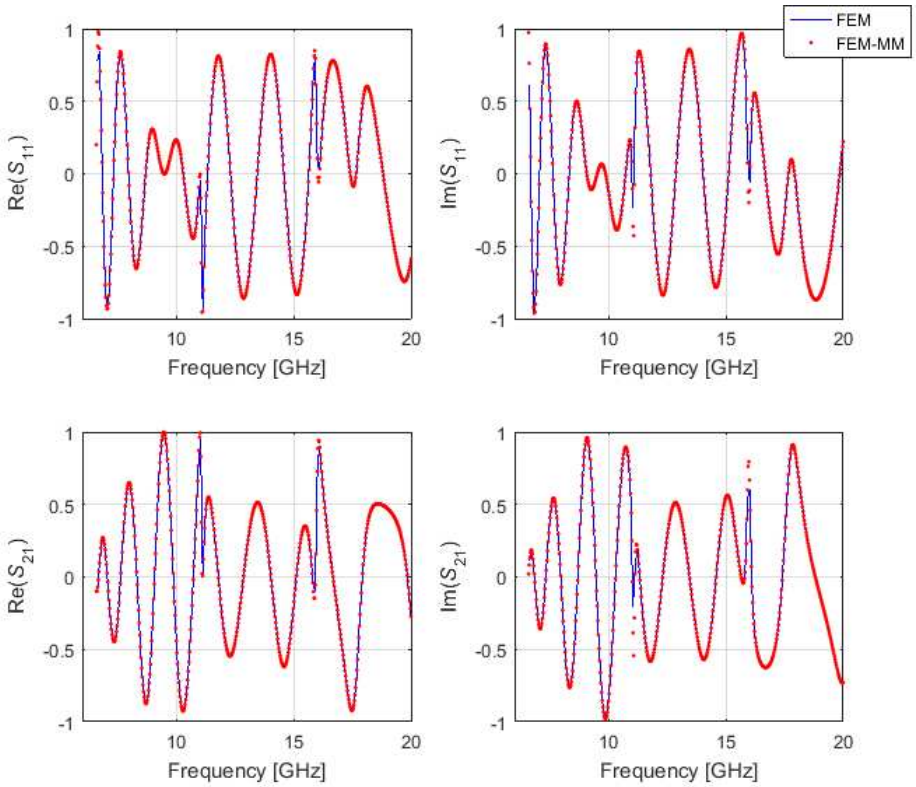

Fig. 2.7. Comparison of *S*-parameters for the dominant mode analysis of the model in Fig. 2.6 obtained by FEM and FEM-MM.

2.4.3 Short WR-90 with cylindrical metallic post

The dominant mode regime analysis of the waveguides containing an embedded structure close to the port needs to take into account higher modes in the port boundary condition due to

generation of the evanescent modes. Short waveguide structure in Fig. 2.8 is described by geometrical parameters: $l = 4\,\text{mm}$, $a = 22.86\,\text{mm}$ and $b = 10.16\,\text{mm}$, with cylindrical post of radius $r = 1\,\text{mm}$ in the middle of the structure. Due to specific geometry of the structure, just TE_{m0} modes, for odd values of *m*, are needed for the correct boundary condition analysis when the structure is excited by the dominant mode. *h*- and *p*- refinement analysis along *x* and *z* directions is done, while the parameters along *y* axis are kept constant, and the results are presented. For the comparison purpose, results are obtained in ANSYS HFSS [106] for the same waveguide but of the length $l = 10\,\text{mm}$, so all evanescent modes at the port boundary have dissipated. HFSS basis functions that are used in analysis are of the 2nd order.

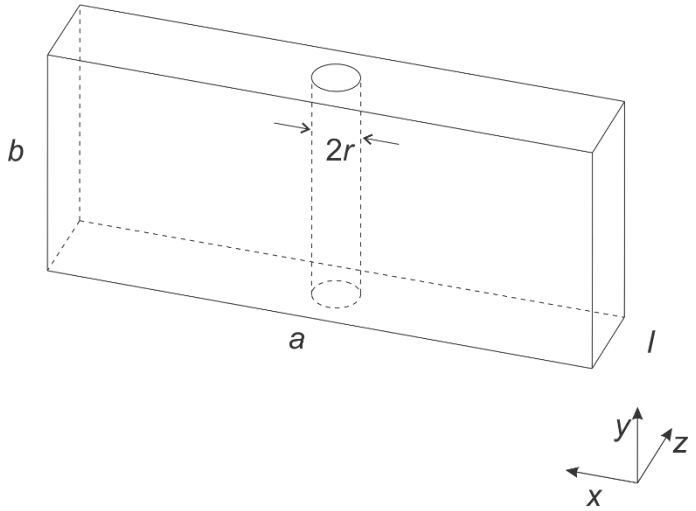

Fig. 2.8. Short WR90 waveguide with cylindrical metallic post.

Fig. 2.9 shows four element model of the second geometrical order in the a) part and with the orders of the polynomial approximation in the b) part. The model is constructed such that *u*, *v* and *w* local coordinates are *x*, *y* and *z* directed at the edges of the model, respectively. Each port is modeled by one 2-D element. Modes are obtained from 2-D FEM analysis for N_u=10, N_v=1, while 3-D FEM results are computed for $N_u = N_v = N$ and N_v=1, where *N* varies between 2 and 10. Number of Gauss-Legendre points used in the integration process is computed as $NGL_{u/v/w} = N_{u/v/w} + 4$. Scattering parameters and absolute error compared to the HFSS results given in Fig. 2.10 are

computed taking into account TE_{10}, TE_{30}, TE_{50} and TE_{70} modes when evaluating GSM matrix. Accuracy increases with higher order basis functions and the absolute error increases at higher frequencies which can be expected having in mind that wavelength in the waveguide decreases. The absolute error averaged over frequency taking into account one, two, three or four modes is given in Fig. 2.11. Note that the averaged error decreases with increasing *N* when higher modes are taken into account.

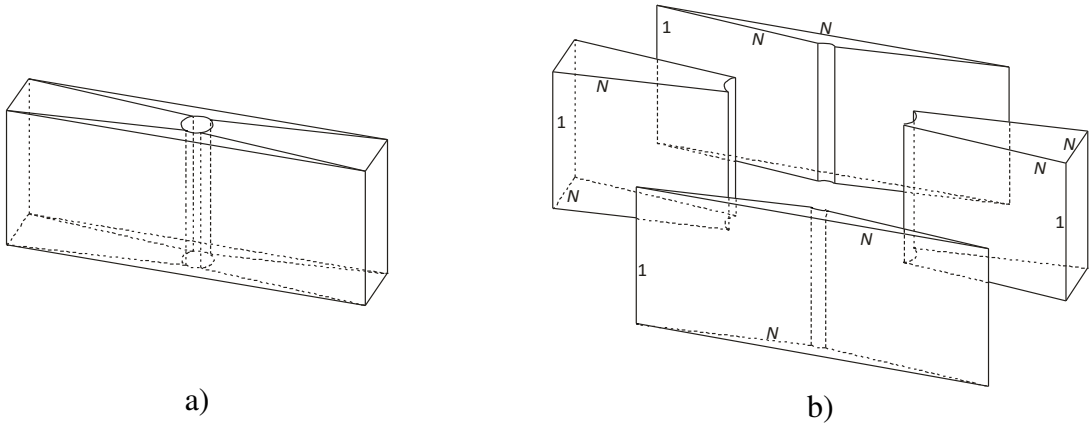

a) b)

Fig. 2.9. Large-domain meshing (a) 2nd geometrical order model with four elements around the post. (b) Orders of the polynomial field approximation.

Fig. 2.12 shows (a) six element model of the second geometrical order and (b) the orders of the polynomial approximation. The model is constructed such that *u*, *v* and *w* local coordinates are *x*, *y* and *z* directed at the straight edges of the elements, respectively. Each port is modeled by three 2-D element. Modes and results are obtained for the same basis function order values per element as for the previous model, Fig. 2.9. Scattering results and error analysis are shown in Figs. 2.13-2.14. The error averaged over frequency decreases with increasing *N* when taking higher modes into account, and higher accuracy than in the previous model for the same number of unknowns is observed.

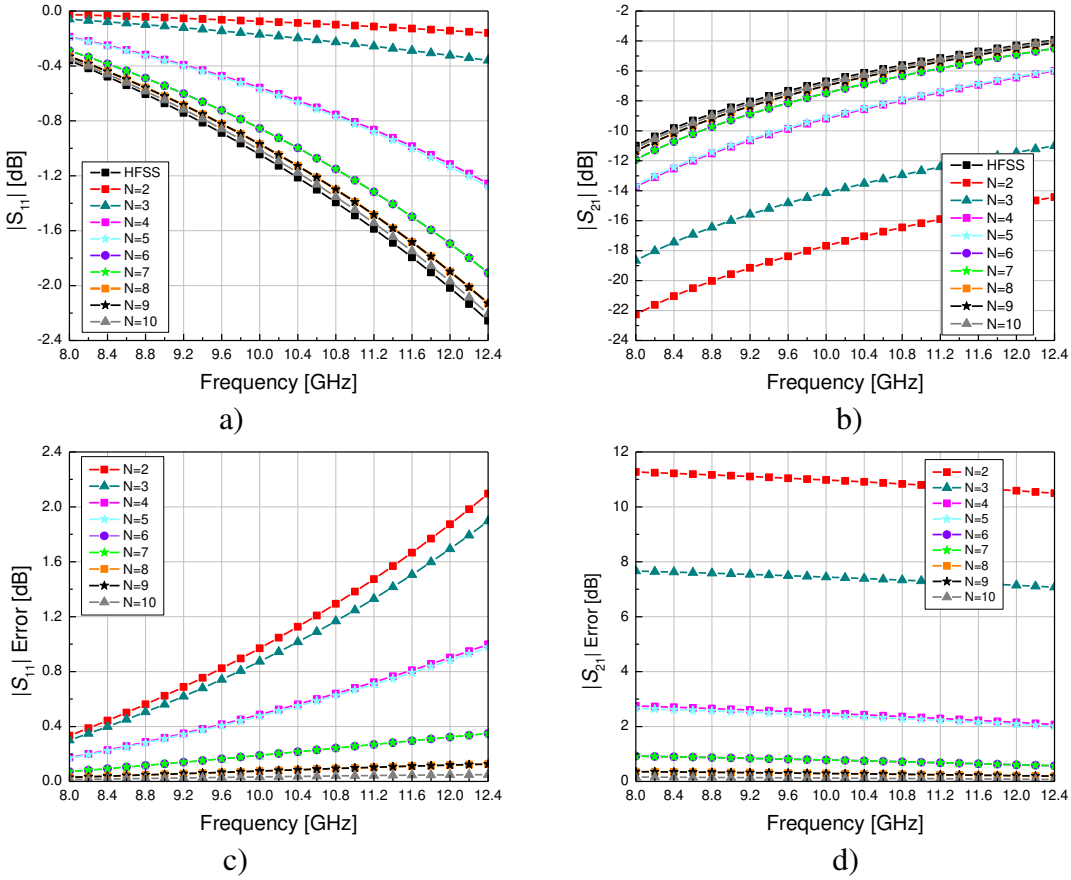

Fig. 2.10. Scattering parameters as a function of frequency computed for different values of *N* for the waveguide model in Fig. 2.9. (a) Reflection coefficient in dB, (b) Transmission coefficient in dB, (c) Absolute $|S_{11}|$error in dB, (d) Absolute $|S_{21}|$ error in dB.

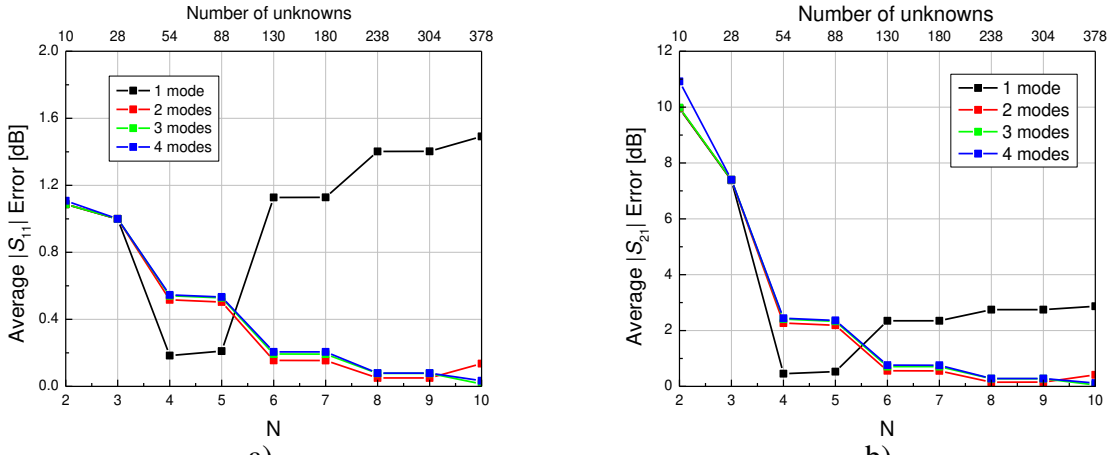

Fig. 2.11. Error in dB averaged over frequency range from 8 to 12.4 GHz computed for (a) Reflection coefficient, (b) Transmission coefficient for the structure in Fig. 2.9.

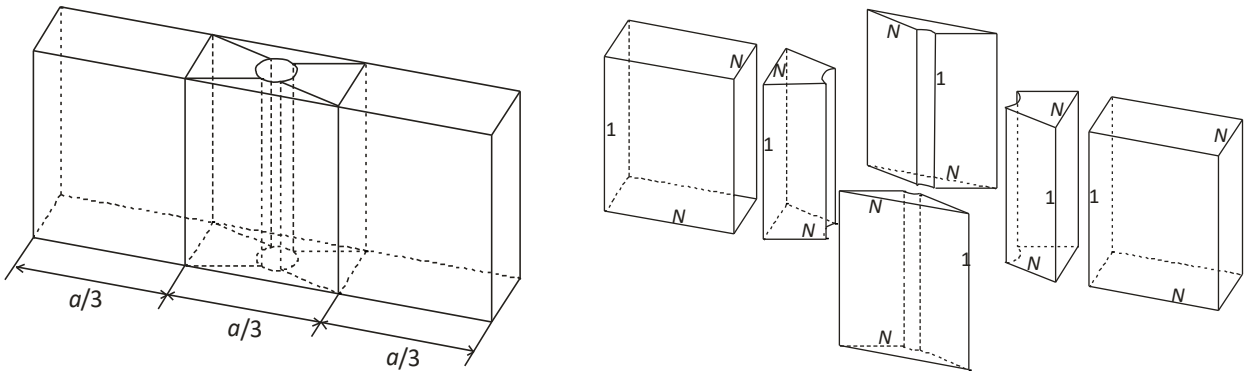

a) b)

Fig. 2.12. Large-domain meshing (a) 2nd geometrical order model with four elements around the post and two added on the side. (b) Orders of the polynomial field approximation.

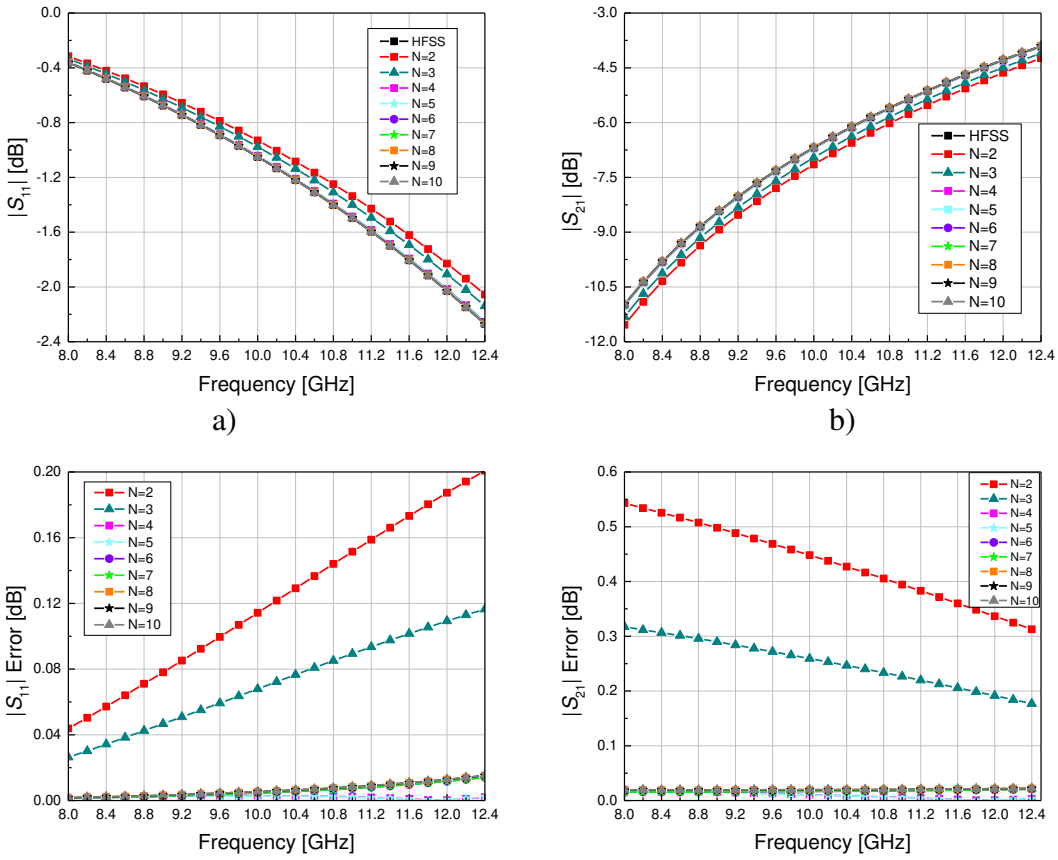

a) b)

c) d)

Fig. 2. 13. Scattering parameters as a function of frequency computed for different values of *N* for the waveguide model in Fig. 2.12. (a) Reflection coefficient in dB, (b) Transmission coefficient in dB, (c) Absolute $|S_{11}|$error in dB, (d) Absolute $|S_{21}|$ error in dB.

Figs. 2.15 and 2.17 show second geometrical order models with 16 and 36 elements, with ports being modeled by six and ten 2-D elements, respectively. Modes and results are obtained for

the same numerical integration parameter and basis order values per element as in for the model from Fig. 2.9. Error analysis is shown in Figs. 2.16 and 2.18 for the two models in Figs. 2.15 and 2.17, error decreasing with higher values of *N*, when taking higher modes into account.

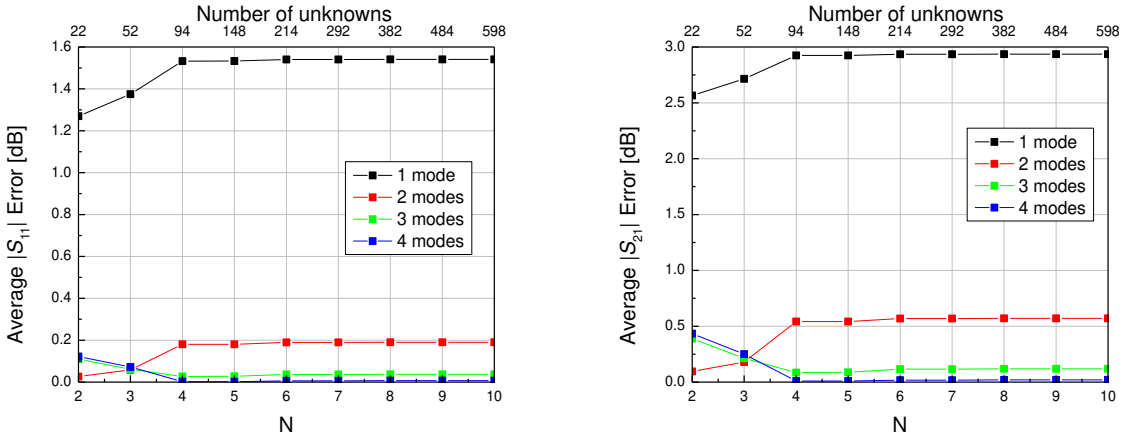

Fig. 2.14. Error in dB averaged over frequency range from 8 to 12.4 GHz computed for (a) Reflection coefficient, (b) Transmission coefficient for the structure in Fig. 2.12.

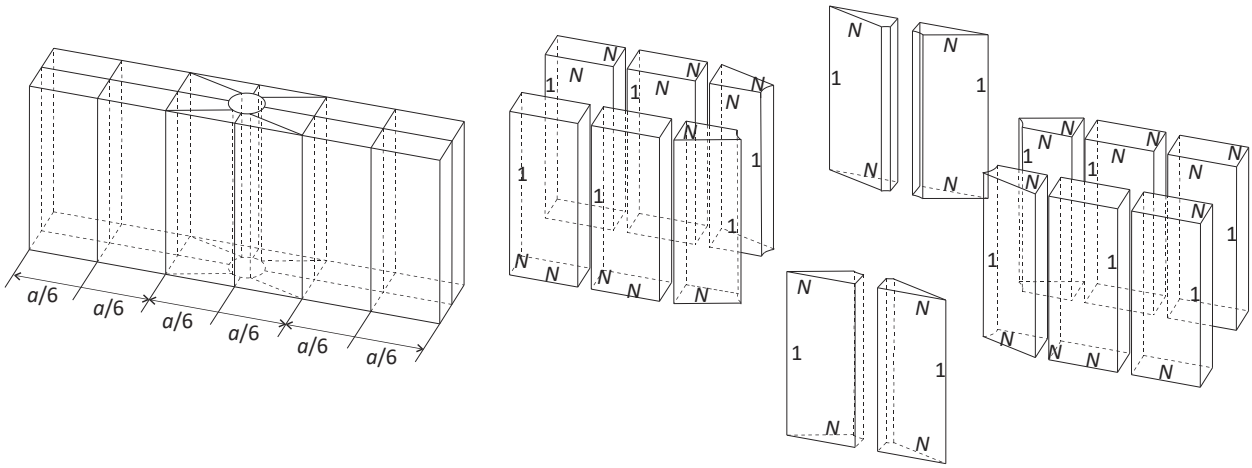

Fig. 2.15. 2nd geometrical order model with eight elements around the post and eight added on the side with orders of the polynomial field approximation.

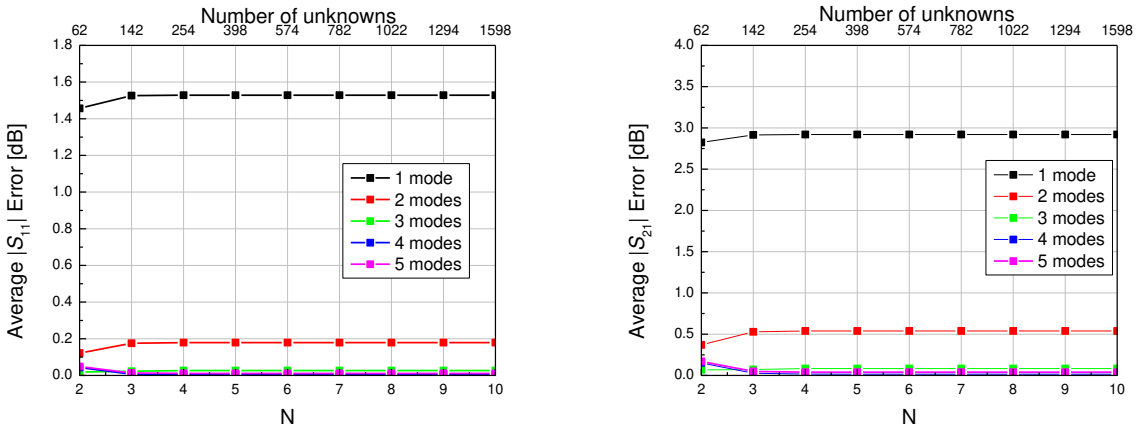

a) b)

Fig. 2.16. Error in dB averaged over frequency range from 8 to 12.4 GHz computed for (a) Reflection coefficient, (b) Transmission coefficient for the structure in Fig. 2.15.

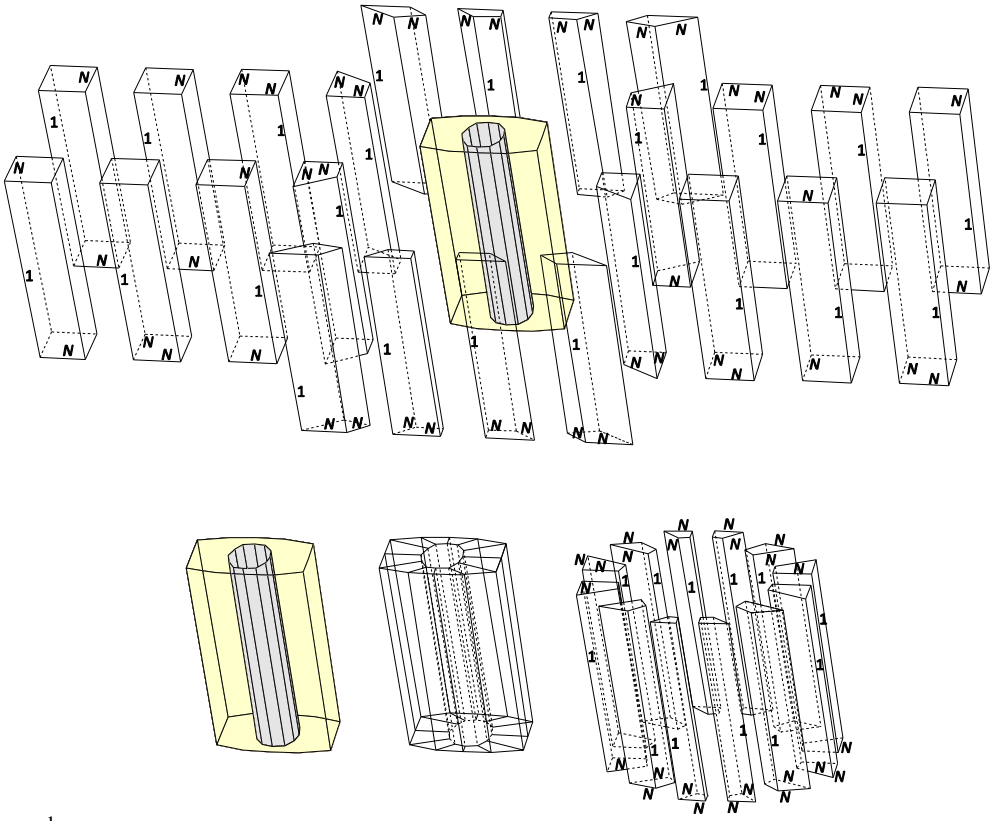

Fig. 2.17. 2nd geometrical order model with 36 elements with orders of the polynomial field approximation.

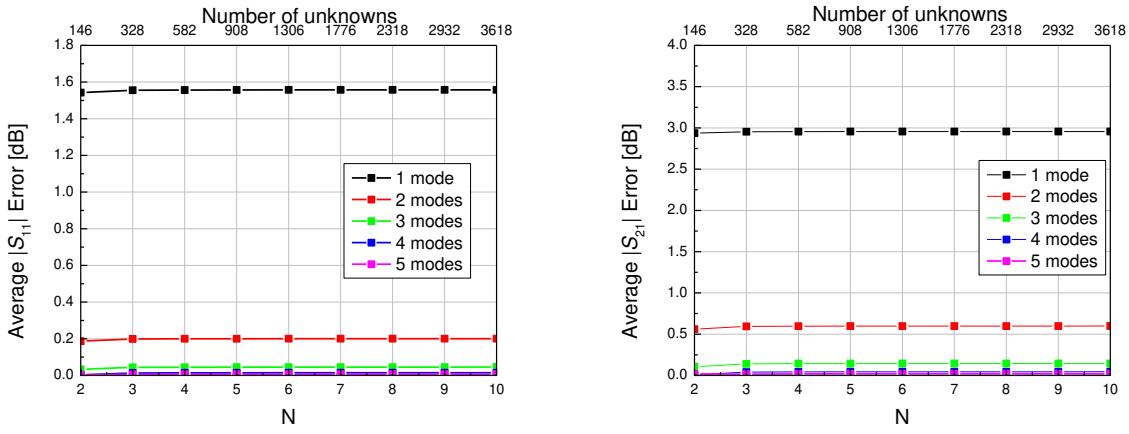

a) b)

Fig. 2.18. Error in dB averaged over frequency range from 8 to 12.4 GHz computed for (a) Reflection coefficient, (b) Transmission coefficient for the structure in Fig. 2.17.

From the analysis presented, it is noted that higher modes need to be considered in order to accurately model short waveguides containing an embedded structures in the vicinity of the port. The geometry of waveguide structure with cylindrical post in Fig. 2.8 and different model discretization provided in Figs. 2.9, 2.12, 2.15 and 2.17 and corresponding results show that *h*-refined around the metallic post brings improvement of accuracy but that large domain elements and *p*-refinement are better choice. For the best error - number of unknown balance, the large domain model with refinement around the post in Fig. 2.12 is the choice showing excellent error averaged over frequency for 94 unknowns.

2.5 Numerical Results for 3-D waveguides enclosed by SIBC

2.5.1 Long 3-D rectangular waveguide model excited by TE_{10} mode

Consider an air filled rectangular waveguide in Fig. 2.3(b) with $a = 4$ m, $b = 3$ m and overall length 1000m. Smooth wall parameters are $\sigma_w = 0.01$ S/m, $\varepsilon_{rw} = 5$ and operating frequency is 1 GHz. Port 1 is excited by TE_{10} mode with the peak value of 1V/m. The long waveguide is modeled in two sections (subsystems). The first section of the length l includes port 1, and it is short and modeled by means of FEM-MM-GSM with N_m modes approximating field at the port 2. The

electromagnetic behavior of the second section, which includes the rest of the waveguide, is modeled by the means of 2-D FEM where electric field in the plane at $z'+l$ away from the port 1, i.e. z' away from the end of the first section (port 2), is assumed to be superposition of propagating modes:

$$\mathbf{E}(x, y, z'+l) = \sum_{m=1}^{N_m} C_m \mathbf{e}_m (x, y) e^{-\gamma_m z'}, \tag{2.10}$$

where C_m is the magnitude of the m^{th} mode existing at port 2 and is computed from GSM-FEM-MM simulation of the first section. This approximation assumes reflection coefficients in the second subsystem are zero.

Port 1 is modeled by 48 first order square elements - every element is 0.25 m^2. The 3-D structure of the first section is then constructed with elements conforming to the 2-D elements of the waveguide port and are 0.25 m long along z-axis. First half of the meter of the subsection is enclosed by PEC walls in order to generate TE_{10} waveguide mode excitation at port 1. The walls of the rest of the waveguide are enclosed by the material with finite conductivity. Model 1 is 1 m long, having 192 3-D elements. Basis function orders per element are $N_u = N_v = N_w = 3$, $NGL_u = NGL_v = NGL_w = 8$, giving overall number of 3-D unknowns to be 16386. Model 2 is 1.5 m long, having 288 3-D elements. Basis function orders per element are the same as for model 1 giving overall number of 3-D unknowns to be 24672.

Fig. 2.19 shows results at the center of the waveguide as a function of the distance (d) from the excited port. For the verification purposes of the method including SIBC, waveguide with finite conductivity walls is analyzed by means of Vector Parabolic Equation (VPE) method[1] which discretizes the whole length of the waveguide, unlike FEM-MM-GSM. The y component of the electric field vector is compared for two models and different number of modes (N_m)

[1] VPE results are provided by Dr. Slobodan Savić, collaborator from University of Belgrade, Belgrade, Serbia

approximating field at port 2. It can be noted that for the shorter model, boundary condition at port 2 needs to include higher number of modes (cyan line in Fig. 2.19) in order to compare accurately with the reference VPE result. On the other hand, for the longer model, lower number of modes at the port 2 approximates well the field at boundary. This can be explained by attenuation of higher modes in the extra length in model 2.

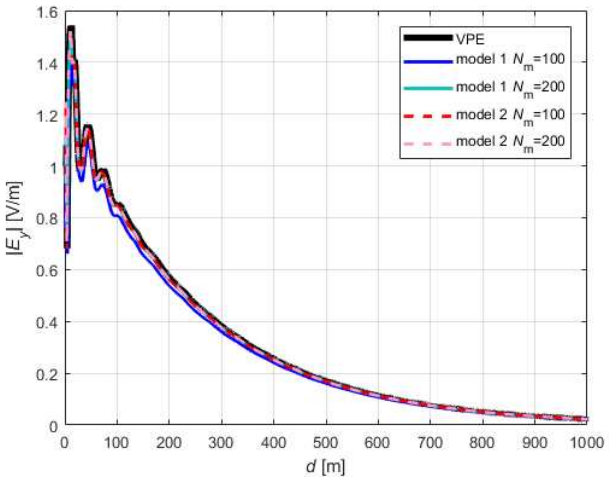

Fig. 2.19. Electric field at the center of the waveguide cross-section as a function of the distance from the excited port.

2.5.2 Communication system in Massif Central tunnel

Modeling of electromagnetic field in tunnels has been in high-demand for decades, especially with underground transportation development and improvement of mining environment. Measurement operations in tunnels, which are commonly employed [150],[151],[155][156], are cumbersome and simulation assisted communication design is highly appreciated. In tunnel modeling, Vector Parabolic Equation (VPE) [158]-[159], Ray tracing (RT) [161]-[163] and hybrid [164]-[166] methods have been popularly employed. VPE methods are very efficient in analyzing long straight sections of the tunnel, but approximate arched structures with rectangular cross-section. RT method, which is not employing full wave analysis, is excellent in providing signal attenuation characteristics of complex structures, but computational time

depends on number of reflections on the ray path, which is increasing with length of the tunnel. Hybrid methods seem to take advantage of both of these methods, but rectangular approximation of the arched cross-section has been mainly used, providing accurate power estimation just in the central area [159]. This can be a satisfactory trade-off especially when the optimization for the communication placement needs to be performed, but very few papers report on the results for antenna placed in the vicinity of the tunnel boundary [160]. It has been well known that tunnels can be modeled as waveguides with lossy dielectric walls [154],[151],[168], but mainly rectangular and circular cross-sections have been used giving limited accuracy representations [157]. We are exploring the benefits of higher order waveguide modeling to accurately model geometry of the arched tunnel cross-section and precisely estimate field variation even close to the wall.

Vertically polarized transmitting and receiving antenna are positioned inside the Massif Central tunnel at distance $2l+z$ from each other [151], at x_A and y_A away from the center and bottom of the tunnel, respectively. The tunnel walls are represented via SIBC with σ_w=0.01 S/m and ε_{rw}=5 [150],[151], and the curved geometry of the tunnel is modeled with 2nd order geometrical elements. Corrugation coefficient is chosen to be C_{CW}=0.83, in order to obtain correct attenuation and pseudo periodicity in the tunnel, having in mind results in Fig 1.9. The tunnel is modeled in 3 sections (subsystems).

The first and third sections, in Fig. 2.20, containing transmitting and receiving antenna respectively, are geometrically the same and are modeled by the means of FEM-MM-GSM. The computational domain of the section is truncated by tunnel walls modeled via SIBC (in light pink in Fig. 2.20), waveguide port and absorbing boundary situated on opposite sides of the antenna along z axis. Port is colored in light blue, absorbing boundary in blue and antenna is depicted in

black. In the section containing transmitting antenna, the port is placed towards the receiving antenna and it is at distance l away from the transmitting antenna, while the absorbing boundary is placed away from the receiving antenna at l' distance from the transmitting antenna.

The field at transmitting antenna terminal is represented by single mode while the field at the waveguide (tunnel) port truncating the domain expands N_m modes. Matrix (GSM^{PA}) relating the outgoing modes at the port and the ingoing mode of transmitting antenna is then of N_mx1 size, P standing for the first port and A for the antenna. The transpose of this matrix (GSM^{AP}) connects the mode received by the antenna with the ingoing modes of the tunnel port.

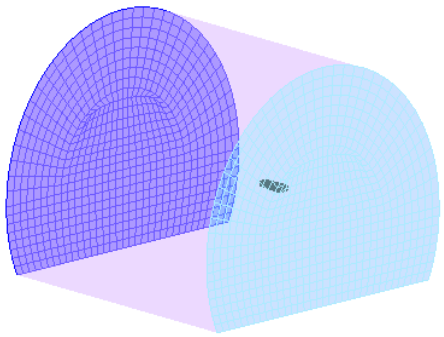

Fig. 2.20. Section of the Massif Central tunnel with antenna.

The second tunnel section, of the length z, is placed between two previously mentioned subsystems and encompassed by ports of both sections with antennas. It is modeled by the means of 2-D FEM where electric field is assumed to be superposition of propagating modes (2.10). The part of GSM connecting ingoing and outgoing modes at two ports at the ends of this section is diagonal with $GSM^{2D}(m,m) = e^{-\gamma_m z}$.

The GSM representing the whole system is computed by formulas for the cascaded subsystems as in [152], and it is 2x2 square matrix, representing the communication link between transmitting and receiving antenna. The received power is then defined as the function of distance between two antennas (z+2l):

$$P_{\mathrm{R}}(x, y, z+2l) = \left| GSM^{\mathrm{sys}}(2,1) \right|^2 P_{\mathrm{T}}, \tag{2.11}$$

where P_{T} is the input power of the transmitting antenna and the part of the system GSM needed for the computation is defined as:

$$GSM^{\mathrm{sys}}(2,1) = \left[GSM^{\mathrm{AP}} \right] \left[GSM^{\mathrm{2D}} \right] [U] \left[GSM^{\mathrm{PA}} \right], \tag{2.12}$$

where $[U] = \left([I] - \left[GSM^{\mathrm{PP}} \right] \left[GSM^{\mathrm{2D}} \right] \left[GSM^{\mathrm{PP}} \right] \left[GSM^{\mathrm{2D}} \right] \right)^{-1}$, I is diagonal unit matrix and GSM^{PP} represents the correlation between outgoing and ingoing modes of the tunnel port 1 in the section in Fig. 2.20.

GSM results of the whole system are compared to measurements [151] with the antennas excited by 34 dBm and the received power measured in dBm. Two dipole antennas are utilized for measurements at 450 MHz frequency, while horn antennas with 7dBi gain are used at 900 MHz operating frequency. Both transmitting and receiving antennas are placed 2 m away horizontally from the center and 2 m away vertically from the lowest points of the tunnel [150],[151].

For the FEM-MM-GSM models at operating frequency of 900 MHz, $x_{\mathrm{A}} = 2$ m and $y_{\mathrm{A}} = 2$ m. The horn antenna is designed to have 7 dBi gain and it is 0.41 m long with 240 mm x 120 mm waveguide feed which is excited by the dominant mode. The antenna is modeled by means of perfect electric boundaries and the space around it is finely discretized. The models are enclosed by Absorbing Boundary at $l' = 1.58$ m away from the antenna, while the port is located at the opposite side at the same distance, 57895 3-D elements discretized the subsystem and $N_u = N_v = N_w = N = 1$.

For the FEM-MM-GSM model at operating frequency of 450 MHz, $N_{\mathrm{m}} = 100$, $x_{\mathrm{A}} = 1.95$ m and $y_{\mathrm{A}} = 2$ m. Absorbing boundary (ABC) in Fig 2.20 is exchanged to another tunnel (waveguide) port. The dipole wires are modeled by means of perfect electric boundaries, the space around it is

finely discretized and the dipole is excited by ingoing TEM wave across the terminal. Distance of the ports to the antenna is $l = l' = 0.54$ m and 11922 3-D elements discretized the subsystem and $N_u = N_v = N_w = N = 1$. The coarser model is obtained by 202 2-D elements at port at $l = 0.66$ m distance from the antenna and ABC behind the antenna at the same distance. The 3-D structure is modeled by 2390 second order elements and basis functions parameters $N_u = N_v = N_w = N = 2$ and number of 3-D unknowns is 60756. The model is labeled as MC in the Fig. 2.21.

It is observed in Fig. 2.21 that, for higher frequency, with increase of number of modes at the boundary from 100 to 300, results correspond better to the measurements, as expected. For the lower frequency, 100 modes model achieves excellent comparison with measurements. For the results labeled $N_{2D} = 2$, the field at port is expanded $N_u = N_v = 2$ order of the basis functions, further confirming the results precision.

Relative received power in dB [150] has different signal level from measurements in dBm in [151], which authors in [150] explain is due to insertion loss of the antennas. We account for the difference when presenting our results. Results in Fig. 2.21 are computed using formula in (2.11), with insertion loss included, which is evaluated to decrease received power by 13 dB.

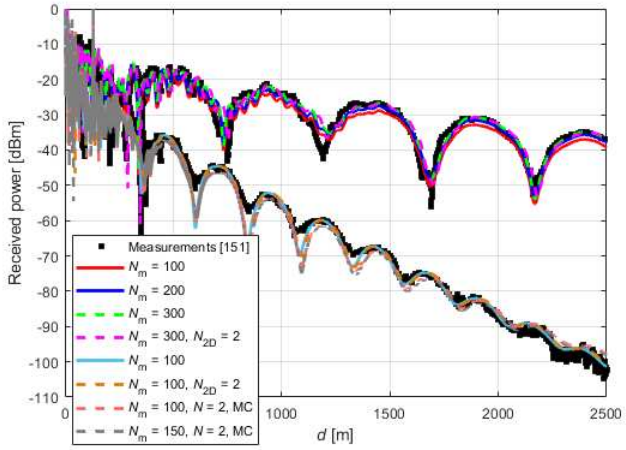

Fig. 2.21. Received Power as a function of distance between transmitting and receiving antenna.

Variation of y component of the electric field vector over the tunnel cross-section, computed as sum of the modes, is shown in Fig. 2.22 at the 450 MHz operating frequency. The two cross-section are at 0.54 m and 500 m away from the transmitting antenna and the dipole is excited by ingoing TEM wave with 1.29 V across the terminal.

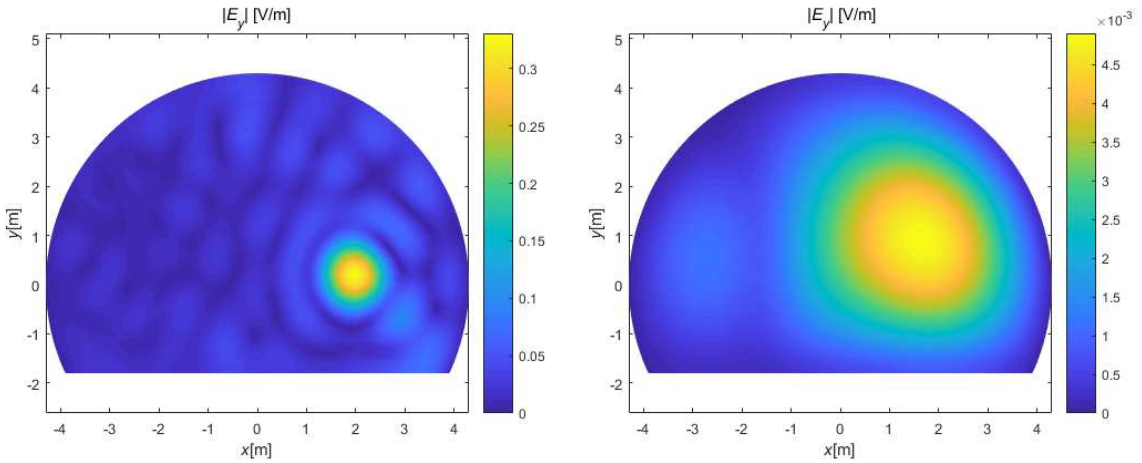

a) b)

Fig. 2.22. Field pattern at a) 0.54 m and b) 500 m away from the antenna.

Relative received power measured in dB in Fig. 2.23 are computed using formula in (2.11) and port refinement as in Fig. 2.20. They are compared with measurements for both horizontally (HH) and vertically (VV) positioned transmitting and receiving dipole antennas [150], showing excellent agreement for both amplitude variation and pseudo periodicity, unlike commonly used equivalent rectangular model of the tunnel. The results for vertical polarization are shifted by 52 dB to match the power representation in the figure. Operating frequency is 510 MHz, $N_{\mathrm{m}} = 150$, $y_{\mathrm{A}} = 2$ m and antenna is horizontally situated 1.2 m away from the wall of the tunnel, i.e. $x_{\mathrm{A}} = 3.1$ m. 3-D FEM model of the subsystem with antenna is similar to the one in Fig. 2.20. Distance of the port to the antenna is $l = 0.48$ m and absorbing boundary is placed at the same distance on the other side of the antenna. The subsystem is discretized by 7590 3-D elements. Order of the basis functions per element is $N_u = N_v = N_w = N = 1$ and number of 3-D unknowns is 25096.

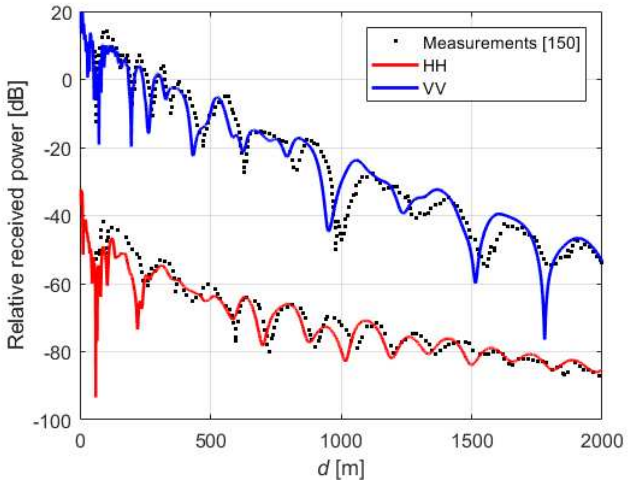

Fig. 2.23. Relative received power for the antenna situated in the vicinity of the wall.

2.6 Conclusion

Double Higher Order FEM-MM computation of GSM is developed using modal forms and propagation coefficient from eigenvalue solution of 2-D FEM analysis in Chapter 1. The method is verified with one mode large domain model analysis and compared to purely FEM waveguide analysis for dominant mode excitation. *p*- and *h*- refinement analysis is operated on short W-90 with cylindrical post by multi-mode GSM computation showing the benefits of large domain discretization and multimode boundary condition at the ports truncating the domain of computation. SIBC is implemented and methodology is verified by comparing results of the rectangular waveguide model with lossy dielectric walls to Vector Parabolic Equation method. Massif Central tunnel with the geometry accurately presented by second geometrical order elements is analyzed by means of DHO FEM-GSM-MM with SIBC modeling the tunnel walls. Communication system in Massif Central tunnel is simulated at operating frequencies of 450, 510 and 900 MHz and excellent agreement with measurements is achieved when using large number of modes for field expansion, even near the wall of the tunnel.

3 EXTRACTION METHOD FOR NEAR-FIELD SINGULAR AND HYPERSINGULAR INTEGRALS FOR THE DOUBLE HIGHER ORDER SURFACE INTEGRAL EQUATION METHOD OF MOMENTS

3.1 Introduction

Precise and computationally efficient matrix entry determination for the method of moments (MoM), applied to the surface integral equation (SIE) formulation in the frequency domain, highly depends on the evaluation of the integrals defined on the surface elements, which is especially complicated for near-singular integrals, i.e. for the elements in close proximity. The techniques improving the integral precision for small distances between testing and basis elements in the MoM matrix entries computation are mainly categorized into singularity extraction (i.e. subtraction methods) [40],[42] and singularity cancellation (i.e. coordinate transformation methods) [43]-[44]. The benefits of treating source and testing integrals simultaneously (so called 4-D integral) have been reported [46],[47] and are proving to be the best choice for specific mutual spatial position of elements. This chapter is about novel extraction integration technique that mitigates 2-D singularity on the basis patch and can be utilized on testing and basis elements in no specific mutual spatial position, also taking into account higher order basis function approximating equivalent currents defined over higher order elements which adds complexity to the problem [42]. In general, MoM-SIE method solves electromagnetic response of the structures with both metallic and dielectric/magnetic features. This increases the singularity of the integrated function so the method needs to alleviate both types of singularities.

This chapter is organized as follows. Section 3.2 gives an overview of the Double Higher Order (DHO) Surface Integral Equation (SIE) Method of Moments (SIE). Section 3.3 gives overview of novel singularity extraction technique [42], with the introduction to the method

correction for the low precision cases, which is the main topic of the work presented. In Section 3.4 numerical results and discussion are provided, followed by the summary in Section 3.5.

3.2 Double Higher Order Surface Integral Equation Method of Moments

3.2.1 Surface Integral Equation Formulation

Let the arbitrary electromagnetic structure be excited by a time-harmonic electromagnetic field of $\mathbf{E}_i$ and $\mathbf{H}_i$ electric and magnetic field intensities of angular frequency ω. Based on surface equivalence principle [1], [2] this structure can be broken into subsystems, where each represents a homogeneous dielectric region or a domain. While the medium homogeneity of each domain is a requirement, there can be metallic surfaces contained within each medium. The electric and magnetic fields, **E** and **H**, scattered from the dielectric discontinuities in each domain, can be represented as the radiation by the equivalent surface electric $\mathbf{J}_S$ and magnetic $\mathbf{M}_S$ currents placed on the boundary of the domain. Only the electric currents ($\mathbf{J}_S$) are required for metallic surface representation.

The tangential components of electric and magnetic fields at the boundary surface between two dielectric domains yield

$$[\mathbf{E}(\mathbf{J}_S,\mathbf{M}_S,\varepsilon_1,\mu_1)]_{tang}+(\mathbf{E}_i)_{tang}=[\mathbf{E}(-\mathbf{J}_S,-\mathbf{M}_S,\varepsilon_2,\mu_2)]_{tang}, \tag{3.1}$$

$$[\mathbf{H}(\mathbf{J}_S,\mathbf{M}_S,\varepsilon_1,\mu_1)]_{tang}+(\mathbf{H}_i)_{tang}=[\mathbf{H}(-\mathbf{J}_S,-\mathbf{M}_S,\varepsilon_2,\mu_2)]_{tang}, \tag{3.2}$$

where ε_1, μ_1 and ε_2, μ_2 are complex permittivity and permeability of domains 1 and 2. Equations (3.1)-(3.2) represent the boundary conditions for the electric and magnetic fields and assume excitations to be present only in domain 1. At the surface of the conducting bodies, the above mentioned boundary conditions reduce to

$$[\mathbf{E}(\mathbf{J}_S,\mathbf{M}_S,\varepsilon_1,\mu_1)]_{tang}+(\mathbf{E}_i)_{tang}=0. \tag{3.3}$$

The electric and magnetic fields radiated by the equivalent electric and magnetic currents in the domain with complex permittivity ε and complex permeability μ are calculated as follows:

$$\mathbf{E} = \mathbf{E}_{\mathrm{J}}(\mathbf{J}_S) + \mathbf{E}_{\mathrm{M}}(\mathbf{M}_S), \tag{3.4}$$

$$\mathbf{E}_{\mathrm{J}}(\mathbf{J}_S) = -\mathrm{j}\omega\mathbf{A} - \nabla\Phi, \tag{3.5}$$

$$\mathbf{E}_{\mathrm{M}}(\mathbf{M}_S) = -\varepsilon^{-1}\nabla\times\mathbf{F}, \tag{3.6}$$

$$\mathbf{H} = \mathbf{H}_{\mathrm{M}}(\mathbf{M}_S) + \mathbf{H}_{\mathrm{J}}(\mathbf{J}_S), \tag{3.7}$$

$$\mathbf{H}_{\mathrm{M}}(\mathbf{M}_S) = -\mathrm{j}\omega\mathbf{F} - \nabla U, \tag{3.8}$$

$$\mathbf{H}_{\mathrm{J}}(\mathbf{J}_S) = \mu^{-1}\nabla\times\mathbf{A}. \tag{3.9}$$

In the above expressions, **A, F,** Φ and *U* are the magnetic and electric scalar and vector potentials, which are computed as

$$\mathbf{A} = \mu\int_S \mathbf{J}_{\mathrm{S}} g \mathrm{d}S, \tag{3.10}$$

$$\mathbf{F} = \varepsilon\int_S \mathbf{M}_{\mathrm{S}} g \mathrm{d}S, \tag{3.11}$$

$$\Phi = \mathrm{j}\omega^{-1}\varepsilon^{-1}\int_S \nabla_{\mathrm{S}}\cdot\mathbf{J}_{\mathrm{S}} g \mathrm{d}S, \tag{3.12}$$

$$U = \mathrm{j}\omega^{-1}\mu^{-1}\int_S \nabla_{\mathrm{S}}\cdot\mathbf{M}_{\mathrm{S}} g \mathrm{d}S, \tag{3.13}$$

where integration is performed over the boundary surface of the domain *S*, with *g* being the homogeneous medium Green's function

$$g = \frac{\mathrm{e}^{-\gamma R}}{4\pi R}, \qquad \gamma = \mathrm{j}\omega\sqrt{\varepsilon\mu}, \tag{3.14}$$

γ the propagation coefficient and *R* the distance between field and source points.

The integral expressions for fields **E** and **H** in (3.4)-(3.13) plugged in (3.1)-(3.3) represent a set of coupled electric/magnetic field integral equations (EFIE/MFIE) with $\mathbf{J}_S$ and $\mathbf{M}_S$ as unknowns, which are numerically solved by the method of moments (MoM) [2].

3.2.2 Method of Moments Generalized Galerkin Impedances

In the method of moments equivalent electric and magnetic current densities $\mathbf{J}_S$ and $\mathbf{M}_S$, are approximated by a linear combination of the basis functions, defined on the geometrical elements which tessellate electromagnetic system geometries, where the objective is to determine the unknown coefficients of the expansion [2]. The classic approach to the compute these unknowns is to test system of equations (3.1)-(3.3) by means of the Galerkin method, where the testing functions are identical to the ones used in the current expansion [12]. This procedure results in a system of linear equations, comprising of different types of elements, corresponding to the various combination of basis and testing functions, which can be expressed as follows

$$Z_{mn}^{\mathrm{ee}} = \int_{S_m} \mathbf{J}_{Sm} \cdot \mathbf{E}_{\mathrm{J}}(\mathbf{J}_{Sn}) \mathrm{d}S_m, \tag{3.15}$$

$$Z_{mn}^{\mathrm{em}} = \int_{S_m} \mathbf{J}_{Sm} \cdot \mathbf{E}_{\mathrm{M}}(\mathbf{M}_{Sn}) \mathrm{d}S_m, \tag{3.16}$$

$$Z_{mn}^{\mathrm{me}} = \int_{S_m} \mathbf{M}_{Sm} \cdot \mathbf{H}_{\mathrm{J}}(\mathbf{J}_{Sn}) \mathrm{d}S_m, \tag{3.17}$$

$$Z_{mn}^{\mathrm{mm}} = \int_{S_m} \mathbf{M}_{Sm} \cdot \mathbf{H}_{\mathrm{M}}(\mathbf{M}_{Sn}) \mathrm{d}S_m. \tag{3.18}$$

where $\mathbf{J}_{Sm}$, $\mathbf{M}_{Sm}$, $\mathbf{J}_{Sn}$ and $\mathbf{M}_{Sn}$ are the electric and magnetic current expansion functions defined on the m^{th} and n^{th} surface elements (S_m) and (S_n). The matrix entrees defined by equations (3.15)-(3.18) are called generalized Galerkin impedances. The right hand side of the final matrix equation (generalized voltages) are determined by system excitations in the form of incident electric $\mathbf{E}_i$ and magnetic $\mathbf{H}_i$ fields, and are computed as

$$V_m^{\mathrm{e}} = \int_{S_m} \mathbf{J}_{\mathrm{S}m} \cdot \mathbf{E}_{\mathrm{i}} \mathrm{d}S_m , \tag{3.19}$$

$$V_m^{\mathrm{m}} = \int_{S_m} \mathbf{M}_{\mathrm{S}m} \cdot \mathbf{H}_{\mathrm{i}} \mathrm{d}S_m . \tag{3.20}$$

Substituting equation (3.5) into (3.15), applying the divergence theorem and expanding $\nabla_S \cdot \left(\mathbf{J}_{\mathrm{S}m} \Phi_n \right)$, results in the following expressions for electric/electric Galerkin impedances:

$$\begin{aligned} Z_{mn}^{\mathrm{ee}} &= -\mathrm{j}\omega \int_{S_m} \mathbf{J}_{\mathrm{S}m} \cdot \mathbf{A}_n \mathrm{d}S_m - \int_{S_m} \mathbf{J}_{\mathrm{S}m} \cdot \nabla_S \Phi_n \mathrm{d}S_m = \\ &= -\mathrm{j}\omega \int_{S_m} \mathbf{J}_{\mathrm{S}m} \cdot \mathbf{A}_n \mathrm{d}S_m + \int_{S_m} \Phi_n \nabla_S \cdot \mathbf{J}_{\mathrm{S}m} \mathrm{d}S_m - \oint_{c_m} \mathbf{J}_{\mathrm{S}m} \Phi_n \mathbf{n}_m \mathrm{d}l_m \end{aligned} , \tag{3.21}$$

where $\mathbf{n}_m$ is the outward facing unit vector normal to the boundary contour C_m of the surface S_m. When the divergence-conforming basis functions are used, the latter term in (3.21) is equal to zero [12]. Finally, using (3.10) the vector potential $\mathbf{A}_n$ can be expressed in terms of the corresponding electric-current basis function $\mathbf{J}_{\mathrm{S}n}$ defined over surface element (S_n), which results in the following expression

$$Z_{mn}^{\mathrm{ee}} = -\mathrm{j}\omega\, \mu \int_{S_m} \int_{S_n} \mathbf{J}_{\mathrm{S}m} \cdot \mathbf{J}_{\mathrm{S}n} g \mathrm{d}S_n \mathrm{d}S_m + \mathrm{j}\omega^{-1} \varepsilon^{-1} \int_{S_m} \int_{S_n} (\nabla_S \cdot \mathbf{J}_{\mathrm{S}m})(\nabla_S \cdot \mathbf{J}_{\mathrm{S}n}) g \mathrm{d}S_n \mathrm{d}S_m . \tag{3.22}$$

Similarly, using vector calculus identity for $\nabla \times \left(\mathbf{M}_n g \right)$ and scalar triple product manipulations, (3.6), (3.11) and (3.16) is transformed into mixed electric/magnetic generalized impedances

$$\begin{aligned} Z_{mn}^{\mathrm{em}} &= -\frac{1}{\varepsilon} \int_{S_m} \mathbf{J}_{\mathrm{S}m} \cdot \nabla \times \mathbf{F}_n \mathrm{d}S_m = -\int_{S_m} \int_{S_n} \mathbf{J}_{\mathrm{S}m} \cdot \nabla \times (\mathbf{M}_{\mathrm{S}n} g) \mathrm{d}S_n \mathrm{d}S_m = \\ &= -\int_{S_m} \int_{S_n} \mathbf{J}_{\mathrm{S}m} \cdot (\nabla g \times \mathbf{M}_{\mathrm{S}n}) \mathrm{d}S_n \mathrm{d}S_m = -\int_{S_m} \int_{S_n} (\mathbf{M}_{\mathrm{S}n} \times \mathbf{J}_{\mathrm{S}m}) \cdot \nabla g \mathrm{d}S_n \mathrm{d}S_m \end{aligned} . \tag{3.23}$$

Subsequently, due to the duality principle, the magnetic/electric and magnetic/magnetic Galerkin impedances in (3.17) and (3.18) are computed as

$$Z_{mn}^{\mathrm{me}} = -\int_{S_m} \int_{S_n} (\mathbf{J}_{\mathrm{S}n} \times \mathbf{M}_{\mathrm{S}m}) \cdot \nabla g \mathrm{d}S_n \mathrm{d}S_m = -Z_{mn}^{\mathrm{em}} , \tag{3.24}$$

$$Z_{mn}^{\mathrm{mm}} = -\mathrm{j}\omega\,\varepsilon \int_{S_m}\int_{S_n} \mathbf{M}_{Sm}\cdot\mathbf{M}_{Sn}\, g\,\mathrm{d}S_n\,\mathrm{d}S_m + \mathrm{j}\omega^{-1}\mu^{-1}\int_{S_m}\int_{S_n}(\nabla_S\cdot\mathbf{M}_{Sm})(\nabla_S\cdot\mathbf{M}_{Sn})\, g\,\mathrm{d}S_n\,\mathrm{d}S_m\,. \quad (3.25)$$

Therefore the electric and magnetic field integral equations (3.1)-(3.3) by means of MoM are transformed into system of linear equations that can be represented in the matrix form as follows

$$\begin{bmatrix} Z^{\mathrm{ee}} & Z^{\mathrm{me}} \\ Z^{\mathrm{em}} & Z^{\mathrm{mm}} \end{bmatrix}\begin{bmatrix} \alpha \\ \beta \end{bmatrix} = \begin{bmatrix} V^{\mathrm{e}} \\ V^{\mathrm{m}} \end{bmatrix} \quad (3.26)$$

where α and β are column matrices of the unknown coefficients of the electric and magnetic current densities expansions, Z^{ee}, Z^{me} , Z^{em} and Z^{mm} are matrices with elements computed by (3.22)-(3.25), and V^{e} and V^{m} by (3.18)-(3.19).

The general method of moment technique, however, is not restricted to the type of the geometrical subdivision blocks or particular basis functions. Therefore there are many ways to obtain system of linear equations (3.26). This work is focused on surface discretization with generalized higher-order curvilinear quadrilaterals and current densities approximated by divergence-conforming hierarchical polynomial basis functions, which is described in details in Section 3.2.3.

3.2.3 Higher-Order Geometrical Elements and Basis Functions

A generalized quadrilateral is shown in (Fig. 3.1), which is used as the tessellation unit for geometry approximation. The curvilinear quadrilateral is determined by $M = (K_u+1)(K_v+1)$ arbitrarily positioned points, with K_u and K_v (K_u, $K_v \geq 1$) being geometrical orders of the element along u- and v- parametric coordinates, mapping it into parametric square [12]. Therefore, analytically position vector of the point on the 2-D element is defined as follows

$$\mathbf{r}(u,v) = \sum_{i=1}^{M}\mathbf{r}_i\, p_i(u,v) = \sum_{k=0}^{K_u}\sum_{l=0}^{K_v}\mathbf{r}_{kl}\,u^k v^l\ ,\ -1\leq u,v\leq 1\,, \quad (3.27)$$

where $\mathbf{r}_1$, $\mathbf{r}_2$, …, $\mathbf{r}_M$ are the position vectors of the interpolation points and $p_i(u, v)$ are Lagrange-type interpolation polynomials. The parametric coordinates u_j and v_j represent the local locations of the j-th node, and $\mathbf{r}_{kl}$ are constant vector coefficients derived from $\mathbf{r}_1$, $\mathbf{r}_2$, …, $\mathbf{r}_M$.

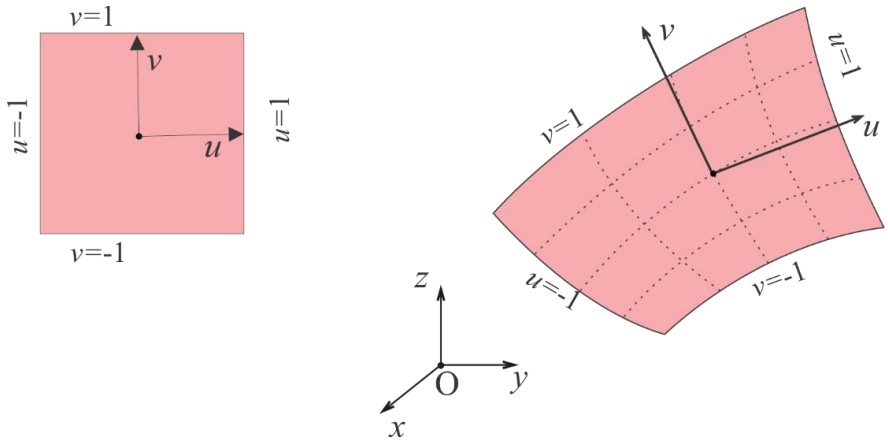

Fig. 3.1. A generalized parametric quadrilateral of geometrical orders K_u and K_v (K_u, $K_v \geq 1$).

Electric and magnetic surface current densities over every curvilinear quadrilateral are expanded as

$$\mathbf{J}_S(u,v) = \sum_{i=0}^{N_u} \sum_{j=0}^{N_v-1} \alpha_{uij}\, \mathbf{f}^{mo}_{uij}(u,v) + \sum_{i=0}^{N_u-1} \sum_{j=0}^{N_v} \alpha_{vij}\, \mathbf{f}^{mo}_{vij}(u,v), \tag{3.28}$$

$$\mathbf{M}_S(u,v) = \sum_{i=0}^{N_u} \sum_{j=0}^{N_v-1} \beta_{uij}\, \mathbf{f}^{mo}_{uij}(u,v) + \sum_{i=0}^{N_u-1} \sum_{j=0}^{N_v} \beta_{vij}\, \mathbf{f}^{mo}_{vij}(u,v), \tag{3.29}$$

where $\mathbf{f}^{mo}$ are maximally orthogonalized higher order basis functions [52] which building blocks are divergence-conforming hierarchical polynomial vector basis functions ($\mathbf{f}$) defined as

$$\begin{aligned} \mathbf{f}_{uij}(u,v) &= \frac{P_i(u)v^j}{J(u,v)}\mathbf{a}_u(u,v) \\ \mathbf{f}_{vij}(u,v) &= \frac{u^i P_j(v)}{J(u,v)}\mathbf{a}_v(u,v) \end{aligned}, \quad P_i(u) = \begin{cases} 1-u, & i=0 \\ u+1, & i=1 \\ u^i-1, & i\geq 2, \text{even} \\ u^i-u, & i\geq 3, \text{odd} \end{cases}, \quad -1\leq u,v\leq 1. \tag{3.30}$$

where N_u and N_v are the degrees of the polynomial current approximation [12]. The unitary vectors $\mathbf{a}_u$ and $\mathbf{a}_v$ in (3.30) are calculated as

$$\mathbf{a}_u(u,v)=\frac{\partial \mathbf{r}(u,v)}{\partial u}=\sum_{i=1}^{K_u}\sum_{j=0}^{K_v}\mathbf{r}_{ij}iu^{i-1}v^j \text{ and } \mathbf{a}_v(u,v)=\frac{\partial \mathbf{r}(u,v)}{\partial v}=\sum_{i=0}^{K_u}\sum_{j=1}^{K_v}\mathbf{r}_{ij}ju^{i}v^{j-1}, \tag{3.31}$$

with **r** given by equation (3.27), and $J(u,v)$ is the Jacobian of the covariant transformation,

$$J(u,v)=\left|\mathbf{a}_u(u,v)\times\mathbf{a}_v(u,v)\right|. \tag{3.32}$$

The mixed-order arrangement in (3.28) and (3.29), where the expansion orders in different directions are intentionally left uneven, equalizes the final approximation orders for surface charge densities. This has been found to be the most suitable choice for modeling of surface current densities and results in the more robust solution.

3.3 Near-Singular and Near-Hyper-Singular Integrals

Matrix elements in (3.22)-(3.25) are numerically evaluated such that outer integral over the testing surface (S_m) is evaluated by means of Gauss-Legendre numerical integration process. The inner integral over the basis surface element (S_n), popularly called two dimensional (2-D) integral, is evaluated integrating just the basis element dependent variables while the testing element is only considered by means of the Green's function (3.14) and field point (i.e. integration point of the numerically evaluated outer integral). Having in mind that double higher order 2-D surface integrals are defined on the Lagrange-type generalized curved parametric quadrilateral elements (in Fig. 3.1) and that the unknown currents, $\mathbf{J}_s$ and $\mathbf{M}_s$ in (3.28) and (3.29), are approximated by polynomial basis functions of the higher order, building blocks of the two types of singular 2-D integrals over the quadrilateral patch, have the following forms respectively

$$I_{ij}^{s}=\int_{-1}^{1}\int_{-1}^{1}u^i v^j\,\frac{e^{-\gamma R}}{4\pi R}\,\mathrm{d}u\mathrm{d}v, \tag{3.33}$$

$$I_{ij}^{hs}=\int_{-1}^{1}\int_{-1}^{1}u^i v^j\,\frac{(1+\gamma R)e^{-\gamma R}}{4\pi R^3}\,\mathrm{d}u\mathrm{d}v, \tag{3.34}$$

where i and j represent arbitrary polynomial orders of the basis functions, γ is the propagation coefficient in the medium on the either side of the element and R is the distance of the source point, $\mathbf{r}(u,v)$, from the field point, $\mathbf{r}_F$, (3.14), s labeling singular and hs hyper-singular integrals which constitute Z^{ee}/Z^{mm} and Z^{em}/Z^{me} generalized impedances, respectively. If the field point is in the proximity to the basis patch, R becomes small and kernels in (3.33) and (3.34) contain weak and strong near singularity respectively. In order to efficiently and precisely determine these integrals handling of the near-singularity is performed.

The integral enumeration technique presented here utilizes the singularity extraction method which, in general, alleviates the singularity by approximating the integrand as a function over parallelogram, in order to be computed analytically. The parallelogram is, as well as quadrilateral, defined as parametric surface in u-v domain. The difference between original function and the approximation is numerically integrated using Gauss-Legendre quadrature formulas.

Considering that $R_P(u,v)$ is the distance of the (u,v) point on the parallelogram from the field point and that variable t is defined as $t(u,v) = R^2(u,v) - R_p^2(u,v)$, the distance R can be represented as:

$$R(u,v) = R_P(u,v)\sqrt{1+t(u,v)/R_P^2(u,v)}\,. \tag{3.35}$$

The approximated singular and hypersingular integrand functions (3.33) and (3.34) defined over the parallelogram are represented through Taylor's expansion series over $t(u,v)/R_P^2(u,v)$ having in mind (3.35):

$$\frac{e^{-\gamma R}}{R} = \sum_n \frac{A_n(t)}{R_P^{2n-1}} \text{ and } (1+\gamma R)\frac{e^{-\gamma R}}{R^3} = \sum_n \frac{B_n(t)}{R_P^{2n-1}}, \tag{3.36}$$

where A_n and B_n are expansion coefficients that depend on variable t. In our implementation, the infinite expansions (3.36) are truncated such that n takes integer values from -2 to 4 and 5 for the singular and hyper singular function, respectively.

The smaller the ratio $t(u,v)/R_P^2(u,v)$ in (3.35) is, the expanded functions in (3.36) better approximate the original function at the (u,v) point. Therefore, parallelogram is constructed to be similar to the surface of the generalized quadrilateral in the vicinity of the singular point. It also needs to be tangential to the quadrilateral at the closest point projection (i.e. cpp point) so the analytic integral evaluation is enabled [40],[42]. The parametric surface is obtained by extending the element out of its finite bounds ($-1 \le u, v \le 1$) and the closest distance between the field point and the unbounded parametric surface containing the basis element (d) is obtained. The point on the unbounded parametric surface closest to the field point is called the closest point projection (cpp) and is computed using Newton-Raphson iteration procedure [48] solving the extremal problem

$$R = \| \mathbf{r}_\mathrm{F} - \mathbf{r}(u,v) \| \to \min \Leftrightarrow (\mathbf{r}_\mathrm{F} - \mathbf{r}(u,v)) \cdot (\mathbf{r}_\mathrm{F} - \mathbf{r}(u,v)) \to \min \ . \tag{3.37}$$

Once close projection point with (u_0, v_0) coordinate is computed, the position vector ($\mathbf{R}$) of the source point ($\mathbf{r}(u,v)$) to the field point ($\mathbf{r}_\mathrm{F}$) is expressed as

$$\mathbf{R}(u,v) = \mathbf{r}(u,v) - \mathbf{r}_\mathrm{F} = \mathbf{r}(u,v) - \mathbf{r}(u_0,v_0) - d\mathbf{n} = -d\mathbf{n} + \sum_{\substack{k=0 \\ k+l \ge 1}}^{K_u} \sum_{l=0}^{K_v} \mathbf{a}_{kl} \mathrm{d}u^k \mathrm{d}v^l \ , \tag{3.38}$$

where d is the distance of the field from cpp point, $\mathbf{n}$ is the unit normal to the (extended) quadrilateral surface at the (u_0, v_0) point, $\mathbf{a}_{kl}$ represents the k^{th} and l^{th} derivative of the quadrilateral surface at the (u_0, v_0) point with respect to u and v, and $\mathrm{d}u = u - u_0$ and $\mathrm{d}v = v - v_0$ are local coordinate distances between (u,v) and cpp point. The square of R is evaluated as:

$$R^2 = d^2 + (\mathbf{a}_{10} \cdot \mathbf{a}_{10} - 2d\mathbf{a}_{20} \cdot \mathbf{n})\mathrm{d}u^2 + (\mathbf{a}_{01} \cdot \mathbf{a}_{01} - 2d\mathbf{a}_{02} \cdot \mathbf{n})\mathrm{d}v^2 + 2(\mathbf{a}_{10} \cdot \mathbf{a}_{01} - 2d\mathbf{a}_{11} \cdot \mathbf{n})\mathrm{d}u\mathrm{d}v + \ldots \tag{3.39}$$

The parallelogram is then constructed at the close point projection as (in Fig. 3.2.):

$$R_P^2(u,v) = d^2 + b_u^2 \mathrm{d}u^2 + b_v^2 \mathrm{d}v^2 + 2b_u b_v \cos\alpha \mathrm{d}u\mathrm{d}v\,, \tag{3.40}$$

where b_u, b_v and cosα are defined to match the coefficients with same du/dv power in R^2 (3.39). Variable $t(u,v)$ is a polynomial of du and dv with all terms being the third or higher order which, in general, creates well approximated integrands in (3.36).

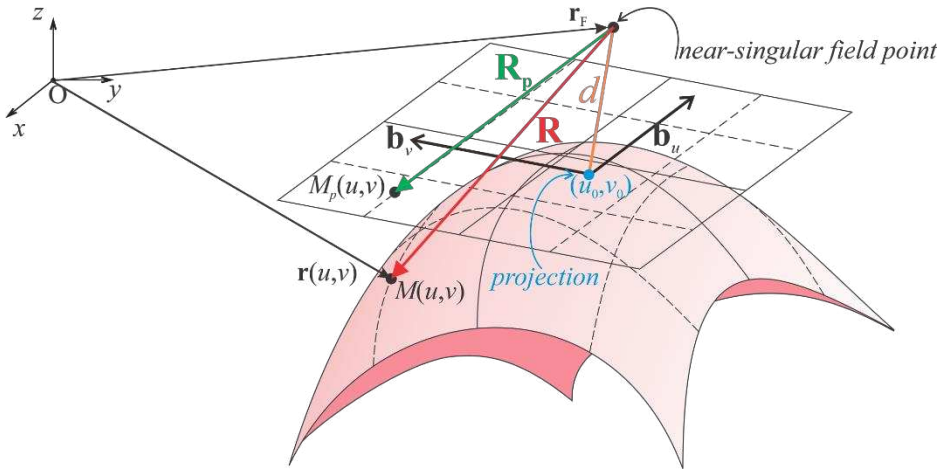

Fig. 3.2. The parallelogram constructed to be tangential to the quadrilateral element at the close point projection.

The ratio $t(u,v)/R_P^2(u,v)$ becomes relatively large if $R_P^2(u,v)$ is of the order or smaller than $t(u,v)$, leading to finite expansion in (3.36) being inferior approximation of the original function. This occurs when the term $2b_u b_v \cos\alpha \mathrm{d}u\mathrm{d}v$ becomes negative and close enough in value to the other terms in (3.40), i.e. when $\cos\alpha \mathrm{d}u\mathrm{d}v < 0$ and $|\cos\alpha|$ is relatively large. Consequently, element geometry is constrained to angles between 60° and 120°. i.e. $|\cos\alpha| \le 0.5$ over the basis element. For the cpp point outside of the element domain where the extension is defined as in (3.27), $|\cos\alpha|$ might be larger than 0.5 due to the large angle between $\mathbf{a}_{10}$ and $\mathbf{a}_{01}$ in (3.39). In these cases, element is extended using the first order parameters ($\mathbf{a}_{10}$ and $\mathbf{a}_{01}$) computed at the point on the patch domain closest to the field point, i.e. this is the most singular point on the patch. The close projection point is recomputed and parallelogram is constructed as previously. Note that now parallelogram and

quadrilateral coincide outside of the finite patch, so $t(u,v) = 0$ at the most singular point on the patch and $t(u,v)$ is not the polynomial function of the third order. The results computed in this manner and presented in Section 3.4 are labeled "corrected".

Integrals of the expanded functions (3.36) are computed as a sum of the analytically determined integrals over the parallelogram and are of the following form [42]:

$$I^{a}_{n,p,q} = \iint_{R_P} u^p v^q R^n_P \mathrm{d}u\mathrm{d}v\,, \tag{3.41}$$

where n takes values of odd integer between 3 and -9, p and q values depend on N_u and N_v orders (3.28) of the basis function and geometrical K_u and K_v orders of the quadrilateral having in mind that unitary vectors depend on the quadrilateral geometry (3.31). The parallelogram is divided into four triangles, each defined by cpp point and one side of the parallelogram. For some of the n, p, q values, integrals have known analytical formula. For other values of parameters, integrals (3.41) are recursively computed using the surface gradient identity. Note that the recursive implementation can rapidly loose precision which needs to be appropriately addressed. Details of the analytical integration over flat triangles with higher order basis functions are given in [40] and [42] provides detailed derivation for the higher order polynomial basis function over parallelogram extending the formulas in [40] for values of n smaller than -3.

3.4 Numerical results

Convergence (δ) of the numerical results presented in this section is computed as:

$$\delta = \log_{10} \frac{\left|\mathrm{real}(I(N_{\mathrm{GL}}) - \tilde{I})\right|}{\left|\mathrm{real}(\tilde{I})\right|} \text{ and } \Delta\delta = \delta_{\mathrm{new}} - \delta_{\mathrm{traditional}}\,, \tag{3.42}$$

where I represents the value of the integral computed over the surface by N_{GL} number of integration Gauss-Legendre points along one dimension, $\tilde{I}$ is integral evaluated at high number of N_{GL}

assuming it to be accurate, while $\Delta\delta$ is the difference between precision values computed for the new and traditional extraction methods. The traditional extraction method builds parallelogram using just the first order geometrical parameters, does not include the variation of the higher order basis functions over the patch and limits approximation to R_P^{-1} and R_P^{-3} terms from singular and hypersingular kernels (3.36), respectively.

One out of six second order elements in Fig. 3.3 describing sphere of unit radius is tested for different values of projection point coordinates and results are provided in Figs. 3.4-3.7. The results presented in Figs 3.4-3.5 assume projection points inside element geometry. The integrals are computed for i and j in (3.33)-(3.34) taking values between 0 and 6. a) to c) plots present convergence of the sample values of i and j while d) plot presents difference in integral convergence between new and traditional method for all i and j combinations. Novel method shows significant improvement over the traditional method.

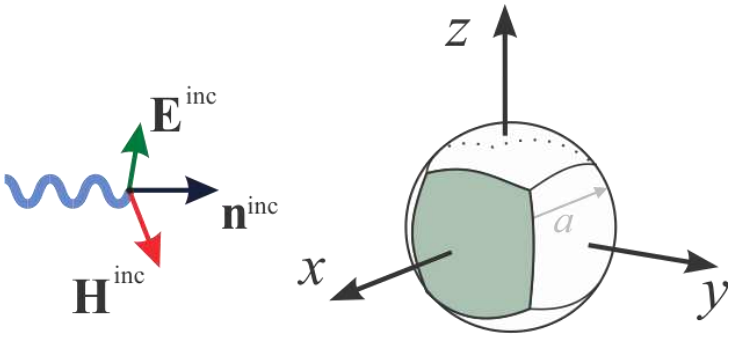

Fig. 3.3. Six surface element sphere model of the second geometrical order with radius a.

The results presented in Figs. 3.6-3.7 assume projection points outside element geometry. The integrals are computed using new and traditional method, as well as corrected new method. The integrals are computed for i and j in (3.33)-(3.34) taking values between 0 and 6. (a) to (c) plots present convergence of the example values of i and j while (d) plot presents difference in integral convergence between new corrected and traditional method with all i and j combinations.

Novel corrected method shows significant improvement over the traditional method, especially for the higher order basis functions.

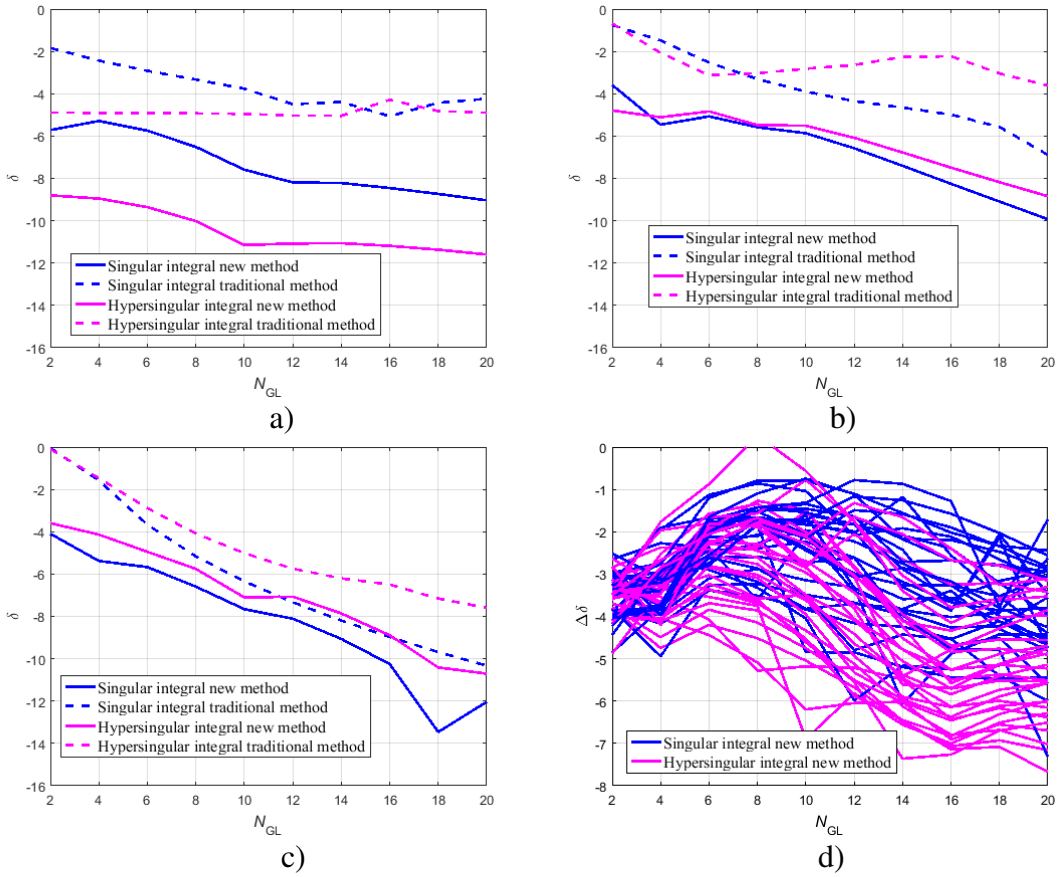

Fig. 3.4. Convergence results for the second order element in Fig. 3.3 for a=1m, $\gamma \approx$j0.7755rad/m, closest projection point coordinates u_0=0.1 v_0=-0.1 and d=10^{-5}m. (a) i=0, j=0; (b) i=3, j=4; (c) i=6, j=6;. (d) Difference in convergence between two methods for $i\epsilon$[0,6], $j\epsilon$[0,6].

3.5 Conclusion

Recently developed novel extraction method [42] incorporated in 2-D integral computation of the Double Higher Order Surface Integral Equation Method of Moments is presented with precision benefits over the traditional extraction method. This is achieved by incorporating higher order basis function and element approximation into computation of the parallelogram and analytic integral approximation. Further, method is improved to increase the accuracy in the cases showing precision tendencies inferior to the traditional method and results are presented.

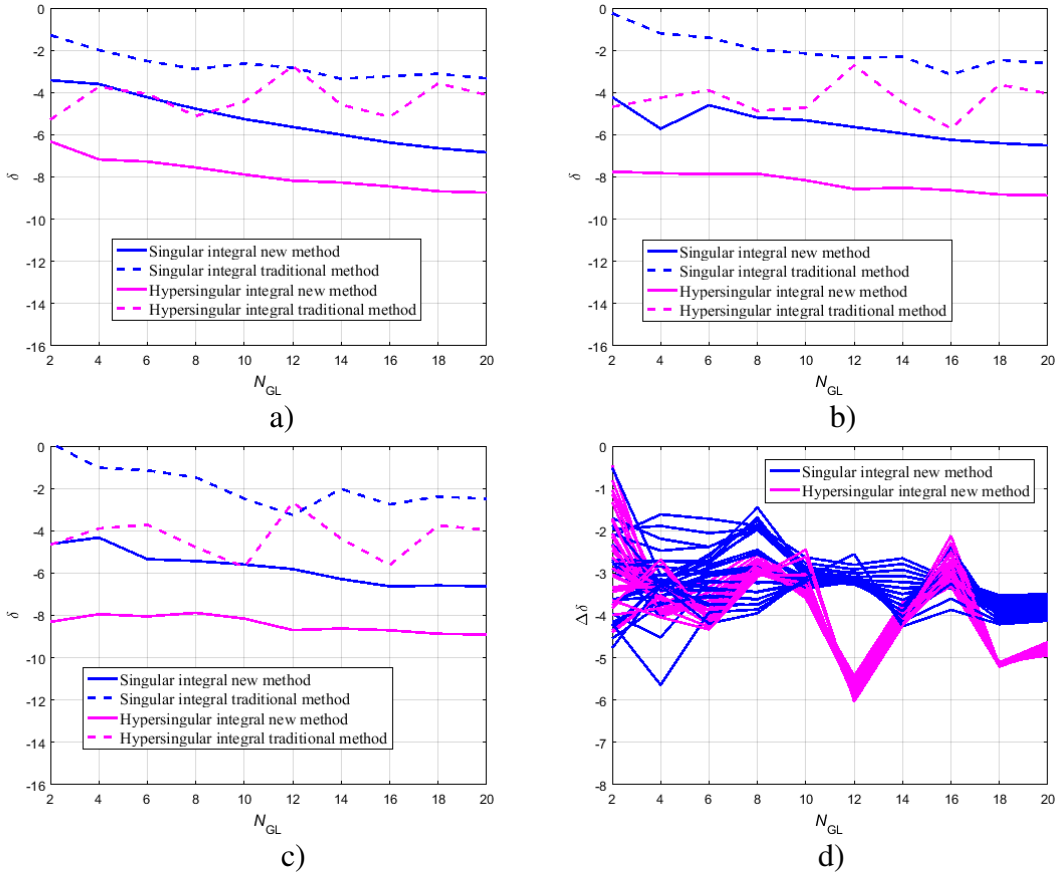

Fig. 3.5. Convergence results for the second order element in Fig. 3.3 for a=1m, $\gamma \approx$j0.7755rad/m, closest projection point coordinates u_0=0.9 v_0=0.9 and d=10^{-5}m. (a) i=0, j=0; (b) i=3, j=4; (c) i=6, j=6;. (d) Difference in convergence between two methods for $i\epsilon$[0,6], $j\epsilon$[0,6].

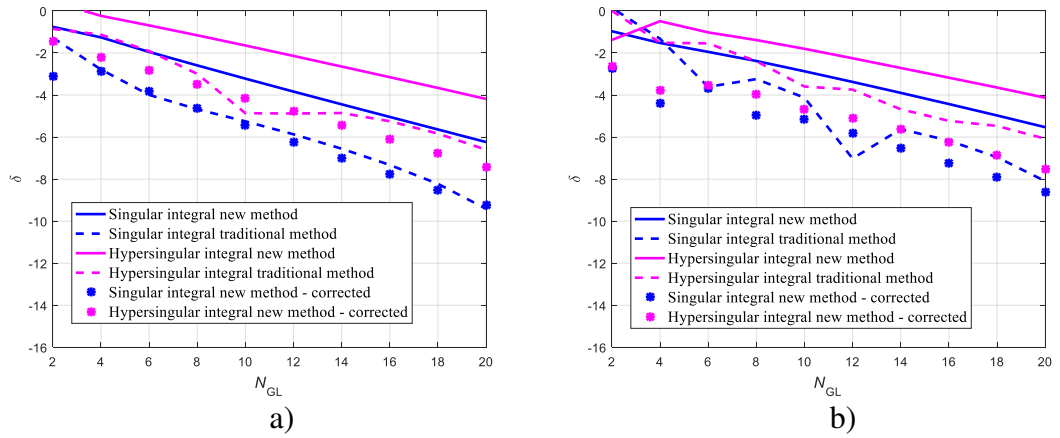

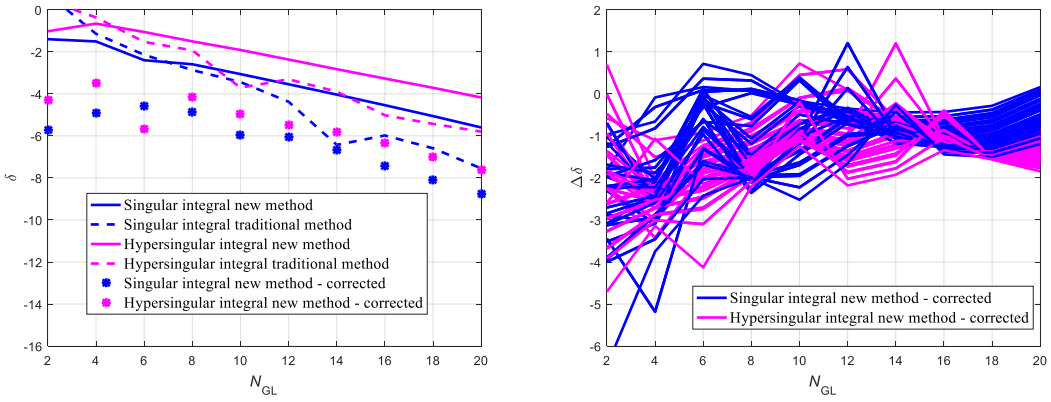

c) d)

Fig. 3.6. Convergence results for the second order element in Fig. 3.3 for a=1m, $\gamma \approx$j0.7755rad/m, closest projection point coordinates u_0=1.1 v_0=1.1 and d=10^{-5}m. (a) i=0, j=0; (b) i=3, j=4; (c) i=6, j=6;. (d) Difference in convergence between two methods for $i\epsilon$[0,6], $j\epsilon$[0,6].

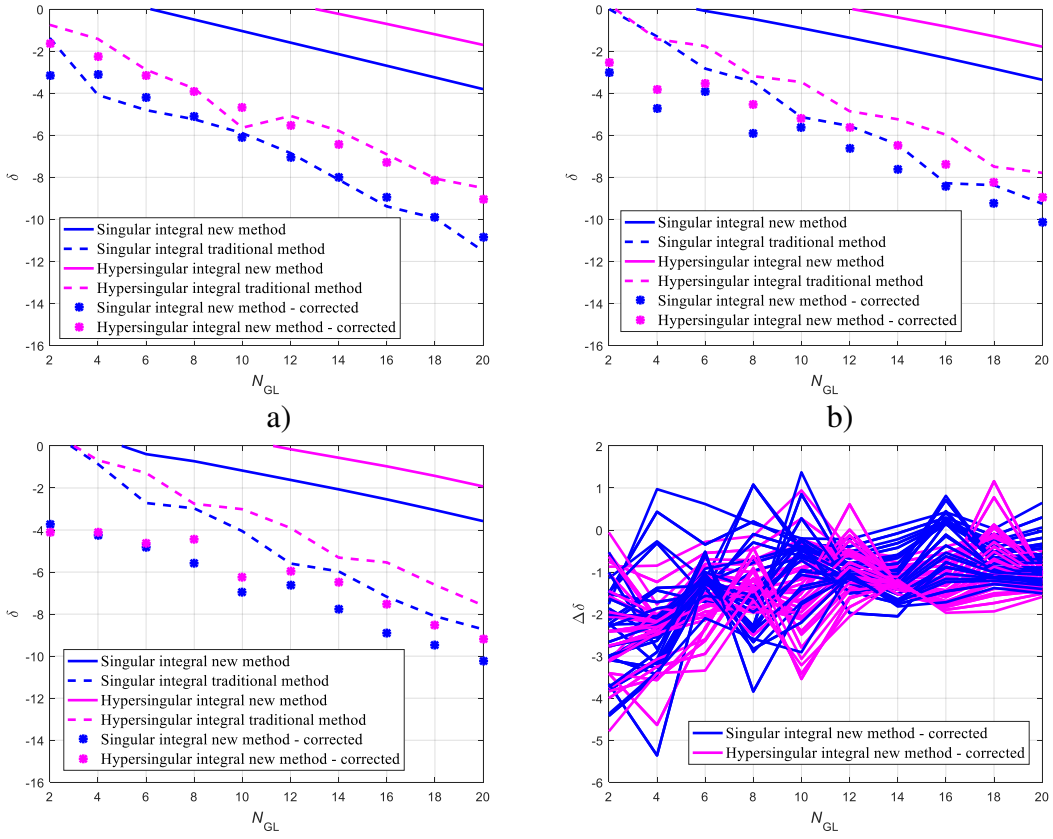

a) b)

c) d)

Fig. 3.7. Convergence results for the second order element in Fig. 3.3 for a=1m, $\gamma \approx$j0.7755rad/m, closest projection point coordinates u_0=1.2 v_0=1.2 and d=10^{-5}m. (a) i=0, j=0; (b) i=3, j=4; (c) i=6, j=6;. (d) Difference in convergence between two methods for $i\epsilon$[0,6], $j\epsilon$[0,6].

4 DOUBLE HIGHER ORDER MULTILEVEL FAST MULTIPOLE METHOD FOR ELECTRIC FIELD SURFACE INTEGRAL EQUATION

4.1 Introduction

The Double Higher Order (DHO) Method of Moments (MoM) techniques have been around for number of years [6]-[12], [16]-[22]. The Surface Integral Equation (SIE) based techniques [1]-[12] were efficiently used for predominantly homogenous, while Volume Integral formulations [13]-[22] for inhomogeneous objects. Aimed at the reduction of a total number of unknowns, these methods have demonstrated clear numerical advantages in discretization of the electrically large structures. However, due to high density of the final system of linear equations and a large condition number, the most popular approach to its solution is a direct LU factorization based solver. The memory required for the matrix storage as well as the complexity of the matrix solution with iterative solver is $O(N^2)$, while LU decomposition complexity is $O(N^3)$, where N is the number of unknowns. At the same time, due to rigorous inter element multidimensional integration of the Green's function, the matrix filling procedure complexity is $O(N^3)$. Therefore, at certain point, DHO MoM technique maximally utilizes system capacity and becomes inefficient.

Another approach to accelerate Integral Equation based solvers is the Fast Multipole Method (FMM) [23]-[26] and its multilevel version MLFMM [27]-[39]. In combination with iterative solvers [27]-[29], the complexity of this technique can be reduced to $O(N^{3/2})$ and even further to $O(N\log N)$. The base of the FMM approach is a representation of the fields radiated by one group of elements using the spherical multipole expansion [24]. Therefore, the interaction between two elements located far apart is computed as a combination of the group-to-group and intragroup interactions. The MLFMM technique has been proven to be extremely efficient, when applied to the lower order MoM-SIE approaches [27]-[32]. However, its benefits have been seldom

explored with higher order modeling [33]. This chapter focuses on the unique MLFMM implementation with the hierarchical divergence-conforming basis functions (3.30) defined on the higher order curvilinear quadrilateral discretization elements (3.27), [12].

4.2 Fast Multipole Method and Rokhlin's Translation

The foundation of the Fast Multipole Method (FMM) is a geometrical grouping of discretization elements, based on their central point location. The division of the model into groups is depicted in Fig. 4.1 as 2-D representation of the actual 3-D problem. The volume of the model is divided into 3-D grid, where each element discretizing the model is assigned to the group (grid element) containing its center. The matrix elements pertaining to interactions within the group or between the groups in the proximity are computed using Double Higher Order MoM-SIE as described in Section 3.2.1. However, interactions between the groups of basis functions defined on geometrical elements positioned sufficiently far can be approximated by Rokhlin's transfer function [24], which translates radiation pattern of one group to another and is defined as follows

$$T_L(\mathbf{k},\mathbf{r}_{ij}) = \sum_{l=0}^{L} (-\mathrm{j})^l (2l+1) h_l^{(2)}\left(k\left|\mathbf{r}_{ij}\right|\right) P_l\left(\hat{\mathbf{k}}\cdot\hat{\mathbf{r}}_{ij}\right) \tag{4.1}$$

where $\mathbf{k}$ is the wave number vector having the same direction as unit radial vector at the surface of the sphere, $\mathbf{r}_{ij}$ is the vector between the centers of *i*-th and *j*-th groups, $\hat{\mathbf{k}}$ and $\hat{\mathbf{r}}_{ij}$ representing unitary vectors, and $h_l^{(2)}$ and P_l are the spherical Hankel function of second kind and the Legendre polynomial of *l*-th order respectively. The truncation index *L* is computed as

$$L = kD + 1.8\beta^{\frac{2}{3}}(kD)^{\frac{1}{3}}, \tag{4.2}$$

where $D = \sqrt{3}d$ is the diameter of the group, *d* is the side length of the group, and $10^{-\beta}$ is the desired relative error [32].

Using Rokhlin's translation the Green's function g in equations (3.22)-(3.25) for sufficiently large R can be approximated as

$$g = \frac{\mathrm{e}^{-\mathrm{j}kR}}{4\pi R} \approx -\frac{\mathrm{j}k}{(4\pi)^2} \oiint e^{-\mathrm{j}k\hat{\mathbf{k}}(\mathbf{r}'-\mathbf{r}_i)} T_L\left(\mathbf{k}, \mathbf{r}_{ij}\right) e^{-\mathrm{j}k\hat{\mathbf{k}}(\mathbf{r}_j-\mathbf{r}'')} \mathrm{d}^2\hat{\mathbf{k}} \tag{4.3}$$

where $R=|\mathbf{r}'-\mathbf{r}''|$, $\mathbf{r}'$ and $\mathbf{r}''$ are position vectors at testing and basis elements, $\mathbf{r}_i$ and $\mathbf{r}_j$ are centers of i-th and j-th element groups, and integration is performed over the unit sphere. Taking into account that the gradient of the Green's function in the far field zone is $\nabla g \approx -\mathrm{j}kg\hat{\mathbf{R}}$, integrals in equations (3.22) and (3.23) can be represented as follows

$$\int_{S_m}\int_{S_n} \mathbf{J}_{\mathrm{S}m} \cdot \mathbf{J}_{\mathrm{S}n} g \mathrm{d}S_n \mathrm{d}S_m = \frac{\mathrm{j}k}{(4\pi)^2} \oiint \mathbf{\Psi}_{mi}\left(\mathbf{k}\right) \cdot T_L(\mathbf{k}, \mathbf{r}_{ij}) \cdot \mathbf{\Phi}_{nj}(\mathbf{k}) \mathrm{d}^2\hat{\mathbf{k}} \tag{4.4}$$

$$\int_{S_m}\int_{S_n} (\nabla_S \cdot \mathbf{J}_{\mathrm{S}m})(\nabla_S \cdot \mathbf{J}_{\mathrm{S}n}) g \mathrm{d}S_n \mathrm{d}S_m = \frac{\mathrm{j}k}{(4\pi)^2} \oiint \Psi'_{mi}\left(\mathbf{k}\right) \cdot T_L(\mathbf{k}, \mathbf{r}_{ij}) \cdot \Phi'_{nj}(\mathbf{k}) \mathrm{d}^2\hat{\mathbf{k}} \tag{4.5}$$

$$\begin{aligned} &\int_{S_m}\int_{S_n} -(\mathbf{M}_{\mathrm{S}n} \times \mathbf{J}_{\mathrm{S}m}) \cdot \nabla g \mathrm{d}S_n \mathrm{d}S_m = -\int_{S_m}\int_{S_n} \mathbf{J}_{\mathrm{S}m} \cdot (\nabla g \times \mathbf{M}_{\mathrm{S}n}) \mathrm{d}S_n \mathrm{d}S_m = \\ &= -\frac{k}{(4\pi)^2} \oiint \mathbf{\Psi}_{mi}\left(\mathbf{k}\right) \cdot T_L(\mathbf{k}, \mathbf{r}_{ij}) \left(\mathbf{k} \times \mathbf{\Phi}_{nj}(\mathbf{k})\right) \mathrm{d}^2\hat{\mathbf{k}} \end{aligned} \tag{4.6}$$

where m-th and n-th basis/testing functions belong to i-th and j-th group respectively,

$$\mathbf{\Phi}_{nj}(\mathbf{k}) = \mathbf{\Psi}^*_{nj}\left(\mathbf{k}\right) = \sum_{k_n=1}^{K_u} \sum_{l_n=0}^{K_v} k_n u^{i_n} v^{j_n} \mathbf{r}_{kl}^{(p)} \xi(i_n + k_n - 1, j_n + l_n) \tag{4.7}$$

$$\Phi'_{nj}(\mathbf{k}) = \Psi'^*_{nj}(\mathbf{k}) = i_n j_n \xi(i_n - 1, j_n) \tag{4.8}$$

$$\xi(i', j') = \int_{-1}^{1}\int_{-1}^{1} u^{i'} v^{j'} e^{-\mathrm{j}k(\mathbf{r}_j - \mathbf{r}(u,v))} \mathrm{d}u\mathrm{d}v \tag{4.9}$$

and $\mathbf{r}_{kl}^{(p)}$ are constant vector coefficients of p-th geometric element (3.27) and n is u directed basis function (3.30) with i_n and j_n orders in u and v directions. The integrals in equations (3.24) and (3.25) are computed similarly to (4.4)-(4.6).

The benefit of the FMM is in faster computation of Eqs. in (3.22-2.25) pronounced in conjunction with iterative solver, where matrix vector multiplication complexity is decreased because Z_{mn}, for the patches that are far away, is not explicitly computed but the matrix vector product. Building blocks enabling acceleration are Iterative solver (Section 4.3) and Aggregation, Translation and Disaggregation process described in Section 4.4.

4.3 Generalized Minimal Residual Method (GMRES) and Block-Diagonal preconditioner

Iterative solvers are used to compute an approximate solution to the matrix equation starting from an initial guess. In the process of solving, they generate the sequence of approximate solutions, each obtained from the previous solutions. The stopping criteria of the rounding error determines if the last approximate solution can be considered as the result. Iterative solvers are mainly used to solve non-linear equations, but employed as well for linear equations with large number of unknowns due to lower complexity compared to the direct solvers computing the exact solution.

Krylov subspace methods (e.g. Arnoldi, Lanczos, Conjugate gradient(CG), Generalized Minimal Residual Method (GMRES), Biconjugate Gradient Stabilized (BICGSTAB)) are commonly used in SIE-MoM ([27]-[29] and Section 1.3) building a linear subspace for the approximate solution. The maximum number of iterations will give the exact solution but much smaller number of iterations usually gives approximation satisfying needed accuracy, especially if appropriate preconditioning is applied. Preconditioner is a matrix multiplying both left and right hand side of the matrix equation decreasing the system's condition number, creating an equivalent system which will reach given accuracy in less iterations than original system. The main bottleneck in iterative solvers' application is matrix vector multiplication in the process of building the subspace. The matrix vector multiplication (y) is conducted using following notation

$$y = [Z]x = [Z^{\text{near}}]x + [Z^{\text{far}}]x = y^{\text{near}} + y^{\text{far}}, \tag{4.10}$$

where x is the last approximate solution and interaction between elements in the proximity are computed with full MoM-SIE ([12]) labeled with $[Z^{\text{near}}]$ (3.22)-(3.25) and far field interactions $[Z^{\text{far}}]$ are implicitly computed using FMM group interactions (4.4)-(4.6). Complexity of matrix vector multiplication using full matrix storage is $O(N^2)$, while using FMM approximation is $O(N^{3/2})$ and $O(N\log N)$ for its multi-level form. We have implemented GMRES for complex equation systems [49] and Block-Diagonal preconditioner constructed from blocks of inverse of the intragroup interactions.

4.4 Aggregation and Disaggregation processes

Fast matrix vector multiplication (4.10) is enabled by FMM's Aggregation and Disaggregation processes explained on the example of interactions between testing and basis functions defined on S_i and S_j surface elements representing all elements belonging to the i-th testing and j-th basis groups respectively. Aggregation assumes the process of summation of transmitting radiation patterns (4.7) coming from all source (basis) currents at the j-th group at the group's center for each wave vector $\mathbf{k}$ (current coefficients being the last approximate solution x)

$$\mathbf{\Phi}^{s}_{j}(\mathbf{k}) = \sum_{f_n \text{ on } S_j} \mathbf{\Phi}_{nj}(\mathbf{k}) x_n, \tag{4.11}$$

depicted by green arrows in Fig. 4.1. The transmitting radiation pattern of the j-th group ($\mathbf{\Phi}^{s}_{j}(\mathbf{k})$) is then translated to the center of the i-th group, for each wave vector $\mathbf{k}$, using Rokhlin's translation ($T_L(\mathbf{k},\mathbf{r}_{ij})$), represented by black arrow in Fig. 4.1.

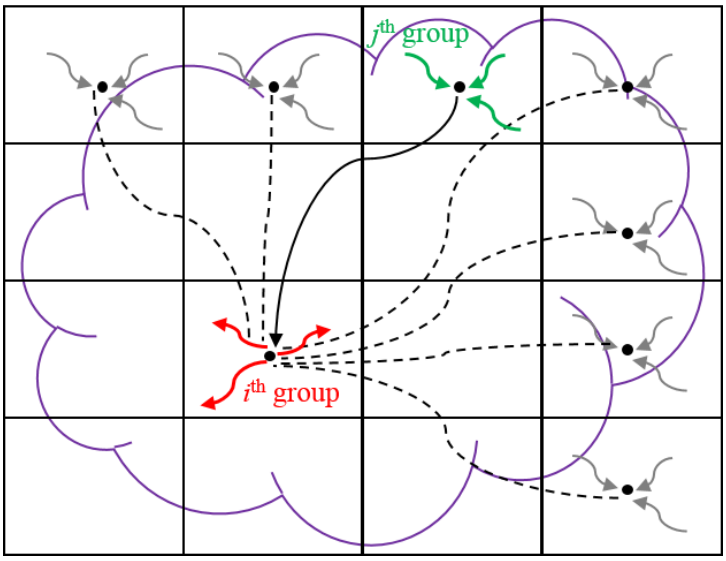

Fig. 4.1. 2-D representation of Aggregation (at *j*-th FMM group) and Disaggregation (at *i*-th FMM group) processes.

Transmitting radiation patterns originating from all the groups that are in the far field zone of the *i*-th group are translated and summed at its center. Disaggregation processes at the *i*-th group, represented by red arrows in Fig. 4.1, computes y_m^{far} coefficient (4.10), where *m*-th basis/testing function belongs to the *i*-th group, by multiplying far field radiation influences summed at the center of *i*-th group by its receiving radiation pattern $\mathbf{\Psi}_{mi}(\mathbf{k})$ (4.7) and performing integration over the unit sphere (i.e. over $\mathbf{k}$ values). The disaggregation process is repeated for each testing function defined on the elements of the *i*-th group. The process of computing the y^{far} coefficients in (4.10), thus can be mathematically described using (4.5)

$$y_m^{\text{far}} = \sum_{j \in farfield} Z_{mn} x_n = -\frac{k}{(4\pi)^2} \oiint \mathbf{\Psi}_{mi}(\mathbf{k}) \cdot \sum_{j \in farfield} T_L(\mathbf{k}, \mathbf{r}_{ij}) \cdot \left(\mathbf{k} \times \sum_{f_n \text{ on } S_j} \mathbf{\Phi}_{nj}(\mathbf{k}) x_n \right) \mathrm{d}^2\hat{\mathbf{k}}, \qquad (4.12)$$

and is employed on the Eqs. (4.4) and (4.6) in the similar fashion.

The acceleration in the computation comes from the fact that Aggregation process is done just once for each group and results are stored. The transmitted far field radiation patterns are than translated to the centers of each testing group and summed, followed by disaggregation process to

each testing function (done only once per iteration) and integration over the unit sphere ending in MVM coefficient computation.

4.5 Multilevel Fast Multipole Method (MLFMM)

MLFMM is multi-level version of FMM algorithm that accelerates MVM even further using Octree grouping scheme [50], three level grouping is shown in Fig. 4.2. The model domain is divided by two in each dimension (the coarsest grouping is boxed in maroon), then each of the domain of the first level groups is halved in each dimension to get the second level groups (boxed in blue). The third level (the finest grid in this case) groups are boxed in black. For each level, it is decided which pairs of groups are in the far field zone and which are in the near field zone. In Fig. 4.2., none of the pairs of the coarsest groups can be considered to be in far field zone being the neighboring groups.

Two level FMM is depicted in Fig. 4.2 using black and blue boxed groups for finer (higher) and coarser (lower) level FMM approximation, respectively, maintaining the color code with group names. Some of the finest level FMM intergroup interaction is computed as explained in previous section (e.g. interaction between the *i*-th and the *j*-th group as well as between *i*-th and the *l*-th group in Fig. 4.2). In the case two groups of the highest (finest) level are situated further away, their interaction can be computed through the coarser level FMM, e.g. interaction between the *l*-th and the *j*-th group in Fig. 4.2 can be computed through *h*-th and *f*-th groups interaction, assuming the coarser groups are in the far-field zone. The transmitting radiation pattern of the *j*-th group is aggregated at its center as in the previous Section. It is then translated to the center of the coarser level group (the *h*-th group) and summed with radiation patterns coming from all other finer level groups contained in the *h*-th group. The *h*-th group transmitting radiation pattern is then translated using Roklin's translation to the center of the *f*-th group for each wave vector **k** as

described in previous Section. The radiation pattern received is translated to the center of the *l*-th group and summed with radiation patterns received from interactions in the finest level (e.g. from the *i*-th group). The disaggregation process with integration over unit sphere follows computation MVM product. If described process is expanded to the multi-level grouping scheme, it is called MLFMM which can achieve $O(N\log N)$ complexity of the method. Note that the integration over unit sphere is always done on the finest level having the smallest number of integration points.

4.5.1 Interpolation, Translation and Anterpolation process

The multi-level computation is enabled by incorporating Interpolation, Translation and Anterpolation processes into inter level transfer of the radiation patterns. Integration over unit sphere is computed using N_ϕ uniformly chosen samples in ϕ direction and N_θ Gauss-Legendre points in θ direction, where $N_\phi=2N_\theta=2(L+1)$, where L is given in (4.2). The sampling rate depends on the size of the group, entailing more integration points for larger groups, i.e. different FMM levels require different number of sampling points on the unit sphere.

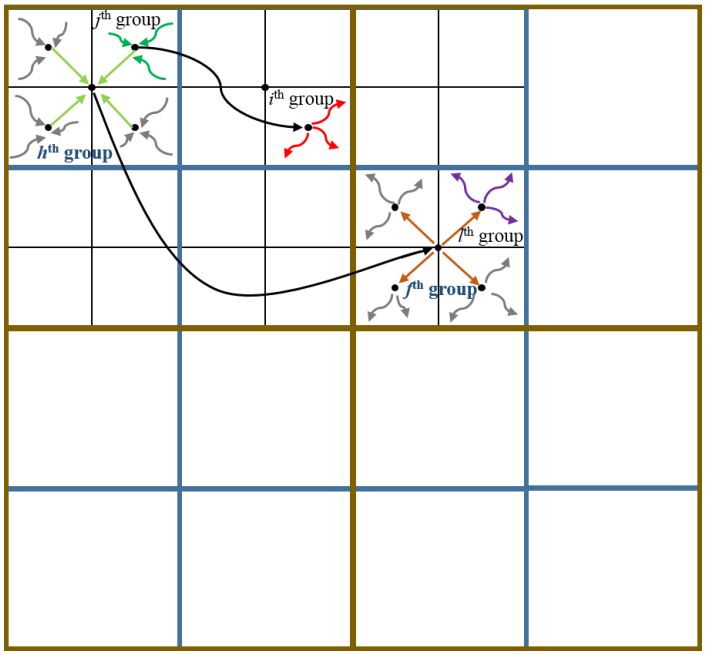

Fig. 4.2. 2-D representation of two level FMM and three level Octree scheme.

In order to transfer radiation pattern from the finer level to the coarser level, it is computed at integration points of the coarser level via two stage 2-D Lagrange interpolation process employing 2*p* x 2*p* points [51], where *p* is an input parameter controlling the accuracy. It is then translated to the center of the coarser group ($\mathbf{r}_h$) by multiplying radiation pattern with $e^{-\mathrm{j}k\hat{\mathbf{k}}\cdot\mathbf{r}_{jh}}$, where $\mathbf{r}_{jh} = \mathbf{r}_j - \mathbf{r}_h$. Similar process is done when transferring radiation pattern from the coarser to the finer grid level. It is translated from the center of the coarser ($\mathbf{r}_f$) group to the finer level group's center (i.e. $\mathbf{r}_l$) by multiplying radiation pattern with $e^{-\mathrm{j}k\hat{\mathbf{k}}\cdot\mathbf{r}_{fl}}$, where $\mathbf{r}_{fl} = \mathbf{r}_f - \mathbf{r}_l$. The radiation pattern then undergoes the anterpolation process (transpose interpolation) to evaluate its values at the integration points of the finer level.

4.6 Numerical Results and Discussion

4.6.1 PEC sphere modeled with FMM approximation

Verification example is unit radius PEC sphere with 600 elements divided into 200 FMM groups in Fig. 4.3. The sphere is analyzed at 1.2 GHz, so the cube encompassing the structure is 8λ large, where λ is wavelength in air. Iterative solver achieved 0.1154E-12 error. Size of the FMM group is λ and far field is assumed if the distance between group centers is 4λ. Results are compared to the full SIE matrix storage and direct solving with LU decomposition. Numerical parameters for both methods were kept $N_u = N_v = 2$ and $NGL_u = NGL_v = 8$ for both inner and outer integration per element.

4.6.2 Dielectric sphere modeled with FMM approximation

Another verification example is unit radius sphere with 600 elements and dielectric constant $\varepsilon_r = 2.25$. The sphere is analyzed at 600 MHz and there is 56 FMM groups. Iterative solver achieved 0.824642E-8 error. Size of the FMM group is λ and far field is assumed if the distance

between group centers is 4λ. Results, in Fig. 4.4, as a function of azimuthal angle and excitation of E_θ=1 V/m at $\phi_{inc} = 0^o$ and $\theta_{inc}=90^o$, are compared to the full SIE matrix storage and direct solver with LU decomposition. Numerical parameters for both methods were kept $N_u=N_v=2$ and $NGL_u=NGL_v=10$ for both inner and outer integration per element. The cross-polarization error in this case comes both from convergence accuracy provided to iterative solver as input as well as FMM approximation error.

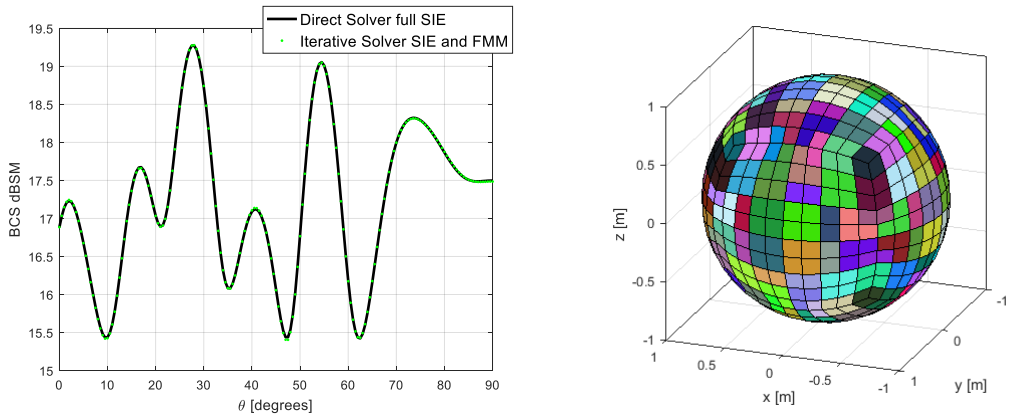

a) b)

Fig. 4.3. (a) Bistatic radar cross-section results for the first order PEC sphere at frequency f=1.2 GHz. (b) Sphere model with FMM groups in distinctive colors.

4.6.3 Interpolation example

For the verification purposes, interpolation implementation is tested on the 1 m^2 square metallic patch at 300 MHz, numerical parameters being $N_u=N_v=3$ and $NGL_u=NGL_v=20$ and the distance from the patch is 100 m in the direction normal to the element. Excitation is plane wave with θ component of the electric field being 1 V/m and incidence direction of $\phi_{inc} = 0^o$ and $\theta_{inc}=90^o$. Consider the sample point close to the pole with coordinates $\theta_s = 3.0698$ rad and $\phi_s = 0$ rad which is part of the finer grid determined by $N_\phi=2N_\theta=66$. In general, the results at points closer to the poles of the unit sphere are interpolated with lower accuracy due to coarser point distribution in the vicinity of the pole.

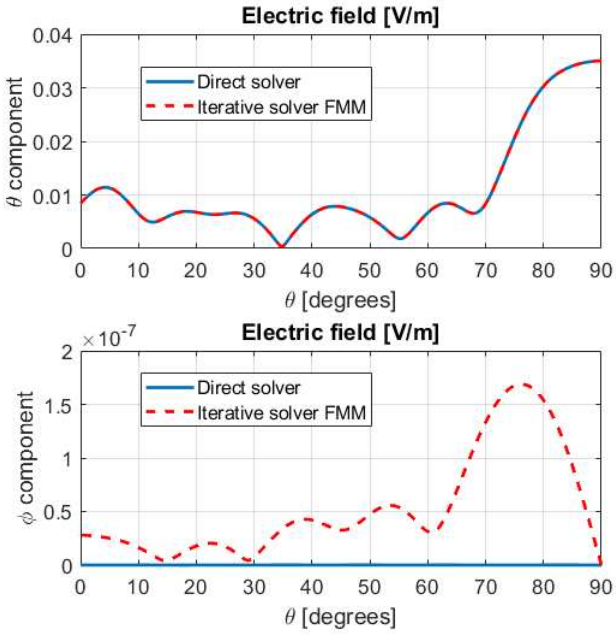

Fig. 4.4. Bistatic radar cross-section results for the first order dielectric sphere at 600 MHz.

The values of the radiation pattern computed using (4.7) at coarser grid determined for $N_\phi=2N_\theta=40$ (blue points in Fig. 4.5), are used to approximate the radiation in the sample point with (θ_s, ϕ_s) coordinates (red star in Fig. 4.5). The resulting x-component of the original radiation and its approximation, computed by means of using 2-D Lagrange interpolation process with $p=3$, give 7.2923e-04 and 2.6395e-04 relative error for real and imaginary component, respectively. Radiation function computed at coarser grid by means of (4.7) (blue points) and the approximated value (red star) are plot in Fig. 4.6 real and imaginary parts in separate plots.

4.7 Summary and Future Work

This chapter presented FMM and its Multi-Level approximation incorporated with double-higher order SIE-MoM solved by iterative solver (GMRES) and the specific implementation details are provided. The accuracy of FMM combined with GMRES is verified on the example of a large sphere model and interpolation implementation is tested on a metallic patch example. The FMM implementation presented has been used in master thesis and development of Randomized

Hierarchical Semi-Separable Structures solver for SIE-MoM [166]. Future work assumes further testing that will show $O(N^{3/2})$ and $O(N\log N)$ complexity is achieved by FMM and its Multi-Level approximation respectively. In order to analyze larger structures where the asymptotic behavior can be obtained, code needs to be changed for parallel execution, which is well known scalability issue for iterative solvers.

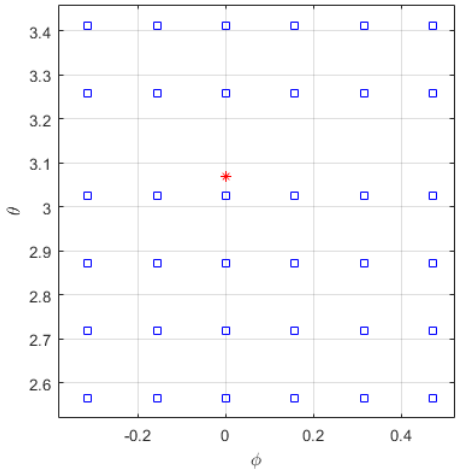

Fig. 4.5. Illustration of interpolation grid for red point and p=3 with coarser grid points in blue.

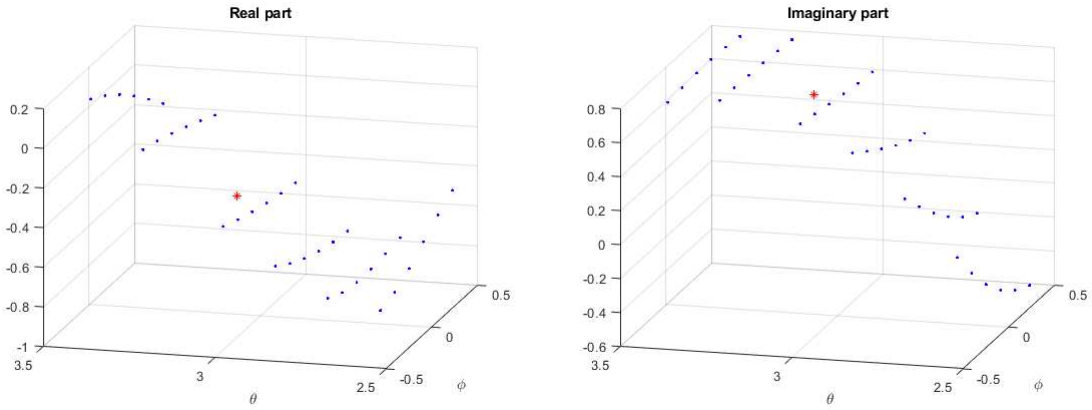

a) b)

Fig. 4.6. Radiation (4.7) computed at coarser grid points and interpolated value (red star) for the example in Fig. 4.5 (a) Real and (b) Imaginary part.

5 SCATTERING CALCULATIONS FOR ASSYMETRIC RAIN DROPS DURING A LINE CONVECTION EVENT: COMPARISON WITH RADAR MEASUREMENTS[2]

5.1 Introduction

Polarimetric weather radars make use of the oblate shapes and high degree of orientation of raindrops in order to better estimate rainfall rates from the retrieved raindrop size distributions [135][136]. As a first step, they utilize the differential reflectivity (Z_{dr}) along with the conventionally measured co-polar reflectivity (Z_h), to reduce uncertainties in estimating the drop size distribution within the radar pulse volume [111]. The equilibrium shapes of raindrops are size dependent [108] and they are generally approximated by oblate spheroids whose axis ratios (minor to major) decrease monotonically with increasing size. Drops with diameters smaller than 0.8 mm can be considered almost spherical. For larger drops (>2.5 mm) the concept of dynamic equilibrium shape was introduced by Szakáll [137] to describe the time-averaged axis ratios due to drop oscillations observed in a wind tunnel which was also confirmed using the concept of 'most probable' shapes from 2-D video disdrometer (2DVD; [131]) by Thurai et al. [140]. It is now well-known that axisymmetric drop oscillations dominate the background state with smaller amplitude mixed oscillation modes that give rise to *asymmetric* shapes [109]. However, there is no theoretical framework for modeling such *asymmetric* shapes in natural rainfall. Hence, the common approach is to neglect the variance of drop shapes and to relate the mean axis ratio with drop equi-volume diameter (D_{eq}) ([108],[110],[139]).

Asymmetric drops were inferred from 2DVD measurements in a highly-organized line convection rain event described in Thurai et al. [143]. During this event a significant fraction of

[2] Reprinted, from "Manić, S.B., M. Thurai, V.N. Bringi and B.M. Notaroš, "Scattering Calculations for Asymmetric Raindrops during a Line Convection Event: Comparison with Radar Measurements", *J. Atmos. Oceanic Technol.,* vol. **35**, pp. 1169–1180 " © American Meteorological Society. Used with permission.

drops (around 30%) within the line convection were *asymmetric*. Eight individual *asymmetric* drops were chosen from the 2DVD measurements to reconstruct their 3D-shapes (Thurai et al.[145]) and to determine their individual scattering amplitudes at C-band using the method of moments in the surface integral formulation (MoM-SIE) [114]. Scattering calculations for the individual asymmetric drops showed that the single particle differential reflectivity (Z_{dr}) values differed from those calculated assuming rotationally symmetric shapes. Differences were also seen in the case of (single particle) specific differential phase (K_{dp} factor) as well as linear depolarization ratio (LDR).

Accurate simulations of radar observables require accounting for variance of drop shapes which requires computation of drop-by-drop scattering amplitudes and integration of the elements of the covariance matrix over a given measurement interval [111]. The aforementioned line convection event is analyzed in this manner herein using 3D- reconstruction of drop shapes from 2DVD disdrometer data. Radar reflectivity, differential reflectivity, copolar correlation coefficient and specific differential phase are computed with 1-min time resolution and compared to radar measurements extracted over the 2DVD site from the University of Alabama in Huntsville Advanced Radar for Meteorological and Operational Research (ARMOR) C-band radar (see [128],[116]). The radar is 15 km away from the ground instrument site and the height of the resolution volume is around 340 m at the lowest elevation angle of 1.3°. For completeness the linear depolarization ratio is also computed even though the radar is not configured for measuring LDR. The drop-by-drop scattering simulations are compared with the bulk method which refers to the use of the T-matrix scattering code [107] with input being the 1-minute averaged drop size distributions from 2DVD, the oblate axis ratios from Thurai et al. [139] with Gaussian canting angle distribution [mean=0°, σ=5°].

This paper is organized as follows. Section 5.1 is reserved for the details of raindrop model construction, used as input to the scattering code. In Section 5.2, for validation purposes, we consider an example of an *asymmetric* drop that is reconstructed from 2DVD measurements [145] and the results obtained by our electromagnetic solver (MoM-SIE) are compared to those using an industry standard software. We then consider, in Section 5.5, the line convection event and compare radar measurements with scattering simulations using drop-by-drop as well as the bulk method. The paper concludes with a short Discussion and Conclusions section.

5.2 Methodology: numerical solution

Raindrop scattering calculations assuming oblate (or rotationally symmetric) shapes typically use the T-matrix method ([146],[107],[126]) which is widely used by the radar meteorology community (see, also, Chobanyan et al. [114] and references therein for a review of different scattering methodologies including discrete dipole approximation, surface and volume integral formulations used for precipitation particles).

Scattering calculations are performed herein using a higher order method of moments solution to the electric and magnetic field surface integral equations (MoM-SIE) based on boundary conditions between air and water dielectric at the rain drop surface, S_a, i.e., the continuity of tangential components of total (incident plus scattered) electric/magnetic fields ([127],[12], Section 3.2)

In our current work using the MoM-SIE methodology, a geometrical model is obtained by discretization of the raindrop surface using Lagrange-type curved parametric quadrilateral elements of arbitrary orders ([12],[114]). The method directly solves for an approximation of fictitious surface electric and magnetic current densities, $\mathbf{J}_s$ and $\mathbf{M}_s$, over the rain drop boundary

using hierarchical divergence-conforming polynomial basis functions, defined over quadrilateral elements ([12],[114] and Section 3.2).

For a given incident wave, the scattered electric field is represented as the following function of current densities Eq. (3.4):

$$\mathbf{E}^{\text{scat}}(\mathbf{J}_s, \mathbf{M}_s, \varepsilon) = -\mathrm{j}\omega\mu_0 \int_{S_a} \left(\mathbf{J}_s g + k^{-2} \nabla_s \cdot \mathbf{J}_s \nabla g \right) \mathrm{d}S_a + \int_{S_a} \mathbf{M}_s \times \nabla g \mathrm{d}S_a \,, \tag{5.1}$$

where g ($g = \mathrm{e}^{-\mathrm{j}kR} / 4\pi R$) and k ($k = \omega\sqrt{\varepsilon\mu_0}$), respectively, are Green's function and wave number for the unbounded medium of parameters $\varepsilon = \varepsilon_r\varepsilon_0$ and μ_0, with R being the distance of the field point from the source point, $\omega = 2\pi f$ the angular (radian) frequency, and ε_r the dielectric constant of the rain drop (water). Magnetic field is expressed in a similar fashion.

When the distance R in (1) is zero or relatively small, the singular or near-singular terms are extracted and evaluated analytically, and the remaining non-singular integrals are calculated numerically using Gauss-Legendre integration formulas. The final matrix equation is obtained after the Galerkin testing procedure has been applied to boundary condition equations, which assumes another surface integration of the SIEs with testing (weighting) functions being equal to the basis functions.

For verification purposes, another method that utilizes 3-D geometrical discretization is considered and results are presented in terms of single particle dual-polarization scattering for three different frequency bands.

5.3 Raindrop modelling

Drop shapes recorded by the 2DVD are used for 3D-reconstruction (for $D_{eq} > 2$ mm) using the algorithm in Schönhuber et al. [132]. Drops with $D_{\text{eq}} < 2$ mm are assumed to have oblate spheroidal shapes with axis ratio as a function of D_{eq} given in [139]. The 3D-reconstruction

procedure give rises to more significant errors for small drops (due to resolution of 170 μm) and hence the 2 mm threshold was applied. Note also that the larger drops will have more of an effect on Z_{dr} than the small drops.

Details of the 3D-shape reconstruction of each recorded drop from its images from the two orthogonal cameras have been published previously ([132],[134]) hence only a brief summary is given here. The 2DVD measures drop contours in two perpendicular planes which can be skewed due to horizontal component of the drop velocity (typical in line scan camera systems). For drops that possess an axis of symmetry, the contours can be deskewed as described in ([130],[118]); in addition, the horizontal velocity can be estimated. In the Appendix of Thurai et al. [145], the horizontal drop velocities derived from the deskewing procedure were shown to be in excellent agreement with the independent wind sensor measurements, both in magnitude and in direction. For deskewing *asymmetric* drops the horizontal velocity must be estimated. This is achieved from the drop horizontal velocities estimated from the deskewed symmetric drops closest in time and size to the *asymmetric* drop (see Section IV of Schönhuber et al. [132]). One limitation of this method for *asymmetric* drops relates to the uncertainty in the exact drop horizontal velocity required as input to the deskewing procedure. However, apart from errors due to rapid fluctuations in wind velocities, we expect the reconstructed shapes to be reasonably representative of their true 'instantaneous' shapes.

The deskewed contours in the two orthogonal planes are sampled at equidistant values along the vertical axis and four points are obtained at each height (note that for rotationally symmetric drops the thin 'slices' along the vertical axis are elliptical and the 3D shape is based on stacked ellipses). For asymmetric drops, four different ellipse quarters are constructed for each slice having in mind the center point. The points describing the geometry of each slice are obtained

by sampling the constructed elliptical quarters in uniform intervals of the azimuth angle. The procedure is repeated for each slice in order to create the 3D-reconstructed drop, an example of which is shown in Fig. 5.1. In our models, the shapes of the slices are limited to convex shapes, i.e. the center point needs to be inside or part of the circumference.

The model of the drop is created by defining first order (bilinear) quadrilateral elements, each between four points of the geometry (Thurai et al. [145]). To define one element, two points are chosen with the same coordinate value on the z axis and sequential values on the azimuthal coordinate. Two other points are chosen to have the same azimuth angles but different, consecutive z axis values compared to the two already chosen points. After creating all the elements by connecting pairs of points from groups with consecutive values on the z axis, the elements at the top and the bottom of the drop are defined using all four points from the group having the same z axis value, the highest and the lowest, respectively, so the entire surface of the drop is discretized. The order of the basis functions ([12] and Section 3.2.3) used for the unknown expansion over the elements was chosen to comply with Klopf et al. [123].

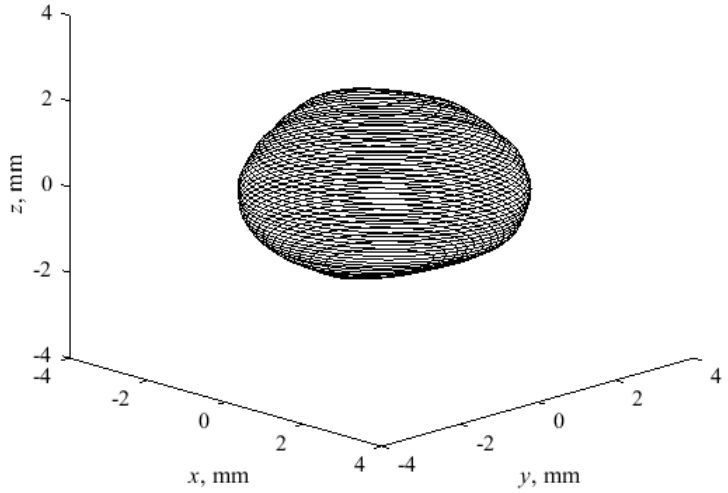

Fig. 5.1. Reconstructed drop from 2DVD measurements in natural rain (equi-volume drop diameter = 4.81 mm).

5.4 Validation of the MoM-SIE method

The single particle differential reflectivity, Z_{dr} (expressed as a ratio) is given by:

$$Z_{dr} = \frac{|S_{hh}|^2}{|S_{vv}|^2}, \tag{5.2}$$

where S_{hh} and S_{vv} are the frequency-dependent backscatter amplitudes for horizontal (h) and vertical (v) polarizations. Fig. 5.2 shows the calculated Z_{dr} for the reconstructed drop in Fig. 5.1 as a function of the ('look') azimuthal angle ϕ, for S, C, and X bands. In all three cases, the Z_{dr} variation with ϕ is significant, whereas for a rotationally symmetric drop the Z_{dr} is ϕ-independent, with values of 3.0, 3.7, and 3.2 dB, respectively, marked as '+' points. Fig. 5.2 also shows that C-band variation lies well above the S and X band variations, which can be attributed to this particular drop size (D_{eq} = 4.81 mm) lying in the C-band resonance scattering region (e.g., Carey and Petersen [113]). The ϕ-angle variation at C-band is also slightly higher than those at S and X bands.

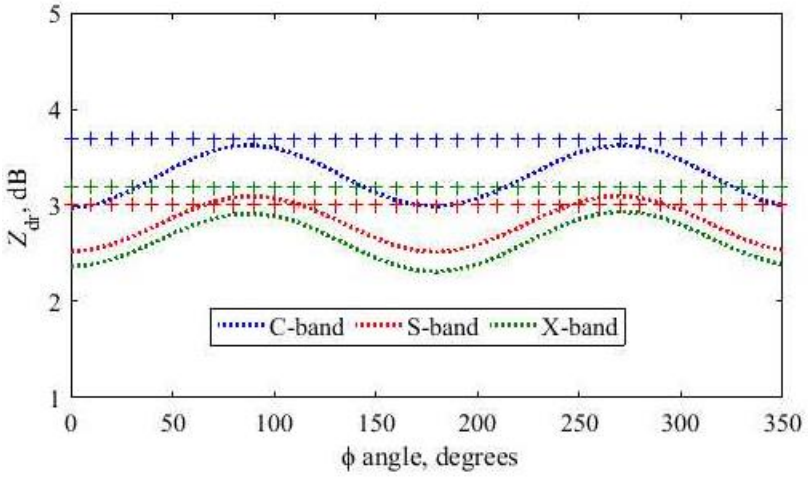

Fig. 5.2. Variation of Z_{dr} (in dB) with 'look angle' ϕ, in horizontal plane, for C, S, and X bands shown as dotted lines for the reconstructed drop in Fig. 5.1. The '+' marks represent the corresponding Z_{dr} values for the most probable shapes.

Although Fig. 5.2 shows a somewhat periodic variation with the ϕ-angle for all three frequency bands, the real and imaginary parts of S_{hh} and S_{vv} do not necessarily show the same

trend. As an example, Fig. 5.3 shows these variations for C-band. The imaginary part of S_{hh} and S_{vv} show non-periodic variations but their amplitudes are considerably lower than the corresponding real parts. It turns out that the Z_{dr} variation is much more governed by the variation in $Re(S_{hh})$ and $Re(S_{vv})$ than by $Im(S_{hh})$ and $Im(S_{vv})$.

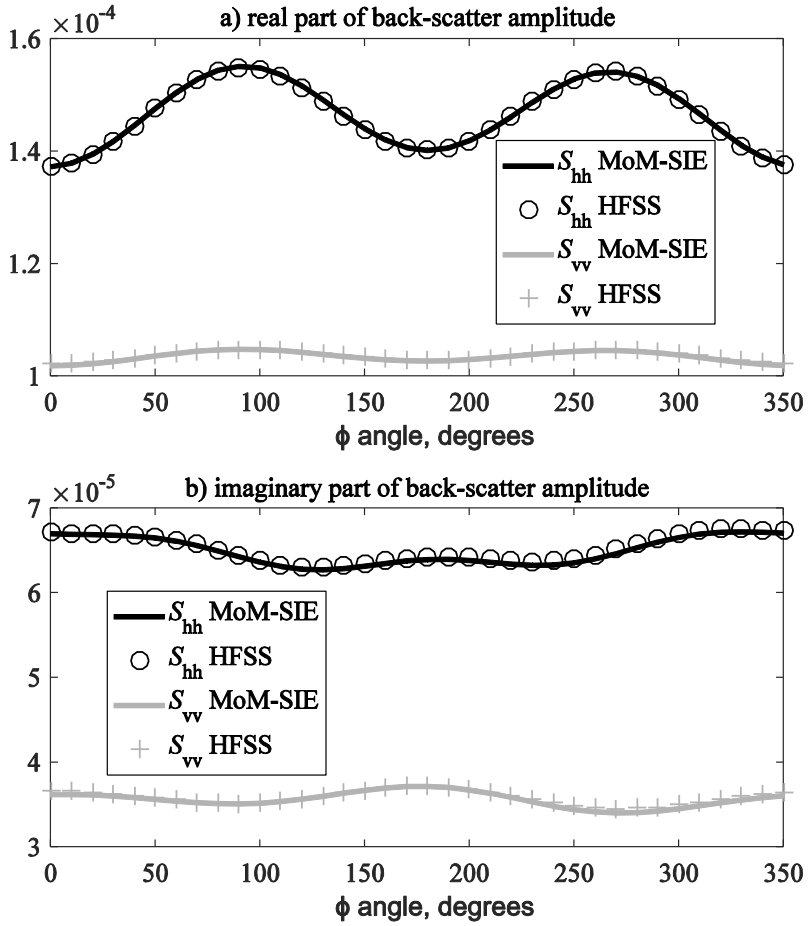

Fig. 5.3. (a) Real part and (b) imaginary part of C-band back-scatter amplitudes as a function of ϕ, in horizontal plane, for h and v polarizations, for the reconstructed drop given in Fig. 5.1. Computations using MoM-SIE and HFSS-FEM methods are displayed.

By way of verification of the MoM-SIE based scattering amplitude results, another method that uses 3-D discretization, namely, ANSYS HFSS code[3] (industry standard utilizing the volumetric finite element method – FEM, so numerically very different from the MoM-SIE

[3] See: http://www.ansys.com/products/electronics/ansys-hfss

approach), is employed. Results by the FEM (HFSS) with the computational region truncated by means of a perfectly matched layer (PML) are also included in Figs. 5.3(a) and 5.3(b). As can be seen, the resulting scattering amplitudes are very close to the MoM-SIE based results. MoM-SIE methods are computationally efficient for electromagnetic problems with small volume to surface ratio and when Green's function can be calculated[4]. FEM-based codes are widely used in computational electromagnetics (in industry), but require discretization of the whole 3 dimensional domain as well as region truncation with boundary condition in order to compute far field scattering results that are easily computed by the SIE method.

5.5 Calculation of radar variables and comparisons with radar measurements

We now consider the rain event which occurred in Huntsville, Alabama on 25 December 2009. This was a wide spread event with an embedded line convection which traversed the disdrometer site (Thurai et al., [143]). The 2DVD measurements for this event showed that a significant fraction of the drops within the line convection (around 30%) did not possess any rotational symmetry axis (i.e., *asymmetric*).

Altogether, 2DVD measurements over a period of 100 minutes were analyzed during which there were 114,317 drops recorded by the instrument, out of which 10,233 drops had $D_{eq} \geq 2$ mm. For all the drops with $D_{eq} \geq 2$ mm, the 3D shapes were constructed in the same way as outlined in Thurai et al. (2017), and their individual scattering amplitudes were calculated using the MoM-SIE method. The individual particle Z_{dr} are plotted as time series in Fig. 5.4 for two values of incident angle. The top two panels show the Z_{dr} for all drops with $D_{eq} \geq 2$ mm for the entire 100-minute period whilst the two lower panels show the same but for the zoomed in time period. In all cases, the drop sizes are color-coded. The variability in Z_{dr} for a given drop size is particularly

[4] See: https://en.wikipedia.org/wiki/Computational_electromagnetics

evident for the large drops (> 4 mm) and further the dependence on the azimuthal angle is also evident. For all drops with D_{eq} < 2 mm, oblate shapes were assumed whose axis ratios were determined using the diameter-dependent relationship given in Eq. (2) of Thurai et al. ([139]). For these drops, the individual scattering amplitudes were also computed with the MoM-SIE. The variability of the single particle Z_{dr} during the line convection passage is evident from Fig. 5.4 (c) though some of the variability is due to sampling errors for the larger sizes which are much lower in concentration. With this consideration the variability in single particle Z_{dr} for a given D_{eq} reflects the variance in shapes due, in part, to the *asymmetric* drops. The coefficient of variation of Z_{dr} (expressed as a ratio) for sizes > 3 mm is around 0.5. The coefficient of variation of the "effective" axis ratio is then ≈ 0.2 using the approximate formula from Jameson [119]. The deduced axis ratio variability is around twice that found by Thurai et al. [140] due to *asymmetric* drops.

From the backscatter amplitudes of each individual drop over a finite time period (1-minute) and drop-by-drop integration of the relevant covariance matrix elements (Bringi and Chandrasekar [111]), the radar reflectivity for horizontal polarization (Z_h), differential reflectivity (Z_{dr}) and copolar correlation coefficient (ρ_{hv}) were computed, for comparisons with the C-band ARMOR radar measurements (see Eqs. 5.3-5.6, later in the text). This method will also be referred to as the MoM-SIE. Note that for K_{dp} calculation the forward scatter amplitudes are used. The finite time period chosen here is 1-minute, since for smaller averaging period, the sampling errors will be large (Schuur et al. [133]) and for larger averaging period, drop sorting errors will also be large (Lee and Zawadzki [124]). Note from Fig. 5.4 (c) and (d) that the line convection passage over the disdrometer site took around 15 minutes, from 03:33 UTC to 03:48 UTC.

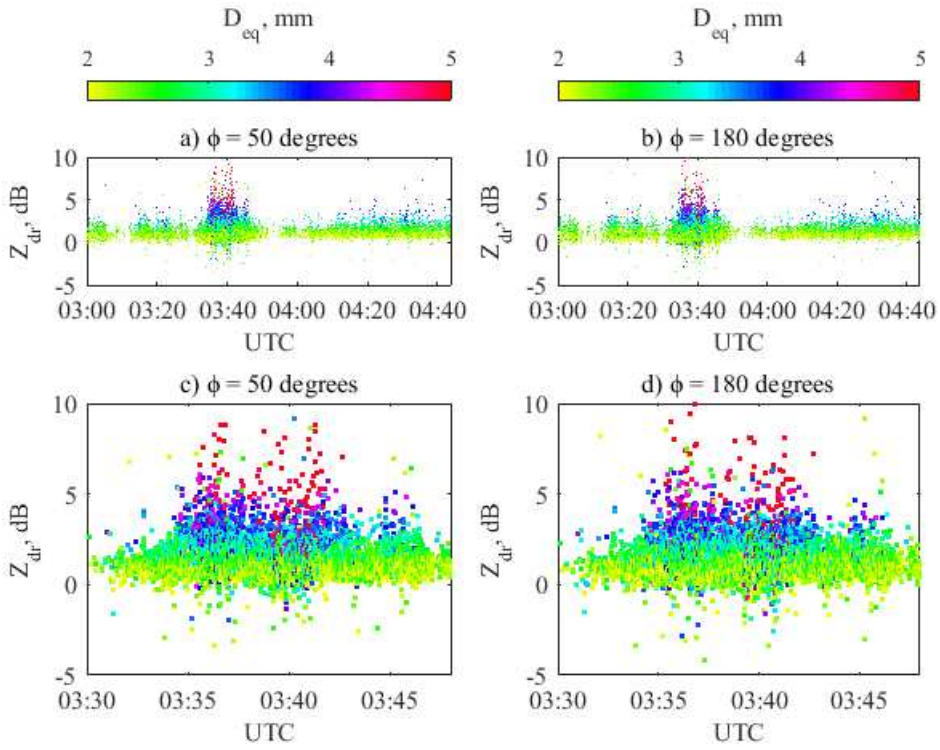

Fig. 5.4. Single particle Z_{dr} for all drops with D_{eq} > 2 mm (a) from 03:00 to 04:40 UTC for ϕ = 50 degrees; (b) the same as (a) but for ϕ = 180 degrees; (c) and (d) are zoomed in versions of (a) and (b) respectively, during the passage of the line convection over the disdrometer site. In all cases, the points are color-coded according to the drop size.

Fig. 5.5 shows the PPI (plan position indicator) scan taken with the ARMOR radar [128] at an elevation angle of 1.3 deg. The time of the scan was 03:40 UTC. The 'star' mark represents the location of the 2DVD, and at this time the line convection was directly positioned over the disdrometer site. Panels (a) and (b) show the copolar reflectivity and the differential reflectivity after correcting for attenuation and differential attenuation, respectively. The correction procedures use the specific differential propagation phase based algorithms, using the same procedure described in Bringi et al. [112]. Reflectivity values were high at the site (> 50 dBZ) and differential reflectivity values were also high (> 4 dB) indicating large drops in the strong precipitation shaft. Other PPI scans taken before and after 03:40 UTC can be seen from Fig. 7 in Thurai et al. [143]. Panel (c) shows the corresponding copolar correlation coefficient, ρ_{hv}, and panel (d) marks the areas within the line convection where ρ_{hv} was less than 0.9. Values of

attenuation-corrected Z_h and Z_{dr} as well as ρ_{hv} were extracted near and around the radar pixels surrounding the 2DVD site (14.5 km radar range, 52.7 degree azimuth) from all the PPI sweeps that were taken from 03:00 to 04:40 UTC. For a given elevation angle, each sweep was repeated at 5-minute time interval.

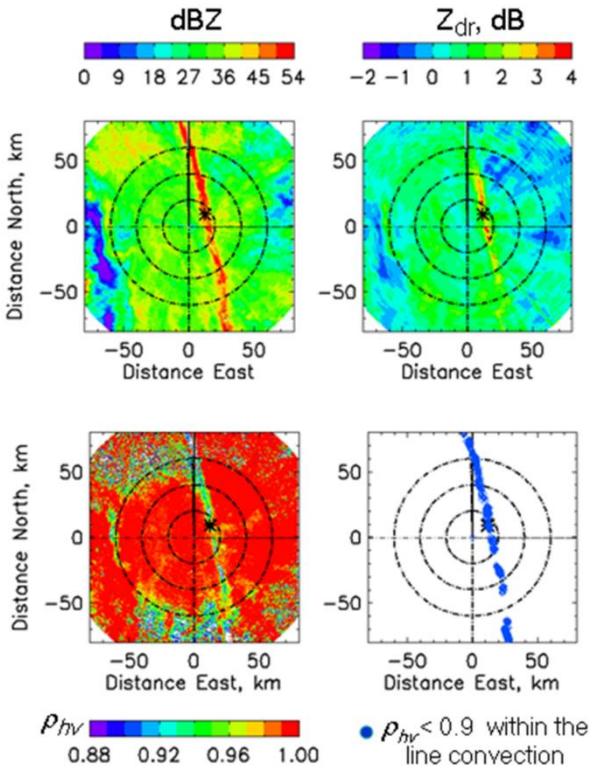

Fig. 5.5. PPI scans of (a) attenuation-corrected Z_h, (b) attenuation-corrected Z_{dr}, and (c) ρ_{hv}, taken at (top to bottom) 03:40 UTC when the line convection was directly above the 2DVD site (marked with an asterisk sign along azimuth 52° and range 15 km). Panel (d) marks the areas within the line convection where ρ_{hv} values were lower than 0.9.

The extracted Z_h and Z_{dr} are shown in Figs. 5.6(a) and 5.6(b), respectively, for the 100-minute period. For a given PPI sweep time, several points are shown which correspond to the '2DVD-pixel' as well as the 'immediate adjacent' pixels in both azimuth and range, covering approximately an area of 750 m by 750 m over the 2DVD site. Altogether 20 PPI sweeps were used over the entire 100-minute period. Reflectivity and differential reflectivity values reach their highest values at 03:40 UTC. Later on, at around 04:30 UTC, reflectivity values again rise but only

up to 40 dBZ. Differential reflectivity remains relatively low, indicating that the maximum drop sizes were significantly lower at 04:30 than at 03:40 UTC. The measured drop size distributions (DSDs) can be seen from Fig. 2(b) in Thurai et al. [143]. At 03:40, the spectra showed the highest mass-weighted mean diameter and the highest standard deviation of the mass spectrum (not shown).

Over-plotted in black in Figs. 5.6(a) and 5.6(b) are the Z_h and Z_{dr} calculations, based on the individual scattering amplitudes of drops (i.e., drop-by-drop integration using MoM-SIE or simply MoM-SIE) over each 1-minute period. The radar measurements of Z_h and Z_{dr} show good temporal correlation and agreement with the MoM-SIE as well as bulk calculations with the radar peak values being somewhat larger (60 dBZ and 4 dB) than the simulations perhaps because of disdrometer sampling limitations for large drops or the applied smoothing. While the agreement between MoM-SIE and bulk methods for Z_h is expected, the agreement of Z_{dr} is somewhat unexpected given the large variance in individual drop Z_{dr} values in the line convection region (see Fig. 5.4(c)) especially for the large drops. The bulk method Z_{dr} is essentially related to the reflectivity-weighted mean axis ratio which would equal the drop-by-drop integrated Z_{dr} if the axis ratio distribution is narrow ([119],[111]). As discussed earlier, the coefficient of variation of the "effective" axis ratio in the line convection is estimated to be around a factor of 2 larger than the value from Thurai et al. [140] which is based on data from an artificial rain experiment where *asymmetric* drops were not detected. In spite of this increase, the axis ratio distribution in the line convection case is judged to be narrow enough that the drop-by-drop MoM-SIE computed Z_{dr} is in good agreement with the bulk method.

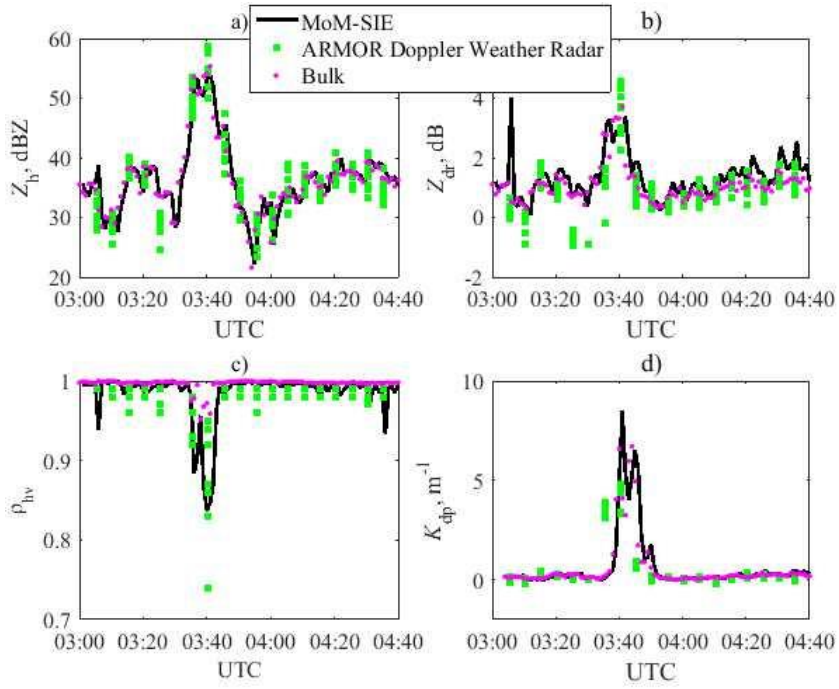

Fig. 5.6. Polarimetric radar variables comparison between MoM-SIE, bulk method, and radar measurements: (a) Reflectivity (Z_h), (b) Differential reflectivity (Z_{dr}), (c) Copolar correlation coefficient (ρ_{hv}), and (d) Specific differential propagation phase (K_{dp}).

Note the radar reflectivity for an individual (i^{th}) drop, in a volume of 1 m^3, is given by:

$$Z_i = 10^{18} \frac{\lambda^4}{\pi^5 |K_w|^2} \eta_i , \tag{5.3}$$

where λ is the wavelength in air, $\eta_{h/v} = 4\pi |S_{hh/vv}|^2$ is back scatter cross section per unit volume for horizontal/vertical (h/v) polarization, $K_w = (\varepsilon_r - 1)(\varepsilon_r + 2)^{-1} = 0.9631 - j0.0111$ is the dielectric factor of water at C-band with dielectric constant $\varepsilon_r = 72.5 - j22.43$. Over a 1-minute period, the resulting reflectivity Z is derived by summing the individual drop reflectivities and is calculated using:

$$Z = \frac{1}{A\Delta t} \sum_i v_i^{-1} Z_i , \tag{5.4}$$

where A is the measurement area of the 2DVD, Δt is the averaging time period, and v_i is the vertical velocity of the i^{th} drop. Equations (5.3) and (5.4) are used to evaluate the overall radar reflectivity based on the individual scattering amplitudes for each of the reconstructed rain drops as well as

their individual measured fall velocities. The computed Z values for h and v polarizations are converted to the conventional dBZ units and the Z_{dr} in dB is obtained from the difference between the two.

Fig. 5.6(c) shows the calculated ρ_{hv} values using:

$$\rho_{hv} = \frac{\left|\sum_i v_i^{-1} S_{hh}^* S_{vv}\right|}{\sqrt{\sum_i v_i^{-1} \left|S_{hh}\right|^2 \sum_i v_i^{-1} \left|S_{vv}\right|^2}}, \tag{5.5}$$

where v_i is the vertical velocity of the i^{th} drop, S represents single drop back-scattering amplitude, and the summation is done over all the drops recorded by the 2DVD during the considered time interval. From 03:35 to 03:40 UTC, a sharp decrease or dip in ρ_{hv} is seen, reaching as low as 0.8. Such low values are consistent with the radar measurement of ρ_{hv} as low as 0.85 in the PPI plot in Fig. 5.5(d). For comparison, C-band scattering calculations using the 1-minute averaged DSDs and bulk assumptions are included in magenta in Fig. 5.6(c). The lowest value using the bulk assumptions is only 0.96. Clearly, the drop-by-drop MoM-SIE based calculations give rise to much more accurate ρ_{hv} predictions than the bulk method. This is due to the inability of the bulk method to capture the variability of drop shapes during the line convection passage. Note however, that at other times, i.e., prior to 03:35 UTC and after 03:45 UTC, both methods predict ρ_{hv} values that are close to 1. These values are consistent with radar measurements over the 2DVD site at these other times. The measurement accuracy of ρ_{hv} is around 1% which is substantially less than the simulated change from 0.96 to 0.8-0.85 so the dip should be detectable if the SNR>20 dB or so (Bringi and Chandrasekar [111]).

Fig. 5.6(d) compares the specific differential propagation phase (K_{dp}) derived from the ARMOR range profiles of differential phase (Φ_{dp}) with the corresponding scattering calculations.

For the radar-based K_{dp} values, the finite impulse response (FIR) range filtering technique is used, as described in Hubbert and Bringi [117], having the advantage of quantifying and removing any backscatter differential phase contribution, which at C-band can become significant when large drops or small melting hail are present in the radar pulse volume. However, close examination of the phase data showed the backscatter differential phase $\delta < 3\text{-}5°$ along the line convection which discounts the presence of small melting hail for which δ could reach 20° (Meischner et al. [125]). For the scattering calculations, as in other panels of Fig. 5.6, the bulk calculations (assuming rotational symmetry) are shown in magenta and the MoM-SIE calculations are shown as black line. K_{dp} is calculated from:

$$K_{dp} = 10^3 \lambda \frac{180}{\pi} \frac{1}{A\Delta t} \sum_i v_i^{-1} \mathrm{Re}\left[S_{hh} - S_{vv}\right], \tag{5.6}$$

where S represents forward scattering amplitudes. The summation is done over all drops recorded in the considered time interval. The bulk calculations are in good agreement with the MoM-SIE calculations which indicates that K_{dp} is not dependent on the variance of shapes, rather it is related to the mass-weighted mean axis ratio ([120][111]). The radar estimate of K_{dp} is smaller than the calculations due to the range filtering and smoothing methodology used across the compact line convection region.

In Thurai et al. [145], the cross-polar backscatter from *asymmetric* drops in terms of single-particle (LDR) was also considered. Here we extend to drop-by-drop MoM-SIE LDR calculations as the ratio of the cross-polar reflectivity to the copolar reflectivity and compare that with the bulk method as shown in Fig. 5.7. It is immediately clear that during the line convection passage, the MoM-SIE method shows much larger LDR than the bulk method (peak of -17 dB versus -26 dB). Even outside the line convection, the MoM-SIE LDR is larger by 3-5 dB relative to the bulk method. We do not have radar data to compare against as the ARMOR radar is not configured for

cross-polar reflectivity measurement. However, it is possible to use an analytical equation relating LDR, Z_{dr}, ρ_{hv}, δ and standard deviation of the canting angle (σ_β) (Jameson [121]) to illustrate the consistency between the dip in ρ_{hv} and the peak in LDR from MoM-SIE calculations during the line convection passage. Using Eq. (3.232) from Bringi and Chandrasekar ([111]) and setting the values of Z_{dr}=3 dB, ρ_{hv}=0.8, δ=5°and σ_β=10° predicts LDR of -19 dB which is consistent with MoM-SIE peak LDR of -17 dB coinciding with dip in ρ_{hv} to 0.82 (close to radar measured dip of 0.8). On the other hand under the same conditions, setting LDR in Eq. (3.232) to the bulk peak value of -26 dB predicts a much larger ρ_{hv}=0.97 (the dip in bulk ρ_{hv} is only to 0.96). Thus, assuming that the radar measured dip in ρ_{hv} to 0.8 is accurate, we can infer that the MoM-SIE calculated LDR peak of -17 dB is more consistent with radar dip in ρ_{hv} than the bulk peak of -25 dB. It follows that the large MoM-SIE LDR values in the line convection are due to enhanced variance in drop shapes due to presence of *asymmetric* drops which cannot be modelled using the bulk method. Over the entire 100-minute event, Table 5.1 shows the relative frequency of occurrence of MoM-SIE and bulk LDR values in 5 dB bins. The modal value (at bin center) of LDR for MoM-SIE and bulk method are, respectively, -37.5 and -32.5 dB with the MoM-SIE showing positive skewness.

TABLE 5.1. Relative frequency of occurrence (in %) of MoM-SIE and bulk LDR values in 5 dB bins computed with drop-by-drop MoM-SIE and bulk T-matrix methods.

Range of LDR, dB	T-matrix	MoM-SIE
< -40	21.3	3.96
-40 to -35	49.2	19.8
-35 to -30	19.7	46.54
-30 to -25	9.8	19.8
-25 to -20	0.0	7.92
-20 to -15	0.0	1.98
-15 to -10	0.0	0
> -10	0.0	0

It should also be noted that because the scattering amplitudes for *asymmetric* drops exhibit ϕ dependence, as we saw earlier in Fig. 5.3, it is necessary to choose the correct ϕ angle, particularly for the Z_{dr} calculations. In our case, the azimuth angle from the radar to the 2DVD site was 52 degrees, and our reconstruction of drops is referenced to the true North (since the 2DVD was aligned in such a way that this criterion was met), hence we chose the same value for ϕ. In Fig. 5.8, we compare the single particle Z_{dr} for ϕ = 50, 110, and 180 degrees. Also shown is the [1:1] line. As seen the correlation is high with negligible bias in both plots and as a result any significant ϕ dependence would not be expected when the overall Z_{dr} is calculated for all drops over a 1-minute integration period.

A limitation of the drop reconstruction procedure is that for a given z = *constant* plane, there are only four points available from the two orthogonal cameras, and the 4-ellipse quarters constructed in this plane can have uncertainties in-between these four points. However, because rain drops do not have sharp discontinuities (unlike snow particles), and further they are homogeneous, the resulting errors in the corresponding scattering calculations are not likely to be significant. Another limitation is that deskewing *asymmetric* drop shapes relies on the accuracy of estimating the horizontal drop speed and direction. In the future we will evaluate if the wind speed and direction measured at the height of the 2DVD sensor area can be used to deskew asymmetric drops.

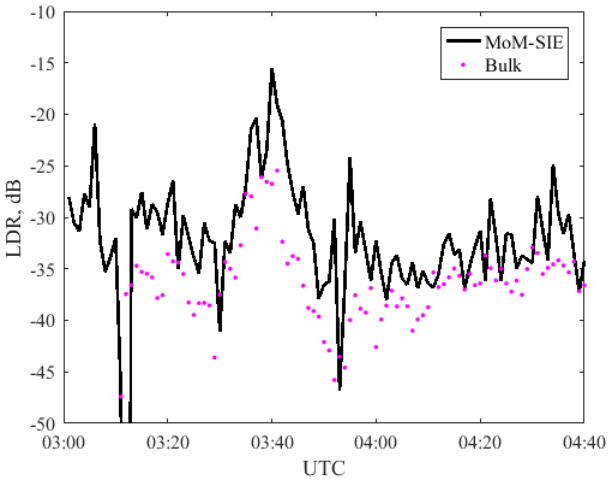

Fig. 5.7. LDR computation for incident ϕ=50^{o} and 1 minute averaging.

Another possible source of errors when comparing disdrometer-based estimates against radar measurements is the different spatial scales of the radar and 'point' 2DVD measurements as well as the height of the radar pulse volume above the surface (340 m in our case). At short ranges considered herein (15 km) the temporal decorrelation between radar and 2DVD is likely to be constrained as evident in Fig. 5.6. It is well-known that surface point measurements cannot be representative of the radar pixel which is often quantified in terms of point-to-area variance ([115],[142]) which depends on the spatial correlation function of the observable used in the comparison. Other sources of errors include radar-measurement errors and disdrometer-sampling errors. However, it is beyond the scope of this paper to quantify the error variances arising from such error sources (we refer to Thurai et al. [142] for variance analysis using ARMOR and 2DVD data).

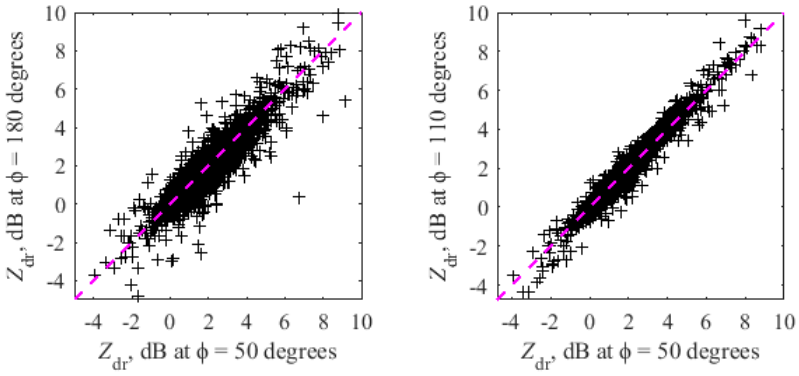

Fig. 5.8. Single particle Z_{dr} comparison for particles with $D_{eq} \geq 2$ mm for ϕ = 50 degrees versus ϕ = 180 degrees (left) and for ϕ = 50 degrees versus ϕ = 110 degrees (right). The purple dashed line represents the [1:1] line.

5.6 Discussion and Conclusions

The bulk method of simulating radar observables such as [Z_h, Z_{dr}, K_{dp}, ρ_{hv}, LDR] in rain involves simplifying assumptions, the main one being related to neglecting the effect of variance in shapes due to presence of *asymmetric drops*, if in fact they occur in significant proportion to the more ubiquitous equilibrium (axisymmetric) shapes. There are very few computations of radar observables that explicitly account for variance in drop shapes. Keat et al. [122] used the data from an artificial rain experiment reported in Thurai and Bringi [138] to simulate steady state axisymmetric drop oscillations (assuming Gaussian axis ratio *pdf*) and its effects on ρ_{hv} and Z_{dr} using gamma distribution of drop sizes (DSD) and Rayleigh-Gans theory. Their goal was to retrieve the shape parameter μ of the gamma DSD from radar measurements of [ρ_{hv}; Z_{dr}]. Their bulk simulations indicated drop oscillations had to be taken into account in order for the radar-based retrieval of μ to be unbiased. Thurai et al. [141] used 2DVD measurements to simulate drop-by-drop scattering but assumed symmetric shapes and canting angles derived from the deskewing procedure as in Huang et al. [118]. The agreement with ARMOR radar measurements was good but they found significant differences in Z_{dr} and ρ_{hv} when compared with bulk methods in one convective rain event.

To the best of our knowledge this study is the first polarimetric scattering analysis of a line convection rain event based on drop-by-drop scattering computations by means of a higher order method of moments in a surface integral equation formulation, with *asymmetric* drop geometries being reconstructed from 2DVD measurements. We have compared MoM-SIE surface model discretization results for an example asymmetric drop with equi-volume drop diameter D_{eq}=4.81 mm (in Fig. 5.1) at S, C, and X bands with volumetric discretization results by an industry standard finite element method based code (HFSS), showing excellent agreement between two methods. The single particle Z_{dr} values showed variability during the passage of the line convection over the 2DVD site with coefficient of variation (when Z_{dr} is expressed as a ratio) of around 0.5 (for drops > 3 mm) which confirms that the variance of drop shapes due to asymmetric drops can be an important factor in this particular case. Note that before and after passage of the line convection the shape variability was sharply reduced.

Drop-by-drop scattering calculations based on 1-minute integration of the covariance matrix elements were performed for the 100-minute event passage over the 2DVD site using the MoM-SIE and the bulk methods. The simulated radar observables were compared with ARMOR radar data extracted from range gates surrounding the 2DVD location. The Z_h, Z_{dr} and K_{dp} were found to be in good agreement between the MoM-SIE, the bulk calculations and the extracted ARMOR data during the line convection passage as well as before and after the passage. However, the bulk method could not simulate the significant lowering of ρ_{hv} during the line convection with dip to 0.8 as measured by radar. The MoM-SIE calculations were able to simulate the dip to 0.8 indicating that the lowered values were a result of variance in shapes due to asymmetric drops. The radar differential phase data showed no evidence of backscatter differential phase (estimated

$\delta < 3\text{-}5°$) within the line convection and neither did the single drop MoM-SIE calculations ($\delta < 5°$), so this effect could not have contributed to the lowering of ρ_{hv}.

We also computed LDR using drop-by-drop MoM-SIE and the bulk method. During the line convection passage over the 2DVD the MoM-SIE LDR values peaked to -17 dB whereas the bulk LDR was around 8 dB lower (-25 dB). Examination of an analytic expression relating the polarimetric variables showed that the MoM-SIE LDR peak of -17 dB was consistent with the dip in ρ_{hv} to 0.8 (the latter in agreement with the radar observed dip). However, the bulk LDR of -25 dB was not consistent with the observed ρ_{hv} dip, the analytic expression giving a much higher ρ_{hv} value of 0.97 consistent with the calculated bulk value of 0.96. Since the ARMOR radar was not configured for LDR measurements we could not compare with the simulated values. Over the full 100-minute event the modal MoM-SIE LDR values were around -32 .5 dB whereas it was around -37.5 dB for the bulk method. Radars with modest dual-polarized antenna with a system LDR limit of -25 dB (e.g., phased-array airborne radars) could easily detect the LDR peak of -17 dB. However, to detect LDR of -32.5 dB a well-designed antenna capable of system LDR limit of -36 dB would be required (the UK C-band operational radars approach the -36 dB system limit and they routinely measure LDR to detect wet snow aloft; Sandford et al. [129]).

As has been mentioned in earlier publications (Thurai et al., [143],[144]), 2DVD data examined during most of the rain events showed that the drop shapes conform to the 'most probable' shapes arising from the steady state axisymmetric oscillation mode which can be regarded as the background state. *Asymmetric* shapes occur when the background state is perturbed due to transverse or horizontal modes mixed in which is termed as mixed-mode oscillations (Beard et al. [109]). The line convection system considered here is one of the few exceptions where a significant proportion (≈30%) of *asymmetric* drops was only detected within the line convection

but not outside it. Currently, there is no theoretical framework to identify the conditions under which mixed mode oscillations may occur in a persistent manner. For now we have to rely on 2DVD data to first detect the presence of a significant proportion of asymmetric drops in the rain shaft and subsequently to evaluate the conditions under which deviations from the 'most probable' axisymmetric drop shapes occur. Based on this study the most impact would be on quantitative use of ρ_{hv} and LDR with much less impact on Z_{dr} and negligible impact on Z_h and K_{dp}.

CONCLUSION

Double Higher Order methods using model subdivision to decrease the memory needed for electromagnetic modeling analysis in order to simulate large structures on a personal computer are presented. The discretization types are both volumetric, in conjunction with Finite Element Method (FEM), and surface, used to model surface encompassing the structure analyzed by means of Surface Integral Equation Method of Moments (SIE-MoM). Lagrange type higher order basis functions model the unknown for both methods, curl conforming functions in FEM and divergence conforming functions in SIE-MoM, enabling the element size to be of the order of the wavelength.

Model subdivision is applied to closed-region (waveguide) structure FEM model computing electric field vector as the unknown. The waveguide structure is divided into subdomains, i.e. smaller sized waveguide structures, which are separately analyzed decreasing the memory consumption. Generalized Scattering Matrix (GSM) is computed for each subdomain by the means of Mode Matching (MM) technique, which is enabled by 2-D FEM iterative eigenvalue solver developed to compute modal patterns existing at the waveguide ports. Original structure is unified by connecting the subdomains via their ports. The response of the original (large) structure is obtained by concatenating computed GSMs into the large matrix connecting all outgoing modes existing on the ports of all subdomains to the all ingoing modes. The benefits of large domain modeling and inclusion of higher modes in design process are presented. The method is applied to computation of the received power in communication system in Massif Central tunnel showing benefits of accurately modeling the geometry, especially in the vicinity of the tunnel walls.

Model subdivision is applied to open-region SIE models computing fictitious surface currents as the unknown. Octree grid is used to decompose the model and the solution is obtained by the iterative solver. The matrix entries computed for groups of elements in the proximity are

obtained by SIE-MoM computation. The interaction between the groups in the far field zone are analyzed by Fast Multipole Method (FMM) never computing the actual matrix entries but the matrix vector multiplication (MVM) in the iterative solver implementation. This process decreases both memory storage and time consumption of the computer simulation. Multi-Level version of FMM uses multi-level Octree grid to compute MVMs through multi-level interaction scheme of the decomposed model groups decreasing the complexity and memory even further. The method was verified but the measurement of the simulation acceleration and memory decrease is part of the future work.

In order to precisely evaluate elements in SIE-MoM matrix entries computation, novel extraction method for near-field 2-D surface integrals is developed taking into account higher order definition of the basis function and curvature of the quadrilateral element. This is done by incorporating quadrilateral curvature into parallelogram definition and developing analytical integration formulas to include higher order basis functions in order to mitigate the singularity occurring in 2-D integrals [42]. The improved precision of the integral computation over the traditional technique is observed even in the cases not reported previously. SIE - MoM technique was applied to line convection event with rain drops recorded by 2-D video disdrometer. The SIE elements discretizing the model's surface are described by the nodes obtained after the reconstruction is performed on the 2-D video disdrometer measurements. Scattering calculations of radar variables computed by the SIE-MoM show improvement over the traditional (bulk) modeling when comparing results to the radar measurements, for the event containing significant percentage of the oscillating drops.

REFERENCES

[1] J.-M. Jin, *Theory and Computation of Electromagnetic Fields*. Hoboken, NJ: Wiley, 2010.

[2] R. F. Harrington, *Field Computation by Moment Methods*. New York: Macmillan, 1968.

[3] S. M. Rao, C. C. Cha, R. L. Cravey and D. L. Wilkes, "Electromagnetic scattering from arbitrary shaped conducting bodies coated with lossy materials of arbitrary thickness", in *IEEE Transactions on Antennas and Propagation*, vol. 39, no. 5, pp.627-631, May 1991.

[4] M. Analoui and Y. Kagawa, "Electromagnetic scattering from conductor-coated material bodies", in *International Journal of Numerical Modelling: Electronic Networks, Devices and Fields*, vol.4, no. 4, pp. 287-299, December 1991.

[5] S. M. Rao, T. K. Sarkar, P. Midya and A. R. Djordjevic, "Electromagnetic radiation and scattering from finite conducting and dielectric structures: surface/surface formulation", in *IEEE Transactions on Antennas and Propagation*, vol. 39, no. 7, pp. 1034–1037, July 1991.

[6] S. Wandzura, "Electric-current basis functions for curved surfaces," in *Electromagnetics*, vol. 12, no. 1, pp. 77–91, 1992.

[7] J. M. Song and W. C. Chew, "Moment Method Solutions Using Parametric Geometry", in *Journal of Electromagnetic Waves and Applications*, vol. 9, no. 1/2, pp. 71-83, January-February 1995.

[8] R. D. Graglia, D. R. Wilton and A. F. Peterson, "Higher Order Interpolatory Vector Bases for Computational Electromagnetics", in *IEEE Transactions on Antennas and Propagation*, vol. 45, no. 3, pp. 329-342, March 1997.

[9] G. Kang, J. Song, W. C. Chew, K. C. Donepudi and J. M. Jin, "A Novel Grid-Robust Higher Order Vector Basis Function for the Method of Moments", in *IEEE Transactions on Antennas and Propagation*, vol. 49, no. 6, pp 908-915, June 2001.

[10] R. D. Graglia, "The use of parametric elements in the moment method solution of static and dynamic volume integral equations," in *IEEE Transactions on Antennas and Propagation*, vol. 36, no. 5, pp. 636-646, May 1988.

[11] M. Djordjević and B. M. Notaroš, "Higher-Order Hierarchical Basis Functions with Improved Orthogonality Properties for Moment-Method Modeling of Metallic and Dielectric Microwave Structures", in *Microwave and Optical Technology Letters*, vol. 37, no. 2, pp. 83-88, April 2003.

[12] M. Djordjević and B. Notaroš, "Double Higher Order Method of Moments for Surface Integral Equation Modeling of Metallic and Dielectric Antennas and Scatterers", in *IEEE Transactions on Antennas and Propagation*, vol. 52, no. 8, pp. 2118-2129, August 2004.

[13] D. Schaubert, D. Wilton and A. Glisson, "A tetrahedral modeling method for electromagnetic scattering by arbitrarily shaped inhomogeneous dielectric bodies," in *IEEE Transactions on Antennas and Propagation*, vol. 32, no. 1, pp. 77-85, January 1984.

[14] T. K. Sarkar, E. Arvas and S. Ponnapalli, "Electromagnetic scattering from dielectric bodies," in *IEEE Transactions on Antennas and Propagation*, vol. 37, no. 5, pp. 673-676, May 1989.

[15] B. J. Rubin and S. Daijavad, "Radiation and scattering from structures involving finite-size dielectric regions," in *IEEE Transactions on Antennas and Propagation*, vol. 38, no. 11, pp. 1863-1873, November 1990.

[16] P. De Doncker, "A Potential Integral Equations Method for Electromagnetic Scattering by Penetrable Bodies," in *IEEE Transactions on Antennas and Propagation*, vol. 49, no. 7, pp. 1037-1042, July 2001.

[17] K. Sertel and J. L. Volakis, "Method of moments solution of volume integral equations using parametric geometry modeling," in *Radio Science*, vol. 37, no. 1, pp. 1-7, January 2002.

[18] O. S. Kim, P. Meincke, O. Breinbjerg and E. Jørgensen, "Method of moments solution of volume integral equations using higher-order hierarchical Legendre basis functions," in *Radio Science*, vol. 39, no. 5, RS5003, pp. 1-7, September 2004.

[19] M. M. Botha, "Solving the volume integral equations of electromagnetic scattering," in *Journal of Computational Physics*, vol. 218, no. 1, pp. 141-158, 2006.

[20] R. D. Graglia and A. F. Peterson, "Hierarchical divergence-conforming Nédélec elements for volumetric cells," in *IEEE Transactions on Antennas and Propagation*, vol. 60, no. 11, pp. 5215-5227, November 2012.

[21] B. M. Notaroš and B. D. Popović, "Large-domain integral-equation method for analysis of general 3-D electromagnetic structures," in *IEE Proceedings - Microwaves, Antennas and Propagation*, vol. 145, no. 6, pp.491-495, December 1998.

[22] E. Chobanyan, M. M. Ilić and B. Notaroš, "Double-Higher-Order Large-Domain Volume/Surface Integral Equation Method for Analysis of Composite Wire-Plate-Dielectric Antennas and Scatterers", in *IEEE Transactions on Antennas and Propagation*, vol. 61, no. 12, pp. 6051-6063, December 2013.

[23] N. Engheta, W. D. Murphy, V. Rokhlin and M. S. Vassiliou, "The Fast Multipole Method (FMM) for Electromagnetic Scattering Problem", in *IEEE Transactions on Antennas and Propagation*, vol. 40, no. 6, pp. 634-641, June 1992.

[24] V. Rokhlin, "Diagonal Forms of Translation Operators for the Helmholtz Equation in Three Dimensions", in *Applied and Computational Harmonic Analysis*, vol. 1, no. 1, pp. 82-93, February 1993.

[25] R. Coifman, V. Rokhlin and S. Wandzura, "The Fast Multipole Method for the Wave Equation: A Pedestrian Prescription", in *IEEE Antennas and Propagation Magazine*, vol. 35, no.3, pp. 7-12, June 1993.

[26] S. Wang, Y. Su and X. Guan, "Applying Fast Multipole Method to Higher-Order Hierarchical Legendre Basis Functions in Electromagnetic Scattering", in *IET Microwaves, Antennas & Propagation*, vol. 2, no. 1, pp. 6-9, February 2008.

[27] S. Velamparambil, W. C. Chew and J. Song, "10 Million Unknowns: Is It That Big?" in *IEEE Antennas and Propagation Magazine*, vol. 45, no. 2, pp. 43-58, April 2003.

[28] O. Ergul, T. Malas and L. Gurel, "Solutions of Large-Scale Electromagnetics Problems Using an Iterative Inner-Outer Scheme with Ordinary and Approximate Multilevel Fast Multipole Algorithms", in *Progress in Electromagnetics Research*, vol. 106, no. 1, pp. 203–223, July 2010.

[29] O. Ergul and L. Gurel, "Rigorous Solutions of Electromagnetic Problems Involving Hundreds of Millions of Unknowns", in *IEEE Antennas and Propagation Magazine*, vol. 53, no.1, pp. 18-27, February 2011.

[30] O. Ergul and L. Gurel, "Accurate Solutions of Extremely Large Integral-Equation Problems in Computational Electromagnetics", in *IEEE Proceedings*, vol. 101, no. 2, pp. 342-349, February 2013.

[31] X. Q. Sheng, J.-M. Jin, J. Song, W. C. Chew and C.-C. Lu, "Solution of Combined-Field Integral Equation Using Multilevel Fast Multipole Algorithm for Scattering by Homogeneous Bodies", in *IEEE Transactions on Antennas and Propagation*, vol. 46, no. 11, pp. 1718-1726, November 1998.

[32] X.-M. Pan, J.-G. Wei, Z. Peng and X.-Q. Sheng, "A Fast Algorithm for Multiscale Electromagnetic Problems Using Interpolative Decomposition and Multilevel Fast Multipole Algorithm", in *Radio Science*, vol. 47, RS1011, pp. 1-11, February 2012.

[33] O. Borries, P. Meincke, E. Jørgensen and P. C. Hansen, "Multilevel Fast Multipole Method for Higher Order Discretizations", in *IEEE Transactions on Antennas and Propagation*, vol. 62, no. 9, pp. 4695-4705, September 2014.

[34] K. C. Donepudi, J.-M. Jin, S. Velamparambil, J. Song and W. C. Chew, "A Higher Order Parallelized Multilevel Fast Multipole Algorithm for 3-D Scattering", in *IEEE Transactions on Antennas and Propagation*, vol. 49, no. 7, pp. 1069-1078, July 2001.

[35] J. Song, C.-C. Lu and W. C. Chew, "Multilevel Fast Multipole Algorithm for Electromagnetic Scattering by Large Complex Objects", in *IEEE Transactions on Antennas and Propagation*, vol. 45, no. 10, pp. 1488-1493, October 1997.

[36] O. Borries, E. Jorgensen, P. Meincke and P. C. Hansen, "Adaptive Grouping for the Higher-Order Multilevel Fast Multipole Methods", in *Microwave and Optical Technology Letters*, vol. 56, no. 10, pp. 2451-2456, October 2014.

[37] K. Sertel, "Multilevel Fast Multipole Method for Modeling Permeable Structures Using Conformal Finite Elements", *Ph.D. Dissertation*, University of Michigan, Department of Electrical Engineering, Ann Arbor, Michigan, 2003.

[38] X.-M. Pan, L. Cai and X.-Q. Sheng, "An Efficient High Order Multilevel Fast Multipole Algorithm for Electromagnetic Scattering Analysis", in *Progress in Electromagnetics Research*, vol. 126, pp. 85-100, March 2012.

[39] D. Dault and B. Shanker, "A Mixed Potential MLFMA for Higher Order Moment Methods with Application to the Generalized Method of Moments", in *IEEE Transactions on Antennas and Propagation*, vol. 64, no. 2, pp. 650-662, February 2016.

[40] Ismatullah and T. F. Eibert, "Surface Integral Equation Solutions by Hierarchical Vector Basis Functions and Spherical Harmonics Based Multilevel Fast Multipole Method", in *IEEE Transactions on Antennas and Propagation*, vol. 57, no. 7, pp. 2084-2093, July 2009.

[41] S. Jarvenpaa, M. Taskinen and P. Yla-Oijala, "Singularity subtraction technique for high-order polynomial vector basis functions on planar triangles," in *IEEE Transactions on Antennas and Propagation*, vol. 54, no. 1, pp. 42-49, January 2006.

[42] A. Manić, “Fast and Accurate Double-Higher-Order Method of Moments Accelerated by Diakoptics Domain Decomposition and Memory Efficient Parallelization for High Performance Computing Systems.” *Ph.D. Dissertation*, Colorado State University, Department of Electrical and Computer Engineering, Fort Collins, Colorado, 2015.

[43] M. M. Botha, "Numerical Integration Scheme for the Near-Singular Green Function Gradient on General Triangles," in IEEE Transactions on Antennas and Propagation, vol. 63, no. 10, pp. 4435-4445, October 2015.

[44] M. M. Botha, “A single domain approach to weak near-singularity cancellation quadrature on triangle domains,” 2016 10th European Conference on Antennas and Propagation (EuCAP), Davos, 2016, pp. 1-4. doi: 10.1109/EuCAP.2016.7481684, 2016

[45] P. W. Fink, D. R. Wilton and M. A. Khayat, “Simple and Efficient Numerical Evaluation of Near-Hypersingular Integrals,” in IEEE Antennas and Wireless Propagation Letters, vol. 7, pp. 469-472, 2008.

[46] A. A. Tambova, M. S. Litsarev, G. Guryev and A. G. Polimeridis, “On the Generalization of DIRECTFN for Singular Integrals Over Quadrilateral Patches,” in IEEE Transactions on Antennas and Propagation, vol. 66, no. 1, pp. 304-314, January 2018.

[47] D. R. Wilton, F. Vipiana and W. A. Johnson, “Evaluation of 4-D Reaction Integrals in the Method of Moments: Coplanar Element Case,” in *IEEE Transactions on Antennas and Propagation*, vol. 65, no. 5, pp. 2479-2493, May 2017.

[48] A. Konyukhov and K. Schweizerhof, “On the solvability of closest point projection procedures in contact analysis: Analysis and solution strategy for surfaces of arbitrary geometry”, in *Comput. Methods Appl. Mech. Engrg.*, vol. 197, pp. 3045-3056, June 2008.

[49] Y. Saad, *Iterative Methods for Sparse Linear Systems*. 2nd edition, Philadelphia: SIAM, 2003.

[50] D. Meagher, “Geometric modeling using octree encoding,” in *Comput. Graphics Image Process.*, vol. 19, no. 2, pp. 129-147, Jun. 1982.

[51] O. Ergul, I. van den Bosch and L. Gurel, “Two-Step Lagrange Interpolation Method for the Multilevel Fast Multipole Algorithm,” in *IEEE Antennas and Wireless Propagation Letters*, vol. 8, pp. 69-71, 2009.

[52] M. Kostić and B. Kolundzija, “Maximally orthogonalized higher order bases over generalized wires, quadrilaterals, and hexahedra,” in *IEEE Transactions on Antennas and Propagation*, vol. 61, no. 6, pp. 3135-3148, June 2013.

[53] P. P. Silvester and R. L. Ferrari, *Finite Elements for Electrical Engineers*. Cambridge, U.K.: Cambridge University Press, 1996.

[54] M. Hano, "Finite-Element Analysis of Dielectric-Loaded Waveguides," in *IEEE Transactions on Microwave Theory and Techniques*, vol. 32, no. 10, pp. 1275-1279, October 1984.

[55] J. F. Lee, D. K. Sun and Z. J. Cendes, “Full-Wave Analysis of Dielectric Waveguides Using Tangential Vector Finite Elements,” in *IEEE Transactions on Microwave Theory and Techniques*, vol. 39, no. 8, pp. 1262-1271, August 1991.

[56] J. F. Lee, "Finite Element Analysis of Lossy Dielectric Waveguides," in *IEEE Transactions on Microwave Theory and Techniques*, vol. 42, no. 6, pp. 1025-1031, June 1994.

[57] S. V. Polstyanko, R. Dyczij-Edlinger and J. F. Lee, "Fast Frequency Sweep Technique for the Efficient Analysis of Dielectric Waveguides," in *IEEE Transactions on Microwave Theory and Techniques*, vol. 45, no. 7, pp. 1118-1125, July 1997.

[58] R. Miniowitz and J. P. Webb, "Covariant-Projection Quadrilateral Elements for the Analysis of Waveguides with Sharp Edges," in *IEEE Transactions on Microwave Theory and Techniques*, vol. 39, no. 3, pp. 501-505, March 1991.

[59] B. M. Dillon and J. P. Webb, "A Comparison of Formulations for the Vector Finite Element Analysis of Waveguides," in *IEEE Transactions on Microwave Theory and Techniques*, vol. 42, no. 2, pp. 308-316, February 1994.

[60] D. K. Sun and Z. Cendes, "Fast High-Order FEM Solutions of Dielectric Wave Guiding Structures," in *IEE Proceedings: Microwaves, Antennas and Propagation*, vol. 150, no. 4, pp. 230-236, August 2003.

[61] S. C. Lee, J. F. Lee and R. Lee, "Hierarchical Vector Finite Elements for Analyzing Waveguiding Structures," in *IEEE Transactions on Microwave Theory and Techniques*, vol. 51, no. 8, pp. 1897-1905, August 2003.

[62] M. M. Ilić, A. Z. Ilić, and B. M. Notaroš, "Efficient Large-Domain 2-D FEM Solution of Arbitrary Waveguides Using p-Refinement on Generalized Quadrilaterals," in *IEEE Transactions on Microwave Theory and Techniques*, vol. 53, no. 4, pp.1377-1383, April 2005.

[63] L. S. Andersen and J. L. Volakis, "Development and application of a novel class of hierarchical tangential vector finite elements for electromagnetics," in *IEEE Transactions on Antennas and Propagation*, vol. 47, no. 1, pp. 112-120, January 1999.

[64] D. T. Nguyen, C. F. Bunting, K. J. Moeller, H. Runesha, and J. Qin, "Subspace and Lanczos sparse eigen-solvers for finite element structural and electromagnetic applications", in *Advances in Engineering Software*, vol. 31, pp. 599-606, August 2000.

[65] Y. Saad, *Iterative Methods for Sparse Linear Systems*. Boston: PWS Publishing, 1996.

[66] Z. Bai, J. Demmel, J. Dongarra, A. Ruhe and H. van der Vorst, *Templates for the Solution of Algebraic Eigenvalue Problems: a Practical Guide*, Philadelphia: SIAM, pp. 56-66, 2000.

[67] M. M. Ilić, A. Z. Ilić and B. M. Notaroš, "Continuously Inhomogeneous Higher Order Finite Elements for 3-D Electromagnetic Analysis," in *IEEE Transactions on Antennas and Propagations*, vol. 57, no. 9, pp. 2798-2803, September 2009.

[68] M. M. Ilić and B. M. Notaroš, "Higher Order Large-Domain Hierarchical FEM Technique for Electromagnetic Modeling Using Legendre Basis Functions on Generalized Hexahedra," in *Electromagnetics*, vol. 26, no. 7, pp. 517-529, October 2006.

[69] M. M. Ilić, A. Z. Ilić and B. M. Notaroš, "Higher Order Large-Domain FEM Modeling of 3-D Multiport Waveguide Structures with Arbitrary Discontinuities," in *IEEE Transactions on Microwave Theory and Techniques*, vol. 52, no. 6, pp.1608-1614, June 2004.

[70] M. M. Ilić and B. M. Notaroš, "Higher order hierarchical curved hexahedral vector finite elements for electromagnetic modeling," in *IEEE Transactions on Microwave Theory and Techniques*, vol. 51, no. 3, pp.1026-1033, March 2003.

[71] J. Rubio, J. Arroyo and J. Zapata, "Analysis of Passive Microwave Circuits by Using a Hybrid 2-D and 3-D Finite-Element Mode-Matching Method," in *IEEE Transactions on Microwave Theory and Techniques*, vol. 47, no. 9, pp. 1746-1749, September 1999.

[72] Z. Lou and J. M. Jin, "An accurate waveguide port boundary condition for the time-domain finite element method," in *IEEE Trans. Microwave Theory Tech*., vol. 53, no. 9, pp. 3014-3023, September 2005.

[73] E. M. Klopf, S. B. Manić, M. M. Ilić and B. M. Notaroš, "Efficient Time-Domain Analysis of Waveguide Discontinuities Using Higher Order FEM in Frequency Domain," in *Progress In Electromagnetics Research*, vol. 120, pp. 215-234, 2011.

[74] R. Sorrentino, "Planar circuits, waveguide models, and segmentation method," in *IEEE Trans. Microwave Theory Tech*., vol. MTT-33, no. 10, pp. 1057–1066, October 1985.

[75] J. Rubio, J. Arroyo and J. Zapata, "SFELP-an efficient methodology for microwave circuit analysis," in IEEE Transactions on Microwave Theory and Techniques, vol. 49, no. 3, pp. 509-516, March 2001.

[76] J. Rubio, M. A. Gonzalez and J. Zapata, "Analysis of cavity-backed microstrip antennas by a 3-D finite element/segmentation method and a matrix Lanczos-Pade algorithm (SFELP)," in *IEEE Antennas and Wireless Propagation Letters*, vol. 1, pp. 193-195, 2002.

[77] J. Rubio, M. A. Gonzalez and J. Zapata, "Generalized-scattering-matrix analysis of a class of finite arrays of coupled antennas by using 3-D FEM and spherical mode expansion," in *IEEE Transactions on Antennas and Propagation*, vol. 53, no. 3, pp. 1133-1144, March 2005.

[78] Jose Ma Gil, Javier Monge, J. Rubio and J. Zapata, "A CAD-oriented method to analyze and design radiating structures based on bodies of revolution by using finite elements and generalized scattering matrix," in *IEEE Transactions on Antennas and Propagation*, vol. 54, no. 3, pp. 899-907, March 2006.

[79] V. de la Rubia and J. Zapata, "Microwave Circuit Design by Means of Direct Decomposition in the Finite-Element Method," in *IEEE Transactions on Microwave Theory and Techniques*, vol. 55, no. 7, pp. 1520-1530, July 2007.

[80] V. de la Rubia and J. Zapata, "MAM—A Multipurpose Admittance Matrix for Antenna Design Via the Finite Element Method," in *IEEE Transactions on Antennas and Propagation*, vol. 55, no. 8, pp. 2276-2286, August 2007.

[81] V. de la Rubia, J. Zapata and M. A. Gonzalez, "Finite Element Analysis of Periodic Structures Without Constrained Meshes," in *IEEE Transactions on Antennas and Propagation*, vol. 56, no. 9, pp. 3020-3028, September 2008.

[82] J. Martinez-Fernandez, V. de la Rubia, J. M. Gil and J. Zapata, "Frequency Notched UWB Planar Monopole Antenna Optimization Using a Finite Element Method-Based Approach," in *IEEE Transactions on Antennas and Propagation*, vol. 56, no. 9, pp. 2884-2893, September 2008.

[83] B. El Jaafari, M. A. G. de Aza and J. Zapata, “An Approach Based on Finite Element Method for CAD of Printed Antennas,” in *IEEE Transactions on Antennas and Propagation*, vol. 11, pp. 1238-1241, 2012.

[84] V. de la Rubia, U. Razafison and Y. Maday, “Reliable Fast Frequency Sweep for Microwave Devices via the Reduced-Basis Method,” in *IEEE Transactions on Microwave Theory and Techniques*, vol. 57, no. 12, pp. 2923-2937, December 2009.

[85] J. Corcoles, M. A. Gonzalez and J. Rubio, “Multiobjective Optimization of Real and Coupled Antenna Array Excitations via Primal-Dual, Interior Point Filter Method From Spherical Mode Expansions,” in *IEEE Transactions on Antennas and Propagation*, vol. 57, no. 1, pp. 110-121, January 2009.

[86] J. Rubio, J. Corcoles and M. Gonzalez de Aza, "Inclusion of the Feeding Network Effects in the Generalized-Scattering-Matrix Formulation of a Finite Array," in *IEEE Antennas and Wireless Propagation Letters*, vol. 8, pp. 819-822, 2009.

[87] E. Martini, G. Pelosi and S. Selleri, “ Hybrid finite-element-modal-expansion method with a new type of curvilinear mapping for the analysis of microwave passive devices,” in *IEEE Transactions on Microwave Theory and Techniques*, vol. 51, no. 6, pp. 1712- 1717, June 2003.

[88] R. D. Graglia, D. R. Wilton and A. F. Peterson, “Higher order interpolatory vector bases for computational electromagnetics,” in *IEEE Transactions on Antennas and Propagation*, vol. 45, no. 3, pp. 329-342, March 1997.

[89] T. Cavanna, E. Franzese, E. Limiti, G. Pelosi, S. Selleri and A. Suriani, “Coplanar-to-rectangular waveguide millimeter-wave transitions manufacturing tolerance analysis using the finite-element method,” in *Int J RF and Microwave Comp Aid Eng*, vol. 16, pp. 118–124, 2006.

[90] G. Guarnieri, G. Pelosi, L. Rossi and S. Selleri, “A domain decomposition technique for finite element based parametric sweep and tolerance analyses of microwave passive devices,” in *Int J RF and Microwave Comp Aid Eng*, vol.19, pp. 328–337, 2009.

[91] E. Martini, G. Carli and S. Maci, “A domain decomposition method based on a generalized scattering matrix formalism and a complex source expansion,” in *Progress In Electromagnetics Research B*, vol. 19, pp. 445-473, 2010.

[92] A. Barka, P. Soudais and D. Volpert, “Scattering from 3-D cavities with a plug and play numerical scheme combining IE, PDE, and modal techniques,” in *IEEE Transactions on Antennas and Propagation*, vol. 48, no. 5, pp. 704-712, May 2000.

[93] A. Barka, P. Caudrillier, “Domain Decomposition Method Based on Generalized Scattering Matrix for Installed Performance of Antennas on Aircraft,” in *IEEE Transactions on Antennas and Propagation*, vol. 55, no. 6, pp. 1833-1842, June 2007.

[94] R. Chiniard, A. Barka and O. Pascal, “Hybrid FEM/Floquet Modes/PO Technique for Multi-Incidence RCS Prediction of Array Antennas,” in *IEEE Transactions on Antennas and Propagation*, vol. 56, no. 6, pp. 1679-1686, June 2008.

[95] A. Barka and N. Douchin, “Asymptotic simplifications for hybrid BEM/GO/PO/PTD techniques based on a Generalized Scattering Matrix approach,” in *Computer Physics Communications*, vol. 183, no. 9, pp. 1928-1936, September 2012.

[96] R. Beyer and F. Arndt, "Efficient modal analysis of waveguide filters including the orthogonal mode coupling elements by an MM/FE method," in *IEEE Microwave and Guided Wave Letters*, vol. 5, no. 1, pp. 9-11, January 1995.

[97] J. M. Reiter and F. Arndt, "Rigorous analysis of arbitrarily shaped H- and E-plane discontinuities in rectangular waveguides by a full-wave boundary contour mode-matching method," in *IEEE Transactions on Microwave Theory and Techniques*, vol. 43, no. 4, pp. 796-801, April 1995.

[98] F. Arndt, R. Beyer, J. M. Reiter, T. Sieverding and T. Wolf, "Automated design of waveguide components using hybrid mode-matching/numerical EM building-blocks in optimization-oriented CAD frameworks-state of the art and recent advances," in *IEEE Transactions on Microwave Theory and Techniques*, vol. 45, no. 5, pp. 747-760, May 1997.

[99] F. Arndt, J. Brandt, V. Catina, J. Ritter, I. Rullhusen, J. Dauelsberg, U. Hilgefort and W. Wessel, "Fast CAD and optimization of waveguide components and aperture antennas by hybrid MM/FE/MoM/FD methods-state-of-the-art and recent advances," in *IEEE Transactions on Microwave Theory and Techniques*, vol. 52, no. 1, pp. 292-305, January 2004.

[100] V. Catina, F Arndt and J. Brandt, "Hybrid surface integral-equation/mode-matching method for the analysis of dielectric loaded waveguide filters of arbitrary shape," in *IEEE Transactions on Microwave Theory and Techniques*, vol. 53, no. 11, pp. 3562- 3567, November 2005.

[101] S. C. Lee, J. F. Lee and R. Lee, "Hierarchical vector finite elements for analyzing waveguiding structures," in *IEEE Transactions on Microwave Theory and Techniques*, vol. 51, no. 8, pp. 1897- 1905, August 2003.

[102] A. Kusiek, R. Lech and J. Mazur, "A New Hybrid Method for Analysis of Scattering From Arbitrary Configuration of Cylindrical Objects," in *IEEE Transactions on Antennas and Propagation*, vol. 56, no. 6, pp. 1725-1733, June 2008.

[103] A. Kusiek and J. Mazur, "Analysis of scattering from arbitrary configuration of cylindrical objects using hybrid finite-difference mode-matching method," in *Progress In Electromagnetics Research*, vol. 97, pp. 105-127, 2009.

[104] D. Arena, M. Ludovico, G. Manara and A. Monorchio, "Analysis of waveguide discontinuities using edge elements in a hybrid mode matching/finite elements approach," in *IEEE Microwave and Wireless Components Letters*, vol. 11, no. 9, pp. 379-381, Sept. 2001.

[105] A. Monorchio, P. Grassi and G. Manara, "A hybrid mode-matching finite-elements approach to the analysis of thick dichroic screens with arbitrarily shaped apertures," in *IEEE Antennas and Wireless Propagation Letters*, vol. 1, pp. 120-123, 2002.

[106] ANSYS, High Frequency Structural Simulator (HFSS), Finite Element Method (FEM). http://www.ansys.com/products/electronics/ansys-hfss.

[107] P. Barber and C. Yeh, "Scattering of electromagnetic waves by arbitrarily shaped dielectric bodies," in *Appl. Opt*., vol. 14, pp. 2864-2872, 1975.

[108] K. V. Beard and C. Chuang, "A new model for the equilibrium shape of raindrops," in *J. Atmos. Sci.*, vol. 44, pp. 1509-1524, 1987.

[109] K. V. Beard, V.N. Bringi and M. Thurai, "A new understanding of raindrop shape", in *Atmospheric Research*, vol. 97, pp. 396-415, 2010.

[110] E. A. Brandes, G. Zhang and J. Vivekanandan, "Drop Size Distribution Retrieval with Polarimetric Radar: Model and Application," in *J. Appl. Meteor*., vol. 43, pp. 461-475, 2004.

[111] V. N. Bringi and V. Chandrasekar, *Polarimetric Doppler Weather Radar: Principles and Applications*. Cambridge U. K.: Cambridge University Press, pp. 636, 2001.

[112] V. N. Bringi, M. Thurai, K. Nakagawa, G. J. Huang, T. Kobayashi, A. Adachi, H. Hanado and S. Sekizawa, "Rainfall estimation from C-band polarimetric radar in Okinawa, Japan: Comparisons with 2D-video disdrometer and 400 MHz wind profiler," in *J. Meteor. Soc. Japan*., vol. 84, pp. 705-724, 2006.

[113] L. D. Carey and W. A. Petersen, "Sensitivity of C-band polarimetric radar–based drop size estimates to maximum diameter," in *J. Appl. Meteor. Climatol.*, vol. 54, pp. 1352–1371, 2015.

[114] E. Chobanyan, N. J. Šekeljić, A. B. Manić, M. M. Ilić, V. N. Bringi and B. M. Notaroš "Efficient and Accurate Computational Electromagnetics Approach to Precipitation Particle Scattering Analysis Based on Higher-Order Method of Moments Integral Equation Modeling," in *J. Atmos. Oceanic Technol.*, vol. 32, pp. 1745–1758, 2015.

[115] G. J. Ciach and W. F. Krajewski, "On the estimation of radar rainfall error variance," in *Adv. Water Resour.*, vol. 22, pp. 585–595, 1999.

[116] C.C. Crowe, C.J. Schultz, M.R. Kumjian, L.D. Carey and W.A. Petersen, "Use of dual-polarization signatures in diagnosing tornadic potential," in *Electronic Journal of Operational Meteor.*, vol. 13, pp. 57-78, 2012.

[117] J. Hubbert and V. N. Bringi, "An iterative filtering technique for the analysis of copolar differential phase and dual-frequency radar measurements," in *J. Atmos. Oceanic Technol.*, vol. 12, pp. 643-648, 1995.

[118] G. Huang, V.N. Bringi and M. Thurai, "Orientation Angle Distributions of Drops after an 80-m Fall Using a 2D Video Disdrometer," in *J. Atmos. Oceanic Technol.*, vol. 25, pp. 1717-1723, 2008.

[119] A. R. Jameson, "Microphysical Interpretation of Multi-Parameter Radar Measurements in Rain. Part I: Interpretation of Polarization Measurements and Estimation of Raindrop Shapes," in *J. Atmos. Sci.*, vol. 40, pp. 1792-1802, 1983.

[120] A. R. Jameson, "Microphysical Interpretation of Multiparameter Radar Measurements in Rain. Part III: Interpretation and Measurement of Propagation Differential Phase Shift between Orthogonal Linear Polarizations," in *J. Atmos. Sci.*, vol. 42, pp. 607-614, 1985.

[121] A. R. Jameson, "Relations Among Linear and Circulur Polarization Parameters Measured in Canted Hydrometeors," in *J. Atmos. Oceanic Technol.*, vol. 4, pp. 634-646, 1987.

[122] W. J. Keat, C.D. Westbrook and A.J. Illingworth, "High-Precision Measurements of the Copolar Correlation Coefficient: Non-Gaussian Errors and Retrieval of the Dispersion Parameter μ in Rainfall," in *J. Appl. Meteor. Climatol.*, vol. 55, pp. 1615-1632, 2016.

[123] E. M. Klopf, N. J. Sekeljić, M. M. Ilić and B. M. Notaroš, "Optimal modeling parameters for higher order MoM-SIE and FEM-MoM electromagnetic simulations," in *IEEE Transactions on Antennas and Propagation*, vol. 60, pp. 2790-2801, 2012.

[124] G. W. Lee and I. Zawadzki, "Variability of drop size distributions: Noise and Noise filtering in Disdrometric data," in *J. Appl. Meteor.*, vol. 44, pp. 634-652. 2005.

[125] P. F. Meischner, V. N. Bringi, D. Heimann and H. Höller, "A Squall Line in Southern Germany: Kinematics and Precipitation Formation as Deduced by Advanced Polarimetric and Doppler Radar Measurements" in *Mon. Wea. Rev.*, vol. 119, pp. 678-701, 1991.

[126] M. I. Mishchenko, L. D. Travis and D. W. Mackowski, "T-matrix computations of light scattering by nonspherical particles: A review," J. Quant. Spectrosc. Radiat. Transfer, vol. 55, pp. 535-575, 1996.

[127] B. M. Notaroš, "Higher Order Frequency-Domain Computational Electromagnetics," in *IEEE Transactions on Antennas and Propagation*, vol. 56, 8, pp. 2251-2276, 2008.

[128] W. A. Petersen, K. R. Knupp, D. J. Cecil and J. R. Mecikalski, "The University of Alabama Huntsville THOR Center instrumentation: Research and operational collaboration," Preprints, *33rd Int. AMS Conf. on Radar Meteorology*, Cairns, Australia. [Available online at https://ams.confex.com/ams/33Radar/webprogram/Paper123410.html.] 2007.

[129] C. Sandford, A. Illingworth and R. Thompson, "The Potential Use of the Linear Depolarization Ratio to Distinguish between Convective and Stratiform Rainfall to Improve Radar Rain-Rate Estimates," in *J. Appl. Meteor. Climatol.*, vol. 56, pp. 2927–2940, 2017.

[130] M. Schönhuber, W. L. Randeu, H. E. Urban and J. P. V. Poiares Baptista, "Field measurements of raindrop orientation angles," *Proc. AP2000 Millennium Conf. on Antennas and Propagation*, Davos, Switzerland, IEE, CD-ROM, 2000.

[131] M. Schönhuber, G. Lammer and W. L. Randeu, "The 2D video disdrometer," *Precipitation: Advances in Measurement, Estimation and Prediction*. S. Michaelides, Ed., Springer, pp. 3-31, 2008.

[132] M. Schönhuber, M. Schwinzerl and G. Lammer, "3D Reconstruction of 2DVD-measured Raindrops for Precise Prediction of Propagation Parameters", *10th European Conference on Antennas and Propagation (EuCAP)*, Davos, 2016, pp. 1-4, doi: 10.1109/EuCAP.2016.7481929, 2016.

[133] T. J. Schuur, A. V. Ryzhkov, D. S. Zrnić and M. Schönhuber, "Drop size distributions measured by a 2-D video disdrometer: Comparison with Dual-polarization radar data," in *J. Appl. Meteor.*, vol. 40, pp. 1019-1034, 2001.

[134] M. Schwinzerl, M. Schönhuber, G. Lammer and M. Thurai, "3D reconstruction of individual raindrops from precise ground-based precipitation measurements", Extended Abstracts, *16th EMS Annual Meeting/11th European Conf. on Applied Climatology*, Trieste, Italy, European Meteorological Society, EMS2016-601. [Presentation available online at: http://presentations.copernicus.org/EMS2016-601_presentation.pptx.] 2016.

[135] T. A. Seliga and V. N. Bringi, "Potential use of radar differential reflectivity measurements at orthogonal polarizations for measuring precipitation," in *J. Appl. Meteor.*, vol. 15, pp. 69-76, 1976.

[136] T. A. Seliga and V. N. Bringi, "Differential reflectivity and differential phase shift: Applications in radar meteorology," in *Radio Science*, vol. 13, pp. 271-275, 1978.

[137] M. Szakáll, K. Diehl, S. K. Mitra and S. Borrmann "A Wind Tunnel Study on the Shape, Oscillation, and Internal Circulation of Large Raindrops with Sizes between 2.5 and 7.5 mm," in *J. Atmos. Sci.*, vol. 66, pp. 755-765, 2009.

[138] M. Thurai and V. N. Bringi, "Drop axis ratios from a 2D video disdrometer," in *J. Atmos. Oceanic Technol.*, vol. 22, pp. 966-978, 2005.

[139] M. Thurai, G. J. Huang, V. N. Bringi, W. L. Randeu and M. Schönhuber, "Drop shapes, model comparisons, and calculations of polarimetric radar parameters in rain," in *J. Atmos. Oceanic Technol.*, vol. 24, pp. 1019-1032, 2007.

[140] M. Thurai, V.N. Bringi, M. Szakáll, S.K. Mitra, K.V. Beard and S. Borrmann, "Drop Shapes and Axis Ratio Distributions: Comparison between 2D Video Disdrometer and Wind-Tunnel Measurements," in *J. Atmos. Oceanic Technol.*, vol. 26, pp. 1427-1432, 2009.

[141] M. Thurai, V. N. Bringi and W.A. Petersen "Rain microstructure retrievals using 2-D video disdrometer and C-band polarimetric radar," in *Adv. Geosci.*, vol. 20, pp. 13-18, 2009.

[142] M. Thurai, M., V. N. Bringi, L. D. Carey, P. Gatlin, E. Schultz and W. A. Petersen, "Estimating the accuracy of polarimetric radar–based retrievals of drop size distribution parameters and rain rate: An application of error variance separation using radar-derived spatial correlations," in *J. Hydrometeor*., vol. 13, pp. 1066-1079, 2012.

[143] M. Thurai, M., V. N. Bringi, W. A. Petersen and P. N. Gatlin, "Drop shapes and fall speeds in rain: two contrasting examples," in *J. Appl. Meteor. Climatol.*, vol. 52, pp. 2567-2581, 2013.

[144] M. Thurai, V. N. Bringi, A. B. Manić, N. J. Sekeljić and B. M. Notaroš, "Investigating rain drop shapes, oscillation modes, and implications for radiowave propagation," in *Radio Science*, vol. 49, pp. 921-932, 2014.

[145] M. Thurai, S. Manić, M. Schönhuber, V. N. Bringi and B. M. Notaroš, "Scattering calculations at C-band for asymmetric raindrops reconstructed from 2D video disdrometer measurements," in *J. Atmos. Oceanic Technol*., vol. 34, pp. 765-776, 2017 .

[146] P. C. Waterman, "Matrix formulation of electromagnetic scattering," in *Proc. IEEE*, vol. 53, pp. 805-812, 1965.

[147] A. C. Woo, H. T. G. Wang, M. J. Schuh and M. L. Sanders, "EM programmer's notebook-benchmark radar targets for the validation of computational electromagnetics programs," in *IEEE Antennas and Propagation Magazine*, vol. 35, no. 1, pp. 84-89, Feb 1993.

[148] G. S. Smith, "On the skin effect approximation," in *American Journal of Physics*, vol. 58, no. 10, pp. 996-1002, 1990.

[149] Woyna, Irene, "Wideband Impedance Boundary Conditions for FE/DG Methods for Solving Maxwell Equations in Time Domain." *Ph.D. Dissertation*, Technische Universität, Darmstad, Germany, 2014.

[150] J. M. Molina-Garcia-Pardo, M. Lienard, A. Nasr and P. Degauque, "On the Possibility of Interpreting Field Variations and Polarization in Arched Tunnels Using a Model for

Propagation in Rectangular or Circular Tunnels," in *IEEE Transactions on Antennas and Propagation*, vol. 56, no. 4, pp. 1206-1211, April 2008.

[151] D. G. Dudley, M. Lienard, S. F. Mahmoud and P. Degauque, "Wireless propagation in tunnels," in *IEEE Antennas and Propagation Magazine*, vol. 49, no. 2, pp. 11-26, April 2007.

[152] Tak Sum Chu and T. Itoh, "Generalized Scattering Matrix Method for Analysis of Cascaded and Offset Microstrip Step Discontinuities," in *IEEE Transactions on Microwave Theory and Techniques*, vol. 34, no. 2, pp. 280-284, Feb 1986.

[153] T. B. A. Senior, J. L. Volakis and S. R. Legault, "Higher order impedance and absorbing boundary conditions," in *IEEE Transactions on Antennas and Propagation*, vol. 45, no. 1, pp. 107-114, Jan. 1997.

[154] A. Emslie, R. Lagace and P. Strong, "Theory of the propagation of UHF radio waves in coal mine tunnels," in *IEEE Transactions on Antennas and Propagation*, vol. 23, no. 2, pp. 192-205, March 1975.

[155] Jacksha, R and C Zhou. "Measurement of RF propagation around corners in underground mines and tunnels." in *Transactions of Society for Mining, Metallurgy, and Exploration, Inc.*, vol. 340, no. 1, pp. 30-37, 2016.

[156] K. Guan et al., "Measurements and Analysis of Large-Scale Fading Characteristics in Curved Subway Tunnels at 920 MHz, 2400 MHz, and 5705 MHz," in *IEEE Transactions on Intelligent Transportation Systems*, vol. 16, no. 5, pp. 2393-2405, October 2015.

[157] S. F. Mahmoud, "Wireless transmission in tunnels with non-circular cross section," in *IEEE Transactions on Antennas and Propagation*, vol. 58, no. 2, pp. 613–616, February 2010.

[158] X. Zhang and C. D. Sarris, "Error analysis and comparative study of numerical methods for the parabolic equation applied to tunnel propagation modeling," in *IEEE Trans. Antennas Propag.*, vol. 63, no. 7, pp. 3025-3034, July 2015.

[159] X. Zhang and C. D. Sarris, "A Gaussian beam approximation approach for embedding antennas into vector parabolic equation based wireless channel propagation models," in *IEEE Transactions on Antennas and Propagation*, vol. 65, no. 2, pp. 1840–1849, February 2017.

[160] X. Zhang and C. D. Sarris, "Vector Parabolic Equation-Based Derivation of Rectangular Waveguide Surrogate Models of Arched Tunnels," in IEEE Transactions on Antennas and Propagation, vol. 66, no. 3, pp. 1392-1403, March 2018.

[161] M. F. Cátedra and J. Perez, *Cell Planning for Wireless Communications*. Norwood, MA, USA: Artech House, 1999.

[162] C. Garcia-Pardo, J.-M. Molina-García-Pardo, M. Lienard, D. P. Gaillot and P. Degauque, "Double Directional Channel Measurements in an Arched Tunnel and Interpretation Using Ray Tracing in a Rectangular Tunnel," in *Progress In Electromagnetics Research M*, vol. 22, pp. 91-107, 2012.

[163] D. Didascalou, T. M. Schafer, F. Weinmann and W. Wiesbeck, "Ray-density normalization for ray-optical wave propagation modeling in arbitrarily shaped tunnels," in *IEEE Transactions on Antennas and Propagation*, vol. 48, no. 9, pp. 1316-1325, September 2000.

[164] X. Zhang, N. Sood, J. Siu, and C. D. Sarris, "A hybrid ray-tracing/vector parabolic equation method for propagation modeling in train communication channels," in *IEEE Transactions on Antennas and Propagation*, vol. 64, no. 5, May 2016.

[165] W. Hou, X. Zhang, J. Wang and C. D. Sarris, "Hybrid Numerical Modeling of Electromagnetic Interference in Train Communication Systems," in *IEEE Transactions on Electromagnetic Compatibility*.

[166] N. Sood, S. Baroudi, X. Zhang, J. Liebeherr and C. D. Sarris, "Integrating Physics-Based Wireless Propagation Models and Network Protocol Design for Train Communication Systems," in *IEEE Transactions on Antennas and Propagation*, vol. 66, no. 12, pp. 6635-6645, December 2018.

[167] Moin, Nabeel, "Randomized Hierarchical Semi-Separable Structures for Parallel Direct Double-Higher-Order Method of Moments." *Master thesis*, Colorado State University, Department of Electrical and Computer Engineering, Fort Collins, Colorado, 2017.

[168] I.F. Akyildiz, Z. Sun and M.C. Vuran, " Signal propagation techniques for wireless underground communication networks", in *Physical Communication Journal (Elsevier)*, vol. 2, no.3, pp.167–183, 2009.